FORSCHUNGSZENTRUM KARLSRUHE
Technik und Umwelt

Wissenschaftliche Berichte
FZKA 6579

Temporal Structure of the Muon Component of Cosmic Rays Extensive Air Showers

Aurelian F. Badea[1]
Institut für Kernphysik

[1]On leave from National Institute of Physics and Nuclear Engineering – Horia Hulubei, Bucharest, Romania

Forschungszentrum Karlsruhe GmbH, Karlsruhe
2001

Abstract

The arrival time distribution of the muon component of an extensive air shower (EAS) has been investigated under the aspect of mapping via time-of-flight the EAS longitudinal development. For the experimental studies and the analyses based on Monte Carlo simulations the arrival time distributions have been characterised by the mean arrival time, the first quartile, the median and the third quartile of the single event distributions. Their correlations with other shower observables and their dependencies as functions of the distance from the shower axis, the zenith angle-of-incidence, the estimated primary energy and the muon multiplicity have been extensively studied.

The measurements use the timing, trigger facilities and Multiwire Proportional Chamber system of the Central Detector of the KASCADE experimental configuration, enabling arrival time measurements for muons with a 2.4 GeV energy threshold. In the present work the muon arrival time distributions have been experimentally studied relative to the first locally registered muon, in a radius interval of $20 \div 110$ m, for a zenith angle of the shower $0° \div 40°$ at primary energies around the "knee" region of the energy spectrum of primary cosmic rays.

The Monte Carlo simulations (using the program CORSIKA vers. 5.621) invoke as generators various hadronic interaction models, in particular QGSJET and GHEISHA for the high energy and low energy range of the EAS particles, respectively.

In order to reveal the relation between muon arrival time distributions and the longitudinal profile of the EAS development, a simulation study has been performed, scrutinising Linsley's approach to infer from arrival time measurements the electromagnetic and muonic elongation rate and fluctuations of the atmospheric height of the shower maximum. The determination of the elongation rate needs a scaling of the results with an a-priori unknown factor, which may be deduced from simulations.

Averaged time parameters of EAS muon component, in particular their lateral variation (time profiles) have been compared with predictions from simulations. In order to avoid effects arising from the strong fluctuations of the relative arrival time of the first locally arriving muon, a procedure has been developed to relate the arrival time distributions to the arrival of the EAS center (global arrival time distributions). They have been analysed on the basis of simple parameterisations and a good agreement is found. In ad-

dition the result have been used to deduce the average atmospheric heights of the production of the observed muons.
The role of the measured (local) muon arrival times distributions for a primary mass discrimination has been explored by means of a nonparametric multivariate analysis techniques on event-by-event basis. It is shown that muon arrival times distributions in the observed ranges of the limited distances from the shower center (between $50 \div 90$ m for muons with 2.4 GeV energy threshold) and the considered energy ranges, analysed in the correlation with other characteristic shower observables, do not significantly improve the mass discrimination, though pure CORSIKA simulations for an ideal detector exhibit promising features. This is mainly due to the relatively limited detector area of the Central Detector and relatively small distances from the shower core, while for larger radial distances with larger time of flights a time resolution of the order of 1 ns get less important. This feature advocates muon arrival time measurements with an extended detector array as useful source of information about the longitudinal EAS profile.

Die Zeitstruktur der Myonkomponente ausgedehnter Luftschauer

Ankunftszeitverteilungen in der Myonkomponente ausgedehnter Luftschauer (EAS) wurden unter dem Aspekt untersucht, inwieweit sie die longitudinale EAS-Entwicklung widerspiegeln. Die experimentellen Studien und Analysen, die auf Monte-Carlo Analysen der Schauerentwicklung basieren, charakterisieren die Ankunftszeitverteilungen durch den Mittelwert, den Median, das erste und dritte Quartil der Verteilung im einzelnen Schauerereignis. Die Korrelationen der Verteilungen dieser Größen mit anderen Schauer-Observablen und ihre Abhängigkeiten vom Abstand der Beobachtung von der Schauer-Achse, vom Schauer-Einfallswinkel, von der geschätzten Primärenergie und der Myon-Multiplizität der Verteilungen wurden ausführlich untersucht.
Die Messungen benutzen die Zeitdetektoren und Vieldraht-Proportionalkammern des KASCADE-Zentraldetektors, die Ankunftszeit-Messungen für Myonen mit einer 2,4-GeV Energieschwelle ermöglichen. In der vorliegenden Arbeit wurden die gemessenen Zeitverteilungen auf die Ankunftszeit des ersten lokal registrierten Myons bezogen und Abstände des Schauerzentrums von 20-110 m, ein Zenitwinkel-Bereich von 0-40 Grad bei Energien der Schauer induzierenden Teilchen im Bereich um das "Knie" des Primärspektrums der kosmischen Strahlung betrachtet. Die Monte-Carlo-Simulationen, die das Programm CORSIKA Version 5.621 benutzen, legen verschiedene hadronische Wechselwirkungs-Modelle als Generatoren zugrunde, insbesondere das QGSJET- beziehungsweise das GHEISHA-Modell für hoch-bzw. niederenergetische EAS-Teilchen.
Um den Zusammenhang zwischen Myon-Ankunftszeitverteilungen und longitudinalen EAS-Profil zu verdeutlichen, wird eine Simulations-Studie vorangestellt, welche eine von Linsley vorgeschlagene Methode überprüft, aus Ankunftszeit-Verteilungen die Elongationsrate und Fluktuationen der atmosphärischen Höhe des Schauermaximums zu gewinnen. Es stellt sich dabei heraus, dass in das Verfahren ein Skalenfaktor eingeht, dessen Wert a-priori unbekannt ist.
Die gemittelten Zeitparameter der EAS Myon-Komponente, insbesondere deren laterale Variation ("Zeit-Profile") werden mit Voraussagen von Monte-Carlo-Simulationen verglichen. Um Effekte zu vermeiden, die von den starken Fluktuationen der Ankunft des ersten registrierten Myons herrühren, wird ein Verfahren eingeführt, die "lokalen" Zeiten auf die Ankunftszeiten des

Schauer-Zentrums zu beziehen. Derartige "globale" Verteilungen werden in verschiedener Weise analysiert und zeigen gute Übereinstimmung mit Ergebnissen der Simulationen. Zusätzlich werden mit einfachen geometrischen Annahmen die Zeitverteilungen in Profile der Produktionshöhe transformiert. Um die Rolle der Myon-Ankunftszeitverteilungen für eine Bestimmung der Masse des primären EAS-Teilchens zu erforschen, werden mit Hilfe nichtparametrischer Klassifizierungsmethoden Multivariate-Verteilungen verschiedener Schauer-Observablen analysiert. Es stellt sich heraus, dass Ankunftszeitverteilungen von 2,4 GeV-Myonen, die innerhalb des eingeschränkten Abstandes von 50-90 m vom Schauerzentrum gemessen werden, unter Einbeziehung der endlichen Zeitauflösung kaum einen Beitrag zur Massen-Diskriminierung liefern. Das ändert sich jedoch bei größeren Abständen (sowie größeren Primärenergien), wo wegen der größeren Laufzeit-Effekte die experimentelle Zeitauflösung an Bedeutung verliert. Diese Beobachtung ermutigt, Myon-Ankunftszeit-Messungen mit einem über das gegenwärtige KASCADE-Areal hinaus ausgedehnten Detektor-Array durchzuführen.

CONTENTS

1. INTRODUCTION

Our earth is permanently bombarded by primary cosmic rays, most abundantly being high-energy protons and heavier nuclei. The cosmic ray energy density integrated over all energies is approximately 1 eV/cm^3, as compared with starlight having an energy density of 0.6 eV/cm^3 and with the energy density of the galactic magnetic field (0.2 eV/cm^3) [1].
The closest cosmic ray source to the Earth is the Sun. The "solar wind" modulation follows the periods of solar activity, containing very rarely, only during solar flares, particles with energies around 10^{10} eV. But cosmic rays contain also particles with energies many orders of magnitude above the most energetical particles from the Sun. The origin of such particles is most probably outside solar system, even outside Galaxy for the highest primary energies. The highest energy of a detected primary is $3 \cdot 10^{20}$ eV (detected in 1991 by Fly's Eye detector, Utah [2])!
The bulk of high-energy primary cosmic rays are accelerated at discrete sites in our Galaxy (magnetic clouds, supernova remnants) and roam around during $\sim$ 10 millions years before accidentally hitting the Earth. Their direction of incidence is no more related to the location of the sources, being deflected by the interstellar magnetic fields. The observable quantities which give informations about the origin, acceleration and propagation of the primary cosmic rays are their energy distribution and elemental composition [3]. The experimental determination of the primary energy distribution and mass composition is the main topic of contemporary cosmic ray research, especially in the energy range exceeding the energies provided by man-made particle accelerators up to now.
Comparing the relative abundance of solar and cosmic ray matter, some interesting features have been observed. Cosmic rays are overabundant in lithium, beryllium and boron. The iron concentration is quite identical, but in cosmic rays there is an excess of elements just lighter than iron. There is also an underabundance of hydrogen and helium. These differences can be understood by assuming that cosmic rays have the same composition as

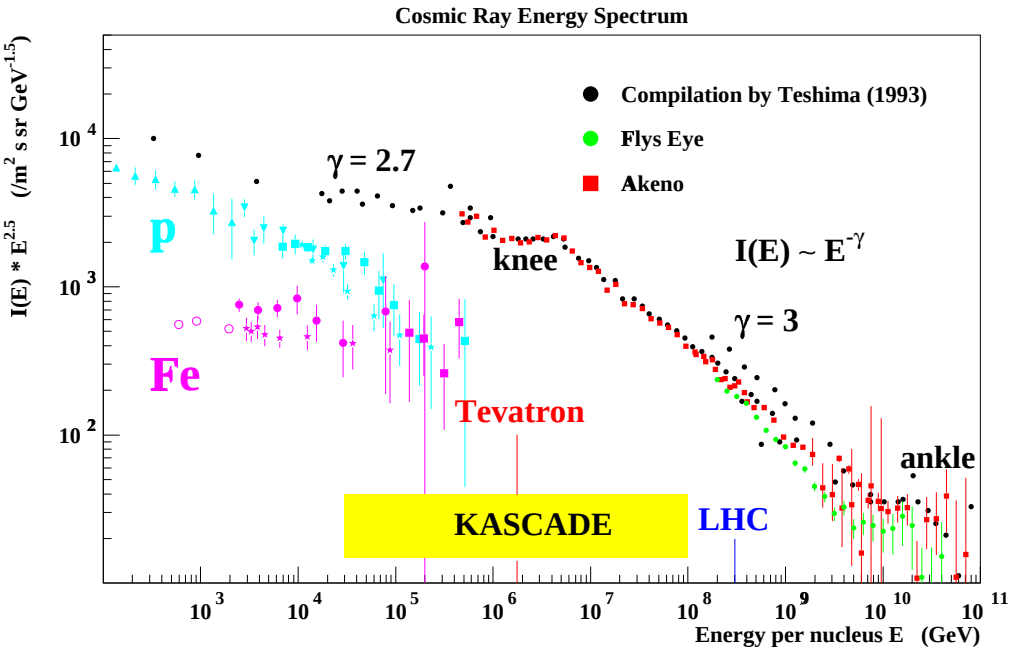

Fig. 1.1: Differential cosmic ray flux [5].

solar matter at their origin. Passing through interstellar space, they interact with gas and dust particles, lighter nuclei being obtained from spallation of heavier nuclei. The composition of cosmic rays at TeV to PeV energies is approximately 50% protons, 25% α-particles, 13% CNO and 13% Fe [4]. Primary electrons and photons contribute less than 1% to the total flux.
The differential energy spectrum (see Fig. 1.1) follows an overall power-law $\sim E^{-\gamma}$ with a characteristic distinct change around $4 \cdot 10^{15}$ eV, called the "knee". The spectral index γ changes from 2.7 before the knee to 3.1 beyond it. This conspicuous modulations of the energy spectrum around the knee can be interpreted as a primary composition change. The fact that a power law exists over many orders of magnitude is important in restricting possible acceleration and propagation mechanisms, since they have to reproduce the power law spectrum. The flux of the primary cosmic ray falls many orders of magnitude with increasing primary energy, e.g. from 1 particle/m^{2}s in 100 TeV range to 1 particle/km^{2}century in the EeV range. Because of the

strongly decreasing flux, experimental techniques used to detect cosmic rays are very different at different energies.
At lower energies ($< 10^{14}$ eV) where the cosmic ray flux is sufficiently large, direct measurements (using calorimeters, emulsions stacks, and spectrometers carried by balloons and satellites) have been performed. For measurements at higher energies, where the flux is strongly supressed primary cosmic rays can be studied indirectly by observations of extensive air showers (EAS) only, initiated in the Earth's atmosphere by the interaction of the primary particles from the cosmos. Such EAS are avalanches of particles which develop by the cascading interactions with air nuclei and move like widespread particle disks through the atmosphere to the observation level. The atmosphere acts as particle multiplier by which the primary high energy of the original particle gets distributed to millions of lower-energy EAS particles, which can be detected by large detector arrays. There are some recent detector arrays, used for studying EAS at energies corresponding to the "knee" region: KASCADE [6, 7, 8], CASA-MIA [9], HEGRA [10], EAS-TOP [11]. The EAS develops with three main components: the electromagnetic (e/γ), the muon and the hadron components, which are additionally accompanied by Cherenkov radiation and nitrogen fluorescence produced in the air. The experiment KASCADE [1] enables a simultaneous (event-by-event) observation of the three charged particle components with a larger number of parameters characterising the EAS. The general procedure to assign an observed EAS to a certain primary energy (E_0) and to a certain primary type (A) is to etablish an energy estimator (a shower observable or a combination of shower observables almost independent on primary mass) and shower observables which can be used for primary mass discrimination. The analysis of such observables can be only done by realistic simulations of the EAS development with adopting particular hadronic interaction models at particle energies exceeding our experimental knowledge from studies at man-made accelerators. On the other side, EAS observations in the PeV region and above, performed with a multi-detector experiment observing simultaneously all major EAS components with many observables, provide the possibility to test the hadronic interaction models and to specify the most consistent one [12, 13, 14].

The temporal structure of the EAS muon component is of special interest

[1] The author is member of the KASCADE collaboration [6].

since it is expected to map the longitudinal development of the shower through the time-of-flight of the relativistic muons from the production locus to the observation level. This is due to the fact that (higher energy) muons do only weakly interact and are practically not absorbed in the atmosphere. Thus the observation and an adequate analysis of EAS muon arrival time distributions provide information about the longitudinal development and help to constrain the mass identification of the primary. This is in particular important when alternative sources of information about the longitudinal EAS profile like air-Cherenkov or air fluorescence measurements are not accessible. The present thesis reports on a detailed investigation of the temporal structure of the muon component under these aspects. The experimental investigation is preceded by an EAS simulation study, revealing the relation between longitudinal EAS development and muon arrival time distribution. In particular the applicability of an approach for the determination of the elongation rate, introduced by Linsley [15] will be scrutinised. The experimental muon arrival distributions, measured with the timing facilities of the KASCADE Central Detector, are analysed in view of their agreement with the predictions of the QGSJET hadronic interaction model. In contrast to previous work, which did exclusively consider the local time structure of the EAS, in the present work the observation are evaluated by global times, i.e. relating the arrival times to a reference time common for all observation distances from the EAS centre. For that an efficient procedure transforming "local" times in "global" times is proposed and applied. Finally, by use of advanced statistical decision methods, the role of muon arrival time distribution data for the mass discrimination of the EAS primaries in event-by-event analyses is explored.

2. EXTENSIVE AIR SHOWERS AND TIME STRUCTURE VARIABLES

2.1 Extensive air showers

The development of an extensive air shower (see Fig. 2.1) is a very complex process. The high energy of the primary particle (proton, helium and also heavier nuclei) is distributed to millions of secondary particles, propagated as a wide disk through the atmosphere, approximately with the speed of light. There are three main components of charged particles in EAS: electrons/positrons, muons and hadrons (near shower axis). As example, an EAS initiated by an 1 Pev proton contains approximately half a million products at sea level, of which about 80% are γ-rays, about 15% electrons and positrons, about 2% muons, and about 0.2% hadrons. Most secondary particles produced by primary strong interactions are π mesons. The neutral π mesons decay almost immediately into two γ-rays:

$$\pi^0 \rightarrow \gamma + \gamma \tag{2.1}$$

These γ-rays start electromagnetic avalanches by pair production (e^+e^-) and bremsstrahlung processes. When the electrons and positrons reach an energy level of about 100 MeV, energy loss by ionisation starts to become important and the particles are quickly stopped; after reaching a maximum, their number declines approximately in an exponential way. The charged π mesons either interact with atoms of the atmosphere, producing further particles or decay into muons. The muon component originates from the decay of charged pions and kaons [16]:

$$\begin{array}{l} \pi^{\pm} \rightarrow \mu^{\pm} + \nu_{\mu}(\overline{\nu}_{\mu}) \\ K^{\pm} \rightarrow \mu^{\pm} + \nu_{\mu}(\overline{\nu}_{\mu}) \end{array} \tag{2.2}$$

Muons form the penetrating EAS component, since they get less absorbed

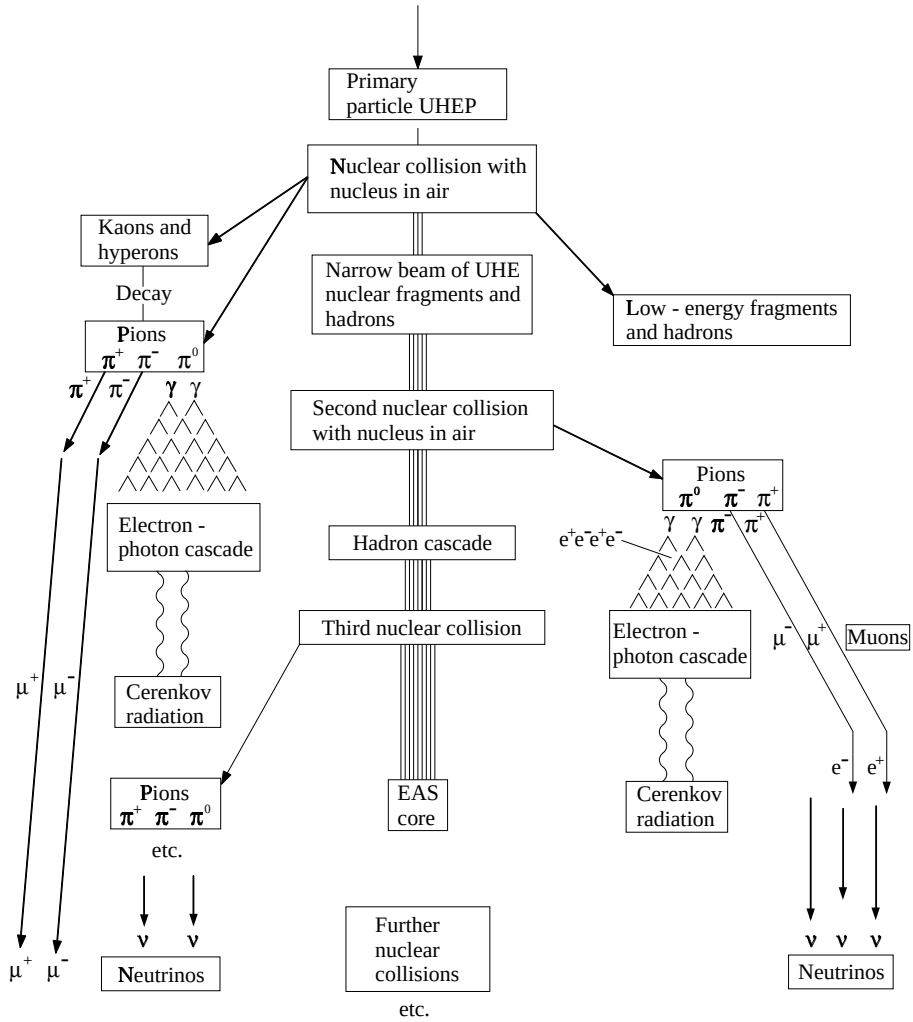

Fig. 2.1: EAS development.

and reach the ground with a large probability, even when produced at high altitudes, due to their comparatively long lifetime, which is enlarged by relativistic time dilatation. When high-energy muons decay in flight, the decay electrons are able to initiate additional electromagnetic cascades which contribute to the electron-photon avalanche. The backbone of an air shower is the hadronic component containing mostly pions but also nucleons, antinucleons, K mesons and more exotic particles. The three main EAS com-

ponents are accompanied by Cherenkov and fluorescence light in the atmosphere produced by ionizing particles from EAS. The opening angle for Cherenkov light emission in the atmosphere is approximately two degrees, so the Cherenkov light is highly collimated with respect to the original particle direction. Because of this, the Cherenkov technique is useful for lower energy events (the primary flux being high enough) and particularly in searching for point sources. The fluorescence light allows a large collection area because it is produced isotropically, being used to study cosmic rays of highest energy. In EAS studies the detector arrays access usually the intensity, the lateral, the arrival time and (occasionally) the energy distributions of different shower components. Observations are made of:

- the intensity, lateral and arrival time distributions of the (soft) electromagnetic (e/γ) component;
- the energy spectrum, radial distributions and relative arrival times of the hadrons in the shower core;
- the intensity, lateral and relative arrival time distributions of the (penetrating) muon component;
- the intensity, lateral and longitudinal distributions of the Cherenkov-light in the atmosphere;
- the intensity and longitudinal distribution of the fluorescence light in the atmosphere.

From such measurements a number of observables are derived. The basic information is derived by the reconstruction of the zenital and azimuthal angle of the shower incidence, the position of the shower centre (shower axis), the total intensity of charged particles or the electron component, i.e. the shower size N_e, the muon content N_μ, the parameters describing the lateral distributions and other observables as accessible by the particular detector set-up. Of particular interest are observables which carry information about the longitudinal EAS development. Simple kinematics arguments let expect that the distribution of the arrival times of the EAS muons maps via the time-of-flight the distribution of the production heights of the muons arriving at the observation level [17, 18]. In fact, alternatively to Cherenkov and fluorescence light observables - when the corresponding devices to measure them are missing - the direct access to the longitudinal development of the

shower is provided by the muon arrival times and by the strongly correlated [19] muon angles-of-incidence distributions.

2.2 Global and local muon arrival times

The definition of observables representing the temporal structure of the EAS, observed at a certain observation level, need a reference zero-time. There are two possibilities to choose the zero-time for muon arrival times in a certain shower (Fig. 2.2).
One possibility is to define as reference the arrival time τ_{cor} of the electromagnetic front of the shower centre. Time quantities referring to τ_{cor} are

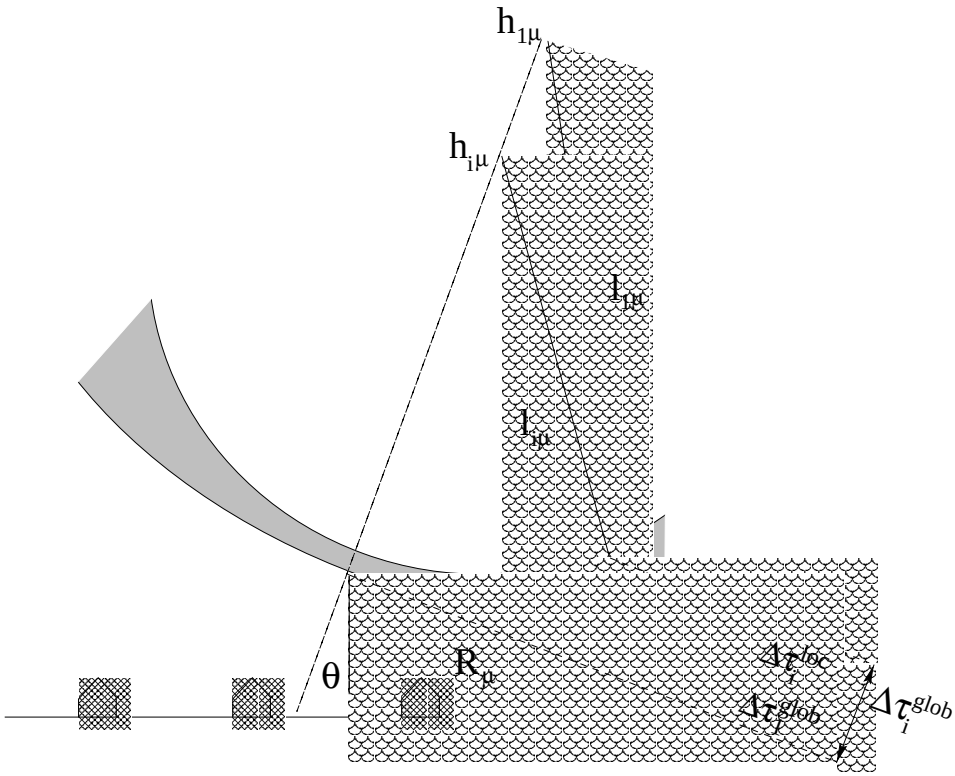

Fig. 2.2: Characterisation of the EAS temporal structure by global and local arrival times.

called "global" times:

$$\begin{aligned} \Delta\tau_1^{glob}(R_\mu) &= \tau_{1\mu}(R_\mu) - \tau_{cor} \\ \Delta\tau_i^{glob}(R_\mu) &= \tau_{i\mu}(R_\mu) - \tau_{cor} \end{aligned} \tag{2.3}$$

where $\tau_{1\mu}$ is the arrival time of the foremost muon. In general, the distance R_μ to the shower core is defined in a plane perpendicular to the shower axis, which is specified by zenith angle θ and the azimuth angle ϕ of the direction of incidence. The arrival time of the electromagnetic front of the shower core has been used as reference in many studies [17, 18], also in the first analysis of relative muon arrival times with KASCADE data [20].
The second possibility is to consider as reference the arrival time of the foremost muon, registered in the timing detector at the particular distance from the shower centre R_μ. In this case, muon arrival times will be called "local times":

$$\begin{aligned} \Delta\tau_1^{loc}(R_\mu) &= 0 \\ \Delta\tau_i^{loc}(R_\mu) &= \tau_{i\mu}(R_\mu) - \tau_{1\mu}(R_\mu) \end{aligned} \tag{2.4}$$

Experimentally it turned out [20] that τ_{cor} is not well determined from the arrival times of the electromagnetic component near the shower core with the present reconstruction procedures, and it introduces an additional jitter of some nanoseconds. Hence, in some recent studies [21, 22], local times have been prefered. Global times can be related in a very intuitive way with the longitudinal development of the shower. Considering high energy muons ($v_\mu \simeq c$) produced near the shower axis, neglecting their Coulomb scattering through the atmosphere, a simple triangulation gives the relation between global time and height of production for a certain muon [17] (see Fig. 2.2):

$$\Delta\tau_i^{glob} = \frac{l_{i\mu} - h_{i\mu}}{c} = \frac{\sqrt{R_\mu^2 + h_{i\mu}^2} - h_{i\mu}}{c} \simeq \frac{R_\mu^2}{2h_{i\mu}c}\,,\ R_\mu \ll h_{i\mu} \tag{2.5}$$

In the present work both global and local times will be considered. Global times are derived from the measured local times using the procedure presented in Sec. 5.4. For a detailed characterisation of the time structure, the *mean value* ($\Delta\tau_{mean}$) and also specific quantiles ($\Delta\tau_\alpha$) of the arrival time distributions will be used: the *first quartile* ($\Delta\tau_{0.25}$), the *median value* ($\Delta\tau_{0.50}$) and the *third quartile* ($\Delta\tau_{0.75}$), which exhibit different features of the time structure of the muon component. For ordered statistics of measured times

$\Delta\tau_1 \leq \Delta\tau_2 \leq ... \leq \Delta\tau_n$ and $i := n \cdot \alpha + \xi$, i integer and $\xi \in [0,1)$, the α-quantile $\Delta\tau_\alpha$ ($\alpha \in (0,1)$) is the following [23]:

$$\Delta\tau_\alpha = \begin{cases} (\Delta\tau_i + \Delta\tau_{i+1})/2 & : \quad \text{for } \xi = 0 \\ \Delta\tau_i & : \quad \text{for } \xi \in (0,1) \end{cases} \tag{2.6}$$

That means: in the case of large n, a fraction α of muons have arrival times less than $\Delta\tau_\alpha$.
The quantities, defined in this section for characterising the temporal EAS structure, can be evaluated for each single shower event and the measurements result in distributions of these quantities within the considered event sample. Altenatively, renouncing of an event-by-event analysis and specifying the samples by certain bins of other characteristic observables (angle-of-incidence θ, distance to the shower core R_μ,...) the single arrival time distributions could be added up and afterwards characterised by the different quantiles.

3. LONGITUDINAL EAS DEVELOPMENT AND MUON ARRIVAL TIME DISTRIBUTIONS.

In advance of the presentation of the experimental aspects and results of the present work and in order to elucidate the relation of EAS muon arrival time distributions with features of the longitudinal development, an extensive study [24] based on Monte Carlo simulations of the EAS development is briefly sketched. It is particularly focussed to scrutinise the information mapped by EAS time structure about the atmospheric height X_m of the shower maximum and the energy dependence of X_m, expressed by the so-called elongation rate.

3.1 The Monte Carlo EAS simulation code CORSIKA

The complex processes generating an Extensive Air Shower can be modeled only by Monte Carlo simulations in which each particle in the shower is followed from production to destruction, decay or passage through the plane of observation. Because of statistical fluctuations the calculations have to be repeated many times for the same starting conditions such as primary mass, energy and direction. A prerequisite is a knowledge of particle production in high energy interactions. Realising that we deal with primary energies of orders of magnitude higher than presently reached by man-made accelerators, the knowledge gained in collider experiments (at CERN and Fermilab) has to be extrapolated, guided by realistic theoretical concepts. The most important features of the high energy nucleon-nucleon interactions determined in collider experiments are:

- the *multiplicity* (number of produced secondary particles) in a high energy nucleon-nucleon interaction increases with primary energy but

less than in a linear proportion;

- the *inelasticity* (the average fraction of energy converted into new particles) is about 50% and almost independent of energy;

- as a consequence of these facts, the average energy of secondary particles increases faster than the primary energy;

- the *mean transverse momentum* imparted to secondary particles increases only slowly with energy. Since the longitudinal momentum grows faster the angles between the momenta of the primary particle and secondaries decrease.

These features of the high energy nucleon-nucleon interaction has to be extended to high energy nucleus-nucleus interaction. It is important to realise that the binding energy of a primary iron nucleus (about 500 MeV) is only a small fraction of the energy available in the centre of mass system. As a first approximation, it is reasonable to consider that an iron nucleus is a superposition of 56 nucleons each with one fifty-sixth of the energy of the nucleus. Assuming this, some differences in the observables can be predicted between extensive air showers initiated by a proton and iron nucleus of the same total energy:

- the 56 nucleons of iron produce more secondary particles than a single proton because of the slower increase of the multiplicity with energy. Most secondaries are π mesons decaying into muons. Because of this, an EAS induced by iron contains more muons than a proton induced shower.

- for similar reasons, hadrons in a proton shower have higher energy than hadrons in an iron shower;

- the smaller deflection angles of secondary particles in proton shower correspond to steeper lateral distributions of particles in the plane of observation;

- the number of electrons is larger in a proton shower because they reflect the energies of the neutral π mesons from which they originate. The maximum of the shower development is reached higher in the atmosphere for an iron shower.

CORSIKA [25] (**CO**smic **R**ay **SI**mulations for **KA**SCADE) is a program for detailed Monte Carlo simulations of the atmospheric development of EAS initiated by high energy cosmic ray particles. Protons, light nuclei up to iron, photons and other particles can be treated as primaries. The adopted atmosphere consists of N_2, O_2 and Ar with the volume fractions of 78.1%, 21% and 0.9% [26]. The U.S. standard atmosphere with five layers:

$$\rho(h) = a_i + b_i exp(-h/c_i)$$

is used as atmospheric density profile (for the parameters see ref. [25]).
CORSIKA uses several models currently en vogue as generators of the hadronic interactions driving the EAS cascade. For higher energies these are alternatively:

- VENUS [27] (**V**ery **E**nergetic **NU**clear **S**cattering)
- QGSJET [28] (**Q**uark **G**luon **S**tring model with **JET**s)
- DPMJET [29] (**D**ual **P**arton **M**odel with **JET**s)
- SIBYLL [30]
- HDPM [25] (**H**adron **D**ual **P**arton **M**odel)

VENUS, QGSJET and DPMJET models are based on the Gribov-Regge theory; SIBYLL is a minijet model; HDPM is a phenomenological generator and adjusted to experimental data wherever possible. These high energy models reach their limit if the energy available for generation of secondary particles drops below a certain value and are replaced by GHEISHA [31] ($E_{cm} \leq 12$ GeV i.e. $E_{lab} \leq 80$ GeV) or ISOBAR [32] ($E_{cm} \leq 10$ GeV i.e. $E_{lab} \leq 50$ GeV) models. E_{cm} and E_{lab} represent available energies for generation of secondary particles in center of mass and respectively laboratory reference systems. The GHEISHA routines as implemented in CORSIKA are taken from the detector simulation code GEANT3 [33]. Approximating hadron-nucleus collisions by hadron-nucleon reactions, ISOBAR model enables fast calculations.
For the simulation of the electron-photon component, the program offers two possibilities: the EGS4 (**E**lectron **G**amma **S**hower system version 4) Monte Carlo procedure [34] or alternatively the NKG (**N**ishimura **K**amata **G**reisen) [35] approximation. The EGS4 enables a full Monte Carlo simulation of

the electromagnetic component delivering detailed information (momentum, space coordinates, propagation time) of all electromagnetic particles. The considerable computional time consumption of the EGS option can be reduced by the use of the NKG approximation. This approximation is an analytical description of pure electromagnetically induced showers providing parametrisations of the longitudinal profile and of the lateral distribution of the electron photon component (see e.g. [36]). They contain as parameter the so-called "age", which controls the status of development of the electron-photon cascade: $s = 0$ at the begining, $s = 1$ at the depth of the EAS electromagnetic maximum. Empirically it turns out that the application of the NKG parametrisations to the superposition of many electromagnetic subshowers, generated in a hadron induced EAS, is a very good first approximation. The same parameter s enters in the description of the lateral distribution of the electron density [35].
The influence of the Earth's magnetic field on the propagation of charged particles is taken into account.

3.2 The longitudinal development of the electromagnetic and muonic component

In order to prepare the basis of simulation data for featuring the longitudinal profile and its relation with muon arrival time distributions, CORSIKA [25] of the vers.5.621 has been used for the data preparation. QGSJET and GHEISHA codes have been considered for high energy interactions and low energy interactions, respectively. NKG approximation has been used for the simulation of the electromagnetic component. Monte Carlo calculations have been performed for proton and iron primaries inducing extensive air showers at three different primary energies ($E_0 = 10^{15}$ eV, $3.16 \cdot 10^{15}$ eV, 10^{16} eV) and three different angles-of-incidence ($\theta = 15°, 25°, 35°$) with a set of 1000 simulated EAS for each case.
The EAS quantities of interest are evaluated at six different observation levels: 250 g/cm^2 (10.5 km a.s.l.), 400 g/cm^2 (7.4 km a.s.l.), 550 g/cm^2 (5.0 km a.s.l.)- corresponding to Chacaltaya experiment [37], 700 g/cm^2 (3.2 km a.s.l.) - ANI experiment [38], 850 g/cm^2 (1.6 km a.s.l.) - Mt. Abu experiment [39], 1020 g/cm^2 (110 m a.s.l.) - KASCADE experiment. The basic parameters of the primary particle-air interaction (mean free path, inelasticity, multiplicity of secondary-particle production) influence critically the early development

of EAS. A shorter initial free path, higher inelasticity and multiplicity are associated to a primary particle with higher atomic number. Even if the early EAS stage is difficult to be observed directly, it influences the position of the atmospheric depth of the maximum EAS development.
The longitudinal developments of the electromagnetic and muonic components are scrutinised on the base of the simulations presented above with a focus to the procedure for estimating the depths of their maxima. Differences between longitudinal developments of proton and iron induced air showers are revealed and also the differences between electromagnetic and muonic longitudinal developments at the same shower.
The number of muons (N_μ) and electrons (N_e) are counted for each shower at the six observation levels defined above. Two different energy thresholds (0.25 GeV and 2.0 GeV) have been considered for muons. The longitudinal variation and the fluctuations of the shower size N_e and of the number of muons N_μ are displayed in Fig. 3.1 for proton and iron induced EAS with the zenith-angle $\theta = 15^\circ$ and the primary energy $E_0 = 10^{15}$ eV. Such a figure represents just an access for six observation levels to the longitudinal development of the shower. The electromagnetic component exhibits a relatively well pronounced maximum of the shower size N_e. The penetrating muon component (N_μ) appears to be shifted slightly deeper and rather shallow, since the muon number losses, after reaching a kind of plateau of N_μ, are relatively small, especially for higher energy muons.
The depths of the electromagnetic and muonic maxima (X^μ and X^e, respectively) are furtheron estimated for each individual shower. The number of muons N_μ^i at the defined six levels X_i ($i \in \{1, 6\}$) are used to estimate the depth of the muon maximum. If X_j is the observation level (from six levels) with the highest number of muons N_μ^j, than a parabola is defined by the point $(X_j, log_{10}N_\mu^j)$ and its neighbouring points $((X_{j-1}, log_{10}N_\mu^{j-1})$ and $(X_{j+1}, log_{10}N_\mu^{j+1}))$:

$$log_{10}N_\mu(X) = a_1X^2 + b_1X + c_1$$

The coefficients a_1, b_1, c_1 being calculated, the depth of the muon maximum is:

$$X_m^\mu = -b_1/2a_1$$

i.e. it corresponds to the maximum of the parabola.
This procedure have not been repeated for estimating the electromagnetic maximum. A more precise estimation have been prefered based on the fact

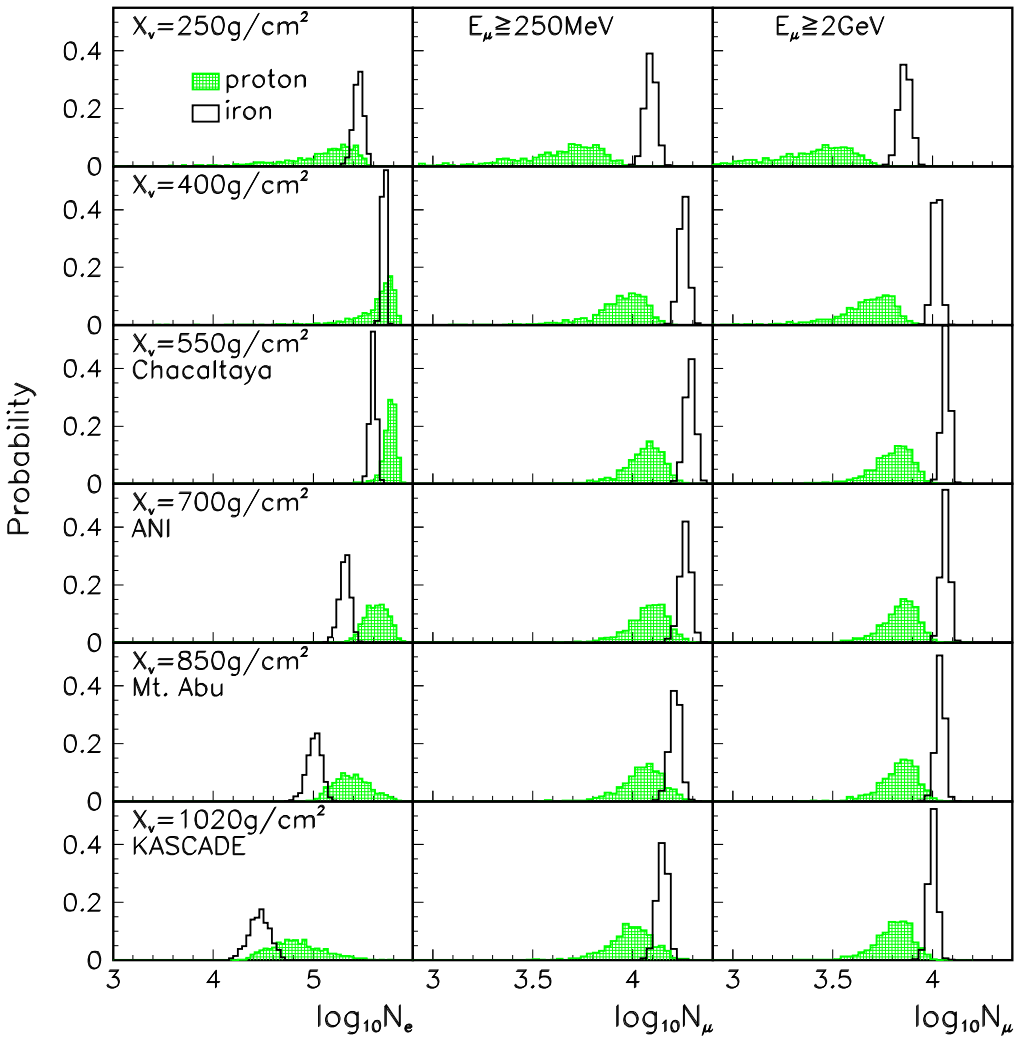

Fig. 3.1: The depth dependence of the shower sizes N_e and of the muon numbers N_μ (considering two muon energy thresholds) for proton and iron - induced EAS ($E_0 = 10^{15}$ eV, $\theta = 15°$).

that the CORSIKA program (with the NKG option) provides (analytically) the shower age parameter s_l for more atmospheric depths X_l ($l \in \{1, 10\}$): 100 g/cm^2, 200 g/cm^2,..., 1000 g/cm^2. A shower age $s = 1$ [35] have been assumed at the electromagnetic maximum of the shower. If (X_{k-1}, s_{k-1}) and

(X_k, s_k) are the neighbouring points with shower ages $s_{k-1} < 1$ and $s_k > 1$, defining the linear dependence:

$$s(X) = a_2 X + b_2$$

the depth of the electromagnetic maximum is:

$$X_m^e = (1 - b_2)/a_2$$

The relations above, estimating X_m^e and X_m^μ, have been written for vertical showers. They are valuable also for inclined showers just multiplying all atmospheric depths by $sec\theta$. There is a clear difference between electromagnetic maximum X_m^e and muon maximum X_m^μ. Their mean values over many showers ($\langle X_m^e \rangle$ and $\langle X_m^\mu \rangle$) have been used in the next section for estimating the electromagnetic and muonic elongation rates.

3.3 Elongation rate

The average depth X_m^e of the electromagnetic maximum of the EAS development depends on the energy E_0 and the mass A of the primary particle. Its dependence from the energy (aproximately in a logarithmic way) is expressed by the so-called *elongation rate* D_e^e, defined as change of the average depth of the maximum with lnE_0 [15, 42]:

$$D_e^e = dX_m^e/dlnE_0 \tag{3.1}$$

Taking into account the (smooth) energy dependence of the multiplicity production and of the hadronic cross sections by modifying the radiation length X_0 in air by the fraction B, the elongation rate is usually written as:

$$D_e^e = (1 - B)X_0 \tag{3.2}$$

B can be expressed by a series of simple terms which express the energy dependence of the multiplicity, g, of particles produced in interactions [15] and the energy dependence of hadronic cross sections [43]:

$$B = B_g + B_\lambda, \text{ where } B_g = d(lng)/d(lnE_0) \text{ and } B_\lambda = \beta d(\lambda_N + \lambda_\pi)/d(lnE_0).$$

where βX_0 is a dimensionless constant of order unity and λ_N, λ_π are the mean free paths in air of nucleons and pions respectively. Invoking the superposition model approximation, i.e. assuming that a heavy primary (A)

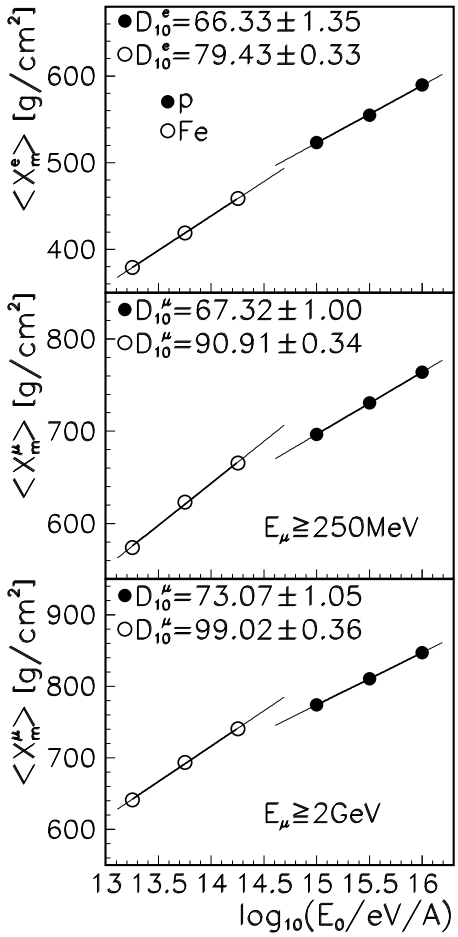

Fig. 3.2: The energy variation of mean depths $\langle X_m^e \rangle$ and $\langle X_m^\mu \rangle$ of the shower maximum of the electromagnetic and muon components (for two different muon detection thresholds), respectively. The elongation rate values are the slopes of the linear fits.

has the same shower elongation rate like a proton, but scaled with energies E_0/A we obtain:

$$X_m^e = X_{init} + D_e^e ln(E_0/A) \tag{3.3}$$

where X_{init} is the starting point of the shower. For a mixed composition, characterized by $\langle lnA \rangle$, Eq.3.3 becomes:

$$\langle X_m^e \rangle = X_{init} + D_e^e(lnE_0 - \langle lnA \rangle) \tag{3.4}$$

As long as D_e^e is only weekly dependent on the energy, X_m^e shows practically a linear dependence from lnE_0 and any change in this dependence is indicative for a change either of D_e^e or of the composition ($\langle lnA \rangle$). Therefore D_e^e is an interesting quantity of the EAS development. For discussions in context of observations communicated in literature we consider furtheron the quantity $D_{10}^e = dX_m^e/dlog_{10}E_0 \simeq 2.3D_e^e$. Generalising the concept the muonic elongation rate D_{10}^μ is defined:

$$D_{10}^\mu = dX_m^\mu/dlog_{10}E_0 \tag{3.5}$$

with X_m^μ being the depth of the maximum of the EAS muon component.
In literature there are only references for the "electromagnetic" elongation rate. Monte Carlo simulation studies of the EAS longitudinal development suggest a value of $D_{10}^e = (80 \pm 11)$ g·cm^{-2}/decade [44]. Experimental investigations, though with a large spread, tend to smaller values [44, 45]. The HEGRA collaboration has communicated as preliminary result $D_{10}^e = (52 \pm 2 \pm 10)$ g·cm^{-2}/decade [40].
Fig. 3.2 shows the energy dependence of the mean electromagnetic maximum depth $\langle X_m^e \rangle$ and mean muon maximum depths $\langle X_m^\mu \rangle$ (for two different muon energy thresholds) obtained by the present simulation procedure. The dependence on $log_{10}E_0$ proves to be linear and the mean values of the electromagnetic elongation rate (quoted with the errors) are in the range of expected values.
All three zenith angles from simulations (15°, 25°, 35°) have been considered together. There is a tendency of $\langle X_m \rangle$ and D_{10} with the zenith angle which can be also understood as effect of the different path lengths of the particle traversing the same mass layers with different zenith angles and different decay chances; but because of systematic uncertainities affecting the estimation of X_m for each individual shower a mean value $\langle X_m \rangle$ over all three zenith angles is regarded to be representative. The fluctuations $\delta(X_m)$ (standard deviation of the X_m distributions) prove to be just slightly decreasing with energy, but they are different for different cases: $\delta(X_m^e)(p) \approx 80$ g/cm^2, $\delta(X_m^e)(Fe) \approx 17$ g/cm^2, $\delta(X_m^\mu)(p) \approx 100$ g/cm^2, $\delta(X_m^\mu)(Fe) \approx 30$ g/cm^2.

3.4 Muon arrival time distributions and the atmospheric height X_m

Time parameters are calculated by counting all muon arrival times at a distance R_μ = between $90 \div 110$ m from the shower axis. Fig. 3.3 displays the correlations of global mean value ($\Delta\tau^{glob}_{mean}$), first quartil ($\Delta\tau^{glob}_{0.25}$) and third quartil ($\Delta\tau^{glob}_{0.75}$) at the observation level of the KASCADE experiment with the electromagnetic and muonic shower depths (inferred from the simulation results) and reveals the considerable fluctuations, in particular for

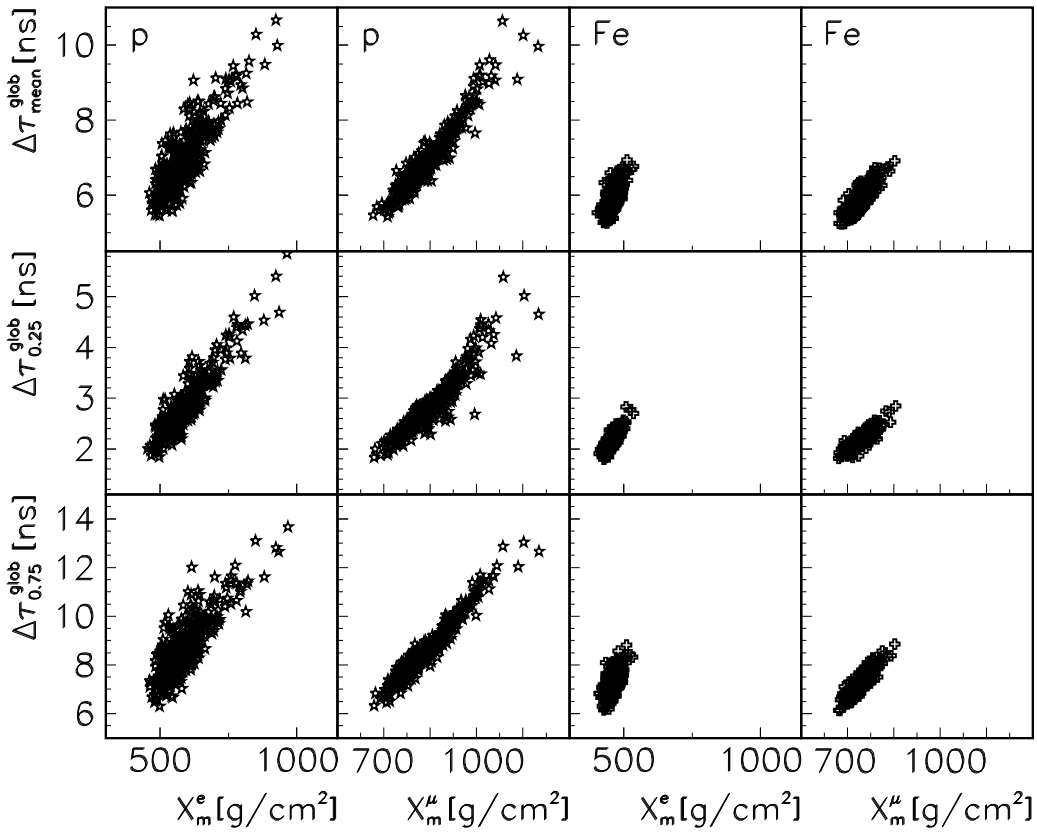

Fig. 3.3: Correlations between different muon arrival time parameters observed at KASCADE level and the electromagnetic (X^e_m) or muonic (X^μ_m) maximum depths. Markers represent individual showers initiated by proton and iron with $E_0 = 10^{16}$ eV and $\theta = 15°$; $E_\mu \geq 2$ GeV; 90 m $< R_\mu \leq$ 110 m.

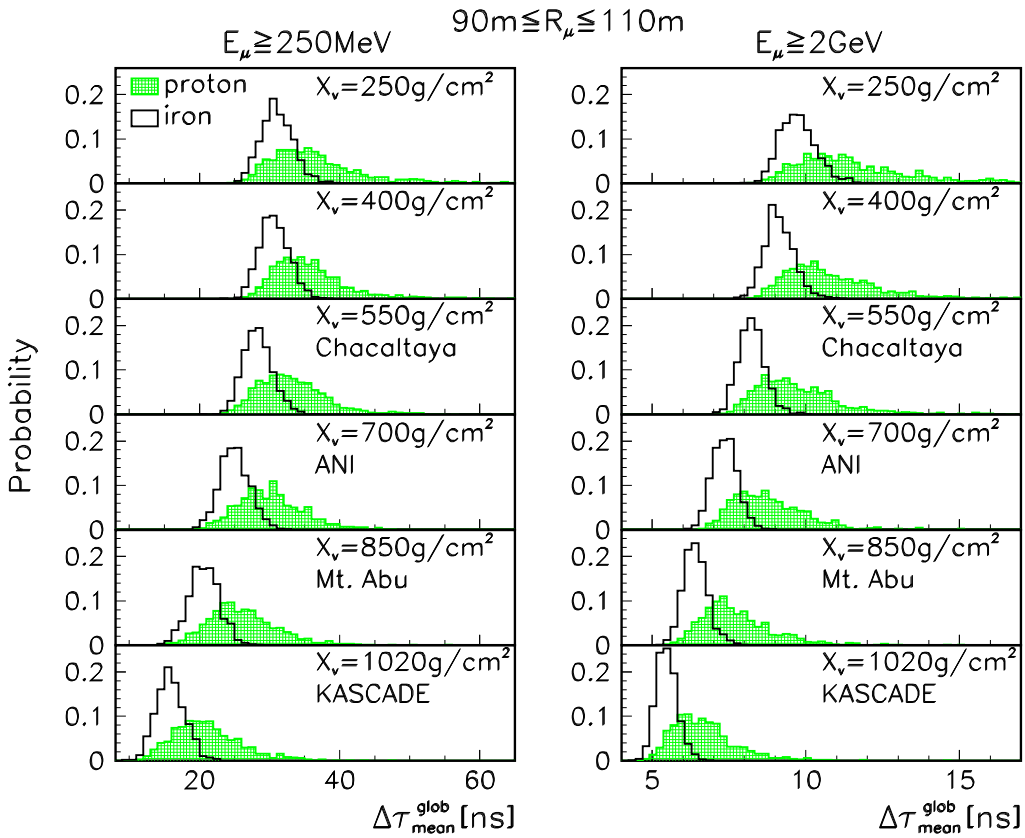

Fig. 3.4: Mean value distributions of muon arrival times calculated for different muon energy thresholds at various observation levels for proton and iron induced EAS of $E_0 = 3.16{\cdot}10^{15}$ eV ($\theta = 15°$); global times.

primary protons. The gross features of the variation of the global distributions of the mean arrival times with the observation level are indicated in Fig. 3.4. According to relation 2.5, muons coming from higher altitude have smaller global arrival times. Muons in a heavy-primary induced shower are produced at higher altitudes in the atmosphere. An iron primary has a much smaller interaction length $\lambda_{Fe} \simeq 15$ g/cm^2 as compared to the proton interaction length $\lambda_H \simeq 80$ g/cm^2. Because of this reason, at a given distance from the shower core, in average, muon arrival times from an iron

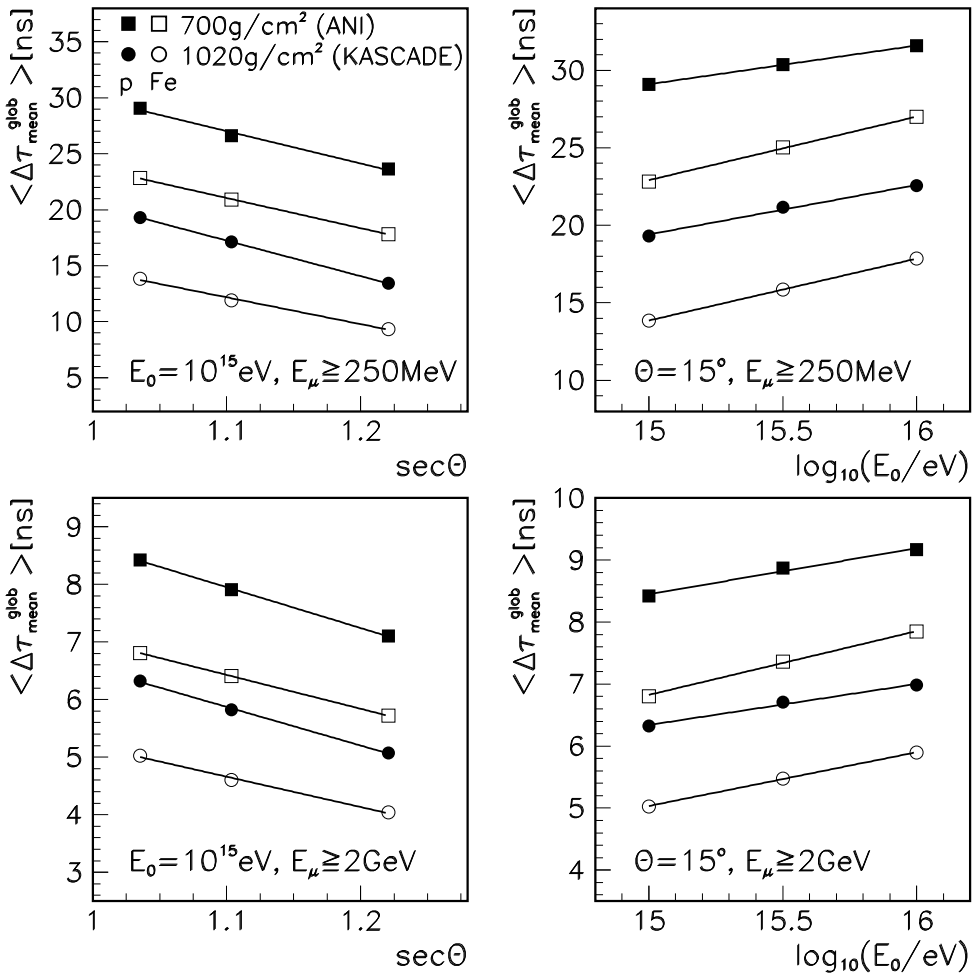

Fig. 3.5: The variation of the average $\langle \Delta\tau^{glob}_{mean} \rangle$, with the angle-of-EAS incidence ($sec\theta$) at $E_0 = 10^{15}$ eV and with $log_{10}E_0$ for $\theta = 15°$.

induced air shower (starting at higher altitude) are smaller as compared with those corresponding to a proton induced air shower. The smaller interaction length for iron imply also smaller fluctuations because almost all iron showers are initiated in a more restricted range of altitude. Muon arrival times are smaller for smaller altitudes because the travel path of muons become longer (see eq. 2.5). Fig. 3.4 shows global times, but the calculation of local time

quantities reveals the same main features: smaller values and fluctuations in the case of heavy-primary induced showers. This behaviour favorises, in principle, primary mass discrimination based on muon arrival times.
From distributions of time quantities $T(R_\mu = 90 \div 110$ m) on the type presented in Fig. 3.4 for $T \equiv \Delta\tau^{glob}_{mean}$ (given for various observation levels by the simulations for different primary energies and zenith angles) the variation of the averages with $sec\theta$ and $log_{10}E_0$ is determined. Examples are shown in Fig. 3.5 for the muon distributions with $E_\mu \geq 250$ MeV and $E_\mu \geq 2.0$ GeV at KASCADE and ANI levels. As shown by Fig. 3.5, mean muon arrival times decrease with $sec\theta$ and increase with $log_{10}E_0$; for more inclined showers (higher $sec\theta$) it is clear that the travel path of muons is longer and (see eq. 2.5) their arrival times are smaller; with increasing primary energy E_0 the shower penetrates deeper in the atmosphere (see Fig. 3.2) and, because of this, there are more delayed muons, coming from lower altitude. The variations of the time quantities with $sec\theta$ and $log_{10}E_0$ can be linearly approximated and their slopes, $\epsilon_\theta = \partial T/\partial log_{10}E_0|_{sec\theta}$ and $\epsilon_E = \partial T/\partial sec\theta|_{E_0}$, are useful in context of an approach propagated by John Linsley [15].

3.5 Linsley's theorem

Linsley [15] and Linsley and Watson [42] have suggested an indirect experimental approach studying D^e_{10}. This approach can be applied to shower parameters which depend on the depth of observation X and on the depth X^e_m of the electromagnetic shower maximum. Linsley suggested that these parameters should not explicitely depend on the primary energy. Walker and Watson [45] scrutinised under this aspect the EAS charge particle component, analysing the time pulses ("rise times") measured with water Cherenkov detectors at the Haverah Park installation. Blake et al. [46] directed their interest to the muon component.
We investigate the EAS muon arrival time distributions as potential observables for Linsley's procedure because they map rather directly the longitudinal EAS development (via time-flight of the muons travelling through the atmosphere), being dependent on distance of the production height from the observation level X (see ref. [17]). Hence arrival time parameters do implicitely depend on the primary energy E_0 and the angle-of-EAS incidence θ (see Sect. 3.4).
For a certain observation level $X_v = X \cdot cos\theta$, an arrival time quantity T can

be written, defining the functions f^e, f^μ and ϕ by:

$$T = f^{(e,\mu)}(X, X_m^{(e,\mu)}) = \phi(X, log_{10}E_0) \tag{3.6}$$

Thus

$$dT = \partial f^{(e,\mu)}/\partial X|_{X_m^{(e,\mu)}} \cdot dX + \partial f^{(e,\mu)}/\partial X_m^{(e,\mu)}|_X \cdot D_{10}^{(e,\mu)} \cdot dlog_{10}E_0 \tag{3.7}$$

and

$$dT = \partial T/\partial X|_{E_0} \cdot dX + \partial T/\partial log_{10}E_0|_X \cdot dlog_{10}E_0 \tag{3.8}$$

It results:

$$\begin{aligned} \partial T/\partial log_{10}E_0|_X &= D_{10}^{(e,\mu)} \cdot \partial f^{(e,\mu)}/\partial X_m^{(e,\mu)}|_X \\ \partial f^{(e,\mu)}/\partial X|_{X_m^{(e,\mu)}} &= \partial T/\partial X|_{E_0} \end{aligned} \tag{3.9}$$

Denoting the vertical atmospheric thickness X_v (=1020 g/cm^2 for sea level), at a given observation level $X = X_v/cos\theta$ *the change of* T *with the energy* E_0 *is proportional to the variation of* T *with* $X_m^{(e,\mu)}$.
At observation level we do not observe $\partial T/\partial X_m^{(e,\mu)}$, but $\partial T/\partial X$, which could be related to each other, if we could specify the function $f^{(e,\mu)}(X, X_m^{(e,\mu)})$

$$F^{(e,\mu)} = -(\partial f^{(e,\mu)}/\partial X_m^{(e,\mu)})_X/(\partial f^{(e,\mu)}/\partial X)_{X_m^{(e,\mu)}} \tag{3.10}$$

and from eqs. 3.9-3.10:

$$\partial T/\partial log_{10}E_0|_X = -F^e \cdot D_{10}^e \cdot 1/X_v \cdot \partial T/\partial sec\theta|_{E_0} \tag{3.11}$$

$$\partial T/\partial log_{10}E_0|_X = -F^\mu \cdot D_{10}^\mu \cdot 1/X_v \cdot \partial T/\partial sec\theta|_{E_0} \tag{3.12}$$

Obviously in order to derive from the energy variation of the studied arrival time quantity information about the elongation rate, some knowledge is required about $F^{(e,\mu)}$, in addition to the variations with the depth of observation and the zenith-angle dependence, respectively. In a similar way the fluctuations $\sigma(X_m^{(e,\mu)})$ of $X_m^{(e,\mu)}$, which could indicate the change of the mass composition of primary cosmic rays, can be related to the fluctuations $\sigma(T)$ of T:

$$\sigma(T) = -\delta X_m^{(e,\mu)} \cdot F_\sigma^{(e,\mu)}/X_v \cdot \partial T/\partial sec\theta|_{E_0} \tag{3.13}$$

The quantity $F_\sigma^{(e,\mu)}$ is the corresponding scaling factor for the fluctuations of $F^{(e,\mu)}$.
Two extreme forms of $f(X, X_m) = f(X - X_m)$ or $f(X, X_m) = f(X/X_m)$ have been proposed [45] with $F = 1$ or $F = X/X_m$, respectively. At a closer look these simple assumptions do not appear convincingly accurate. Due to the stochastic character of the EAS cascade the form of $f(X, X_m)$ is not well defined. In addition though muon arrival times do depend in a relatively simple way from travel distances, the dependence from the traversed grammage $(X - X_m)$ is more complicated due to the barometric profile of the atmosphere (see also Appendix A). It is just the goal of the present study to scrutinize this aspect.

3.6 The question of the scaling factor

Using these coefficients ϵ_θ and ϵ_E characterising the variation of the mean or quantile distributions (median, first quartile and third quartile) with the energy and the angle of EAS incidence and adopting the above derived values for the elongation rate, the scaling parameter values are deduced. This information would be, in turn, a prerequisite to evaluate experimental data in terms of the elongation rate. Tab. 3.1 presents the detailed dependence with θ and E_0 for F^e and F^μ factors $(F^{(e,\mu)} = -\epsilon_\theta \cdot X_v/(\epsilon_E \cdot D_{10}^{(e,\mu)}))$ in case of $\Delta\tau_{mean}^{glob}$ for muons with $E_\mu \geq 2$ GeV. The uncertainities of these values are arising from the fit procedure and are estimated in the range of 10%. The result deviating from the expectation of a simple dependence from $X - X_m$ is plausible, since the arrival times depend from the *geometrical* distance of the height of production and the observation level. A transformation into the dependences from X and X_m involves the particular direction of the muon path in the atmosphere and the variation of the density of the atmosphere. That complicates the relation.
For more detailed description of the behaviour of F, mean values $\langle F^e \rangle$ and $\langle F^\mu \rangle$ have been calculated for all time parameters under consideration (global and local mean, median, first and third quartile distributions) using the mean values of coefficients ϵ_θ (averaged three angles) and ϵ_E (averaged three energies), (see Tab. 3.2).
Obviously $F^{(e,\mu)}$ proves to be dependent from:

- the EAS inducing primary, i.e. from the height of maximum $X_m^{(e,\mu)}$: $F_{Fe}^{(e,\mu)} > F_p^{(e,\mu)}$;

- the atmospheric depth of the observation level X: $F^{(e,\mu)}$ increases with X;
- the energy threshold of muon detection;
- the dependence is different for various quantities of the muon arrival time distributions.

Ignoring some "stray shots", which may arise from fluctuations within a limited sample of simulated showers, we may tentatively infer the tendencies, that F for different observation levels scales with X and for different

$\langle \Delta\tau^{glob}_{mean} \rangle$			ANI		KASCADE		ANI		KASCADE	
	θ	E_0(PeV)	F^e	X/X^e_m	F^e	X/X^e_m	F^μ	X/X^μ_m	F^μ	X/X^μ_m
P	15°	1.	1.11	1.38	1.49	1.99	1.00	0.94	1.35	1.34
		3.16	1.02	1.31	1.34	1.87	0.93	0.89	1.22	1.28
		10.	1.09	1.23	1.41	1.76	0.99	0.86	1.28	1.22
	25°	1.	1.08	1.48	1.32	2.11	0.98	1.00	1.20	1.43
		3.16	1.00	1.39	1.19	1.99	0.91	0.95	1.08	1.36
		10.	1.07	1.31	1.25	1.87	0.97	0.91	1.13	1.30
	35°	1.	1.09	1.63	1.36	2.33	0.99	1.10	1.19	1.58
		3.16	1.01	1.54	1.19	2.20	0.91	1.05	1.08	1.51
		10.	1.07	1.45	1.24	2.07	0.97	1.01	1.13	1.44
Fe	15°	1.	1.54	1.91	2.08	2.73	1.24	1.13	1.67	1.62
		3.16	1.47	1.73	1.93	2.47	1.18	1.04	1.55	1.49
		10.	1.44	1.58	1.78	2.26	1.15	0.98	1.43	1.40
	25°	1.	1.43	2.04	1.94	2.91	1.15	1.21	1.55	1.72
		3.16	1.37	1.84	1.80	2.64	1.10	1.11	1.44	1.59
		10.	1.34	1.68	1.66	2.41	1.07	1.04	1.33	1.49
	35°	1.	1.42	2.25	1.67	3.22	1.14	1.33	1.34	1.91
		3.16	1.36	2.04	1.55	2.91	1.09	1.23	1.25	1.76
		10.	1.32	1.86	1.43	2.66	1.06	1.15	1.15	1.65

Tab. 3.1: Values of the scaling parameters F^e, F^μ for the global mean arrival time of EAS muons ($E_\mu \geq 2$ GeV) for different observation levels and primaries deduced on basis of Monte Carlo simulations. X/X_m is the ratio of the depth of observation level to the depth of EAS component maximum inferred from the simulations.

$\langle T \rangle$		$E_\mu \geq 250$ MeV				$E_\mu \geq 2$ GeV			
		ANI		KASCADE		ANI		KASCADE	
		$\langle F^e \rangle$	$\langle F^\mu \rangle$	$\langle F^e \rangle$	$\langle F^\mu \rangle$	$\langle F^e \rangle$	$\langle F^\mu \rangle$	$\langle F^e \rangle$	$\langle F^\mu \rangle$
P	$\langle \Delta\tau^{glob}_{mean} \rangle$	1.06	1.05	1.33	1.31	1.06	0.96	1.30	1.18
	$\langle \Delta\tau^{glob}_{0.25} \rangle$	1.01	0.99	1.32	1.30	1.01	0.91	1.31	1.19
	$\langle \Delta\tau^{glob}_{0.50} \rangle$	1.04	1.02	1.33	1.31	1.05	0.95	1.34	1.22
	$\langle \Delta\tau^{glob}_{0.75} \rangle$	1.10	1.08	1.34	1.32	1.13	1.03	1.39	1.26
	$\langle \Delta\tau^{loc}_{mean} \rangle$	1.15	1.13	1.41	1.39	1.44	1.31	1.70	1.55
	$\langle \Delta\tau^{loc}_{0.25} \rangle$	1.40	1.38	1.96	1.93	1.67	1.52	2.21	2.01
	$\langle \Delta\tau^{loc}_{0.50} \rangle$	1.20	1.18	1.59	1.56	1.43	1.30	1.81	1.64
	$\langle \Delta\tau^{loc}_{0.75} \rangle$	1.16	1.14	1.43	1.41	1.42	1.29	1.66	1.51
Fe	$\langle \Delta\tau^{glob}_{mean} \rangle$	1.37	1.19	1.65	1.44	1.41	1.13	1.75	1.41
	$\langle \Delta\tau^{glob}_{0.25} \rangle$	1.49	1.30	1.88	1.64	1.51	1.21	1.89	1.52
	$\langle \Delta\tau^{glob}_{0.50} \rangle$	1.44	1.26	1.81	1.58	1.44	1.16	1.80	1.44
	$\langle \Delta\tau^{glob}_{0.75} \rangle$	1.42	1.24	1.82	1.59	1.43	1.15	1.78	1.43
	$\langle \Delta\tau^{loc}_{mean} \rangle$	1.41	1.23	1.70	1.48	1.60	1.28	1.99	1.59
	$\langle \Delta\tau^{loc}_{0.25} \rangle$	1.75	1.53	2.37	2.07	1.90	1.53	2.51	2.01
	$\langle \Delta\tau^{loc}_{0.50} \rangle$	1.55	1.35	2.01	1.76	1.64	1.32	2.09	1.68
	$\langle \Delta\tau^{loc}_{0.75} \rangle$	1.45	1.27	1.89	1.65	1.55	1.24	1.93	1.55

Tab. 3.2: Mean values of the scaling parameters F^e and F^μ for different time parameters (global and local), two energy thresholds for muons (0.25 GeV and 2.0 GeV), proton and iron induced EAS, and two observation levels (ANI and KASCADE).

primaries with the maximum depth $\langle X_m \rangle$, associated with the mass of the primary.

3.7 Outlook to the analysis of experimental muon arrival time distributions

The present study reveals the principal relation between the arrival time distributions of EAS muons and the characteristics of the longitudinal EAS profile, and it scrutinizes a method proposed in ref. [15, 42] for an indirect determination of the elongation rate (characterising the variation of the atmospheric depth X_m of the shower size maximum with the primary energy)

and of the fluctuations of the shower height maximum from observations of arrival time distributions of the EAS muons. The relation between the time observables and the longitudinal EAS profile implies a scaling factor F, which proves to depend from the height X_m of the shower maximum and the observation level X.
In previous studies a simple relation has been conjectured, with the hope of a nearly model independent access to the longitudinal EAS development. The present results display a complex behaviour of F, varying with the variation of X and X_m, neither being simply constant nor transparently dependent from the ratio X/X_m. Practically there is no evident analytical relation between F, X and X_m. This complex behaviour may arise from the complex mapping of the atmospheric depth by the geometric path lenghts (directly affecting the time of flight of the muons)(see also Appendix A). We conclude that the application of the Linsley's procedure to data is unfortunately affected by this uncertainty in F and finally needs unavoidably comparisons with Monte Carlo predictions, thus introducing all model dependence. A systematic Monte Carlo based analysis, however is expected to extract more details about the longitudinal EAS profile. This is the main goal of the analysis of the experimental data done in this work.

4. KASCADE EXPERIMENT

The experiment KASCADE (**KA**rlsruhe **S**hower **C**ore and **A**rray **DE**tector) is located in Karlsruhe, Germany, at 8° E, 49° N, 110 m a.s.l. The detectors are distributed on a field of 200×200 m^2 large. The coverage efficiency is 2.5% for muons, 2.0% for electrons-photons and 0.6% for hadrons.
The expected rates for showers with the core inside the array are 2 s^{-1} for $E_0 > 10^{14}$ eV and 20 h^{-1} for $E_0 > 10^{16}$ eV. KASCADE comprises three main parts (see Fig. 4.1):

- the Field Array
- the Central Detector
- the Muon tunnel

4.1 Array

The detector array (Fig. 4.1), for sampling the electromagnetic and muonic EAS components, consists of 252 detector stations (see Fig. 4.2). The electronic readout of the detectors in the stations is organised in 16 clusters of 16 stations (only 15 stations for the central 4 clusters). These clusters act as independent air shower arrays. A station which belongs to an inner cluster contains four circular detectors (filled with scintillation liquid) for the e/γ component (5 MeV threshold), with a total area of about 3.2 m^2 and 5 cm thickness. Each detector is viewed by a photomultiplier from above.
Stations which belong to one of the outer 12 clusters contain only two e/γ detectors. Below the e/γ detectors there is an absorber of 10 cm of lead and 4 cm of iron corresponding to more than 20 radiation lengths and to a muon threshold of about 230 MeV. The 3.2 m^2 muon detector below this shielding consists of 4 sheets of plastic scintillator, $90 \times 90 \times 3$ cm^3 each, read out by green wavelength shifter bars and phototubes.
The trigger condition [48] is delivered by a cluster detector multiplicity n of

32 e/μ detectors or m of 60 in the inner 4 clusters (15 e/μ detectors each).

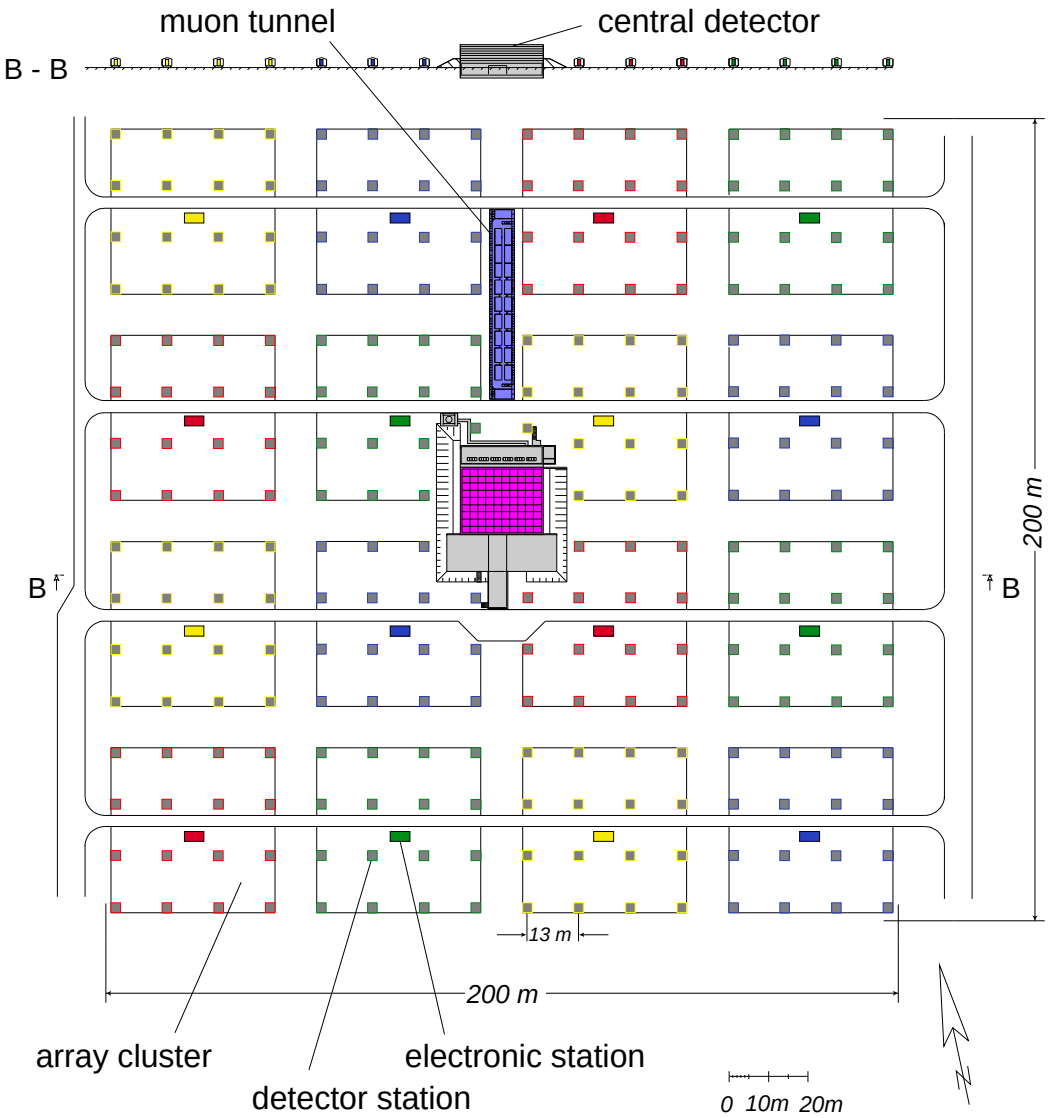

Fig. 4.1: General lay-out of the KASCADE experiment. B-B is a vertical section through KASCADE in the central region.

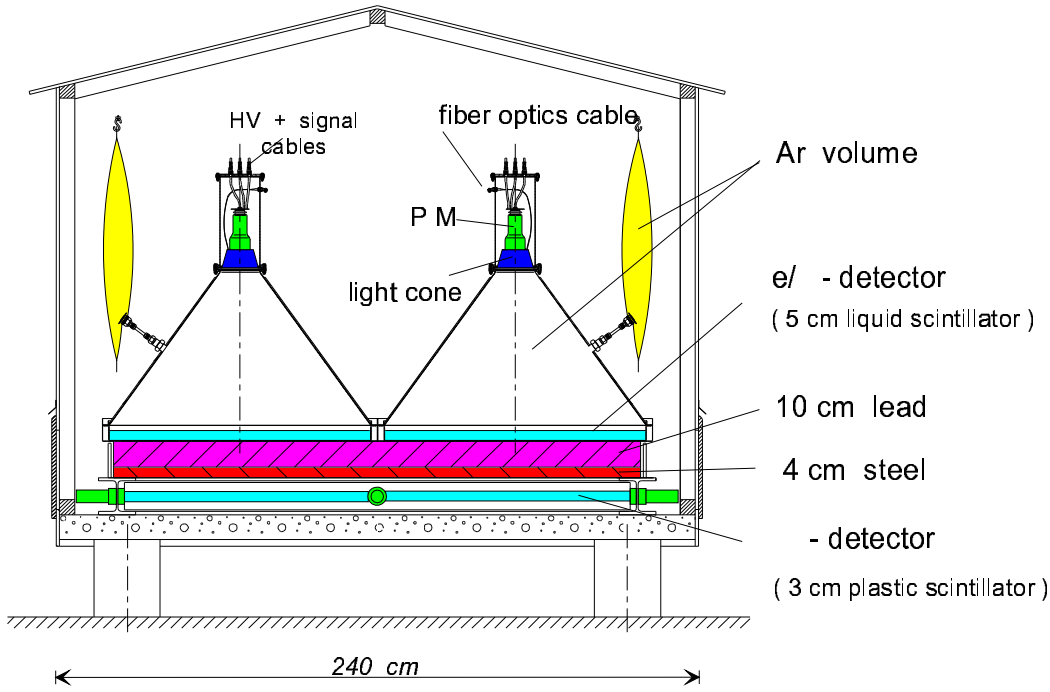

Fig. 4.2: Sketch of a KASCADE array detector station.

4.2 Central Detector

The Central Detector (see Fig 4.3) consists of a hadron calorimeter, a top cluster, a trigger plane and a multiwire proportional chambers (MWPC) system in the basement below for muon detection.
The hadron calorimeter is an iron absorber block with 16×20 m^2 lateral dimension and a depth of about 4 m. The iron block has 8 horizontal gaps. Seven of them contain together 40000 ionization chambers ($25 \times 25 \times 1$ cm^3 each) filled with the room temperature liquid tetramethylsilane (TMS) and tetramethylpentane (TMP) as dielectric. They are the active elements of the calorimeter for hadronic energy measurements. The hadron calorimeter is equivalent to 11 nuclear interaction lengths for vertical protons. According to MC calculations, the energy resolution varies slowly from 20% at 100 GeV to 10% at 10 TeV [49].
A trigger layer of 456 scintillation detectors is placed in the third gap of the

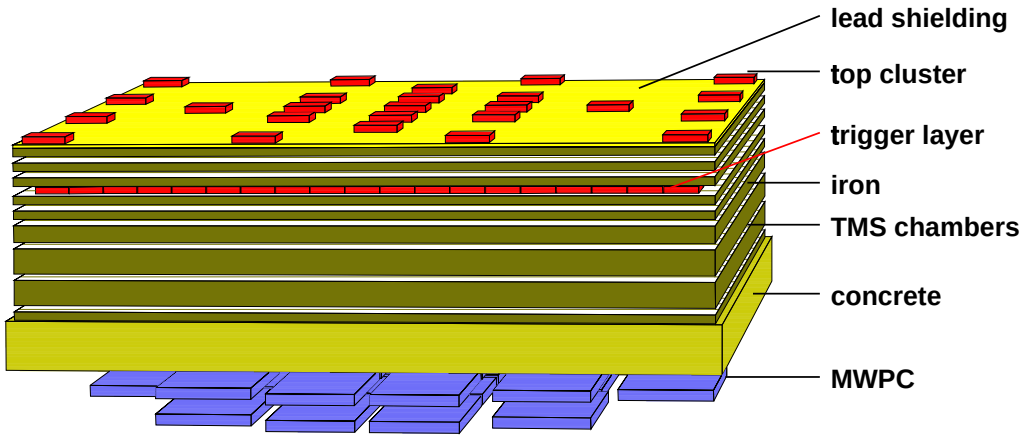

Fig. 4.3: KASCADE Central Detector.

iron block at a depth corresponding to a mean energy threshold [1] for muons of 490 MeV [50]. Each scintillation detector contains two sheets of 3 cm thickness and 0.45 m^2 in total area with a read out by a green wavelength shifter bar and an 1.5-inch photomultiplier. Two neighbouring detectors are shielded in a box (Fig 4.4). Scintillation detectors cover together 64% of the total area of the Central Detector. They provide fast trigger signals for the Central Detector. Their data are analysed for the present time measurements. In addition, this detector layer is used as dE/dx detector for charged particles.
The MWPC system [51] consists of 32 large-area multiwire proportional chambers installed below the iron sampling calorimeter in two layers of 129 m^2 area each, with a telescope effect, improving the reconstruction quality of the particle hits and giving information about the mean direction. The anodes of the MWPC system consist of 20 μm thick gold plated tungsten wires. The distance between the anode wires is 12 mm and they are separated by gold-plated copper-beryllium potential wires of 100 μm diameter. The wires are connected to the readout electronics by printed boards. As cathodes 10.6 mm broad copper stripes on a printed circuit foil are glued on the upper and lower cover panels of the chambers at an angle of +34° or

[1] It means that vertical particles with a kinetic energy of the energy threshold reach the detetector with a probability of 50%.

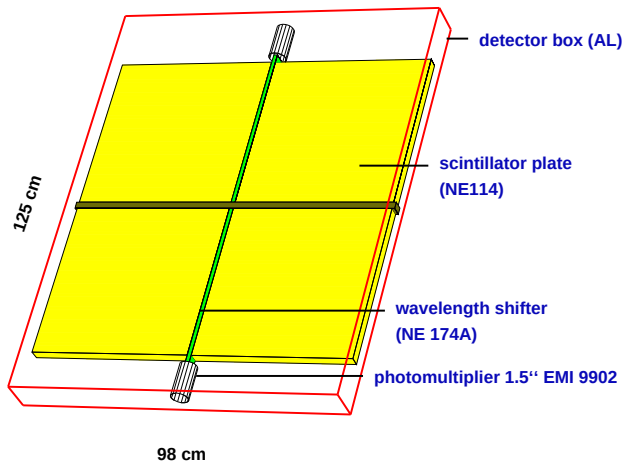

Fig. 4.4: Scintillation detectors of the trigger layer.

$-34°$, respectively, with respect to the anode wires. The gap between the cathode stripes is 2 mm. The chamber read out can be triggered from the trigger layer or from the top cluster.
Correlated measurements of the trigger layer and MWPC system allow to study lateral and time distributions of the muon component with a 2.4 GeV energy threshold (see Sec. 5.1 for more details). The muon arrival time distributions measured by the trigger layer combined with the muon identification by the MWPC facilities are the focus of the present work.
The top cluster above the calorimeter, formed of 50 scintillation detectors of the same type as of the trigger layer, is used for the measurement of small central showers with sizes below the array threshold.

4.3 Muon tunnel

The muon tunnel (50×5.5 m^2) is situated in the northern part of the Central Detector. The tunnel is below a shielding made out of concrete, iron and soil. A multilayer of 6 iron plates of 3 cm thickness, separated each by 5 cm sand provides a good absorber for a large fraction of low energy electromagnetic particles and corresponds to an energy threshold of 0.8 GeV for muons. A large area streamer tube (ST) Muon Tracking Detector (MTD), located in

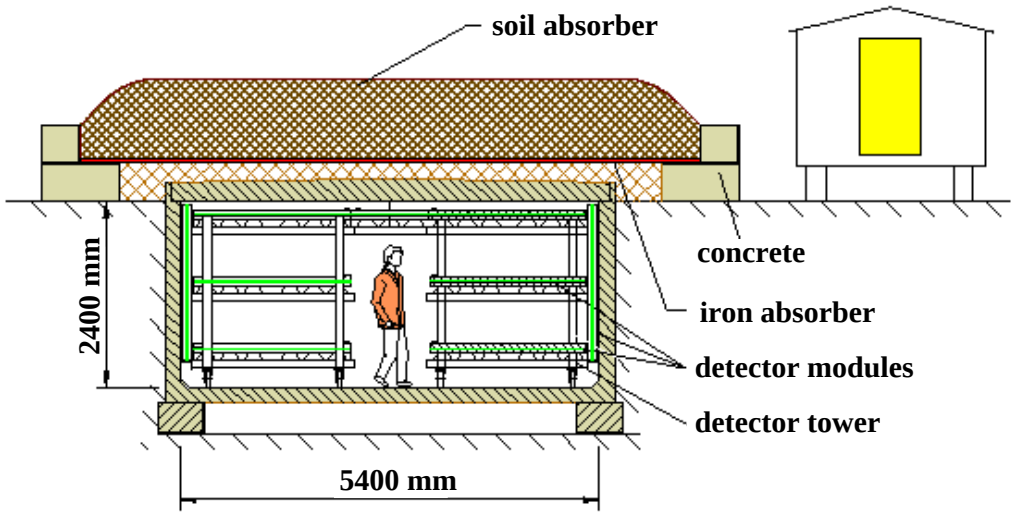

Fig. 4.5: Vertical section of the muon detector tunnel.

the muon tunnel, was put into opperation. The detector is used for the determination of the size and the lateral distribution of the muon component in EAS and to estimate (by triangulation) the muon production heights (an observable which depend on the primary mass). The resolution of the muon tracking is about 0.6° [47]. A cross section of the tunnel (together with an array detector station located nearby) is shown in Fig. 4.5. The ST chambers have been built housing 16 anode wires in 2 cathode comb profiles, extruded for 8 parallel ST cells of 9×9 mm^2 cross section and 4000 mm length. A so-called module (2×4 m^2) contains 12 ST chambers. Above the ST chambers there is a layer of a rigid polyester foil of 75 μm thickness with evaporated aluminium strips of 18 mm width and 2 m length, perpendicular to the wires. Four modules, three positioned horizontally spaced by 820 mm and one arranged vertically, form a muon telescope called detector tower. The whole detector consists of 16 towers arranged in two rows.

4.4 Shower event reconstruction

The general shower parameters are reconstructed from the array data following a procedure with three iterations:

- the centre of gravity of the registered energy signals of the e/γ detectors defines the shower core position. The direction of the shower is calculated out of the arrival times by assuming a plane shower front. N_e and N_μ are determined by summing up the relevant signals of e/γ and muon detectors. These signals are weighted with a geometrical dependent factor.

- the shower direction is reconstructed on a further step by fitting the time signals of the e/γ detectors with a conical shower front. From this fit also the arrival time of the electromagnetic front of the shower core is obtained. The core position is fitted together with the electron shower size and the electron lateral shape parameters by an NKG-form [35].

- the e/γ detector signals are corrected by removing contributions coming from particles others than electrons, and muon detector signals are corrected for expected electromagnetic and hadronic punch-through. Signals largely inconsistent with those from neighbouring detectors are excluded; also signals with times more than 200 ns off from the shower core arrival time are discarded. The same fits as in the second iteration are performed with the corrected signals. Due to the corrections the results of the third iteration are improved.

The core position can be reconstructed with an uncertainty of about 3 m at 1 PeV, and the accuracy is typically better than 1 m for showers above 4 PeV if the core is located well inside the array. The angular resolution for such showers is about 0.4° [50]. The complete EAS event reconstruction includes also the observables measured by the Central Detector: lateral, energetical and angular distributions for hadrons and lateral, angular and temporal distributions for muons (with 490 MeV and 2.4 GeV energy thresholds).
The shower reconstruction is technically implemented in the KRETA code (**K**ASCADE **R**econstruction of **Ex****T**ensive **A**irshowers). The calibration of the detectors is included also in the KRETA code. Simulated and experimental data are treated identically by this code. Concerning simulated data, after adopting the interaction models in CORSIKA program (simulating the atmospheric development of the Extensive Air Showers), a complex simulation of the response of the KASCADE detector is required. The CRES code (**C**osmic **R**ay **E**vent **S**imulation), based on GEANT3 [33], is used for this detector simulation. Shower data from CORSIKA (energy, position and

incident angle of each particle hitting a detector) are used as input to CRES. In principle, after CRES, simulations are at the same level (of consistency) as measured data (raw data) (see Fig. 4.6).
The observables reconstructed for experimental and simulated showers are used furtheron in parametric comparisons or in multivariate analyses. Mul-

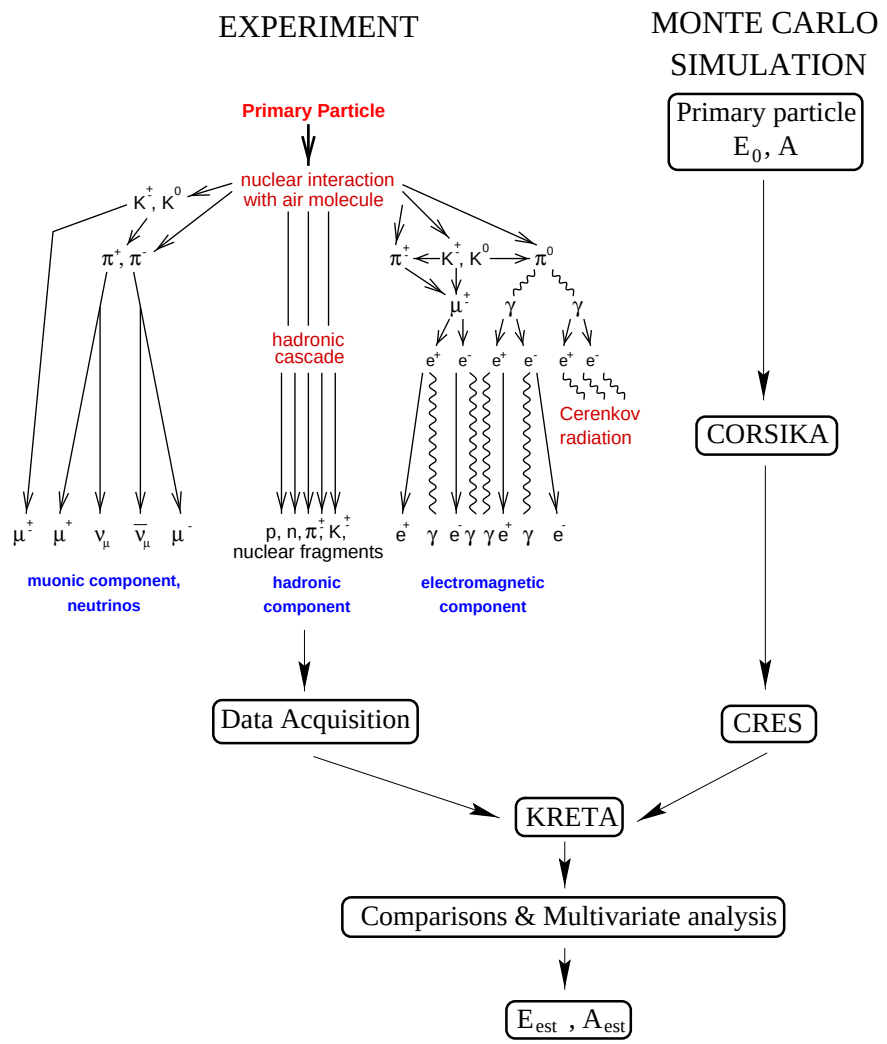

Fig. 4.6: Sketch of the general analysis of EAS observables measured in the KASCADE experiment.

tivariate analyses take into account the correlations between observables and also the intrinsic fluctuations of the EAS events (see Chapter 7).

4.4.1 Primary energy estimator

A very important problem in EAS analyses is to define an adequate quantity (a combination of some EAS observables) which can be used as estimator of the primary energy. As shown by simulation studies, the number of EAS muons with 230 MeV energy threshold and integrated in the range of 40 to 200 m distance from the shower core, the so-called truncated muon number N_μ^{tr}, proves to be such a parameter for the KASCADE experiment, being practically mass independent in the range of 10^{14} to 10^{16} eV [52, 53]. This is due to a fortunate compensation of various effects in the lateral distribution. The energy threshold of 230 MeV for muons corresponds to the muon detectors of the array. The lower geometrical limit avoids the severe (electromagnetic and hadronic) punch-through effect near the shower axis (which disturbs muon identification) while the upper one corresponds to geometrical limits of the KASCADE array size. Statistical sampling errors when estimating N_μ^{tr} improve from about 20% at 1 PeV to about 10% at 10 PeV (primary energy) [50].

5. GENERAL PROCEDURES FOR ANALYSING MUON ARRIVAL TIMES

5.1 Muon arrival time measurements at KASCADE

The Central Detector facilities – trigger layer and MWPC system – are used for muon position and arrival time measurements at the KASCADE experiment. The trigger layer works like an "eye" with 456 pixels (scintillation detectors). The scintillation detectors of the trigger layer are used for time measurements with a time resolution of around 1.5 ns after an energy deposit correction [22]. A simple arrangement with two scintillation detectors placed at a vertical distance of 2.5 m one above the other has been used to

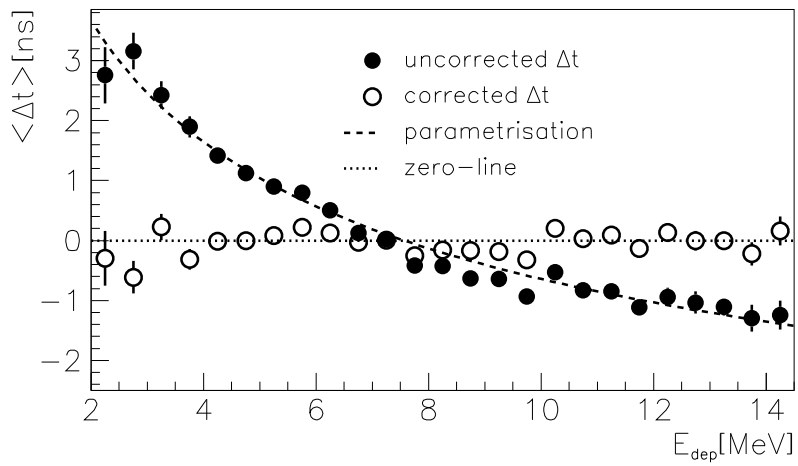

Fig. 5.1: Measured difference time between the two detectors as a function of the energy deposit in the lower detector. The quality of the correction is examined by comparison with the zero-line [22].

estimate the time resolution and the energy deposit correction. A distribution is obtained by measuring the time-of-flight (Δt) of muons between these two detectors; this distribution can be approximated with a gaussian with σ_2 =2.35 ns. The time resolution of a single detector can be easily calculated: $\sigma_1 = \frac{\sigma_2}{\sqrt{2}}$ =1.66 ns. There is a clear dependence of the measured times on the deposited energy. Fig. 5.1 shows the dependence of ($\langle \Delta t \rangle$) with the deposited energy in the lower detector. This dependence can be parametrisated by [22]:

$$\Delta t = a - (b \cdot \frac{\sqrt{E_{dep}/\mathrm{MeV}}}{\sqrt{E_{dep}/\mathrm{MeV}} + c}) \tag{5.1}$$

The parameter a corresponds here only to a shift and serves to the adjustment of parametrisation to the measured values; it results b =26 ns and $c = 0.88$. The corrected times are well distributed around the zero-line (Fig. 5.1). The time resolution of the total system improves from 2.35 ns to 2.06 ns by using energy deposit corrected times. This corresponds to a time resolution of $\simeq$1.5 ns for the single detector.

If the energy deposit in one of the detectors corresponds to more than 300 MeV (50 m.i.p.), a so-called hadron trigger is build. The second possibility is a muon multiplicity trigger when at least 8 of the 456 detectors have signals larger than $\frac{1}{3}$ m.i.p. [49]. The positions of the plastic scintillators from the trigger layer providing time signals are correlated with particle tracks reconstructed by the MWPC system with an accuracy of about 1° [51]. Accepted tracks are required to be in resonable agreement ($\Delta\theta \leq 15°$; $\Delta\phi \leq 45°$ if $\theta \geq 10°$) with the shower direction, determined from the array. Thereby, ambiguous hits are efficiently solved. If the multiplicity of fired anodes and cathodes in a given area of the chambers is too large to separate different hits, a so-called "cluster" is reconstructed. The position of such a cluster is defined as the intersection of the centres of gravity of the fired wires and stripes; also "clusters" tracks (hadrons) are reconstructed. However, more than 99% of all triggered events have a muon density below $1/\mathrm{m}^2$ where ambiguity effects or hadronic punch-through are negligible [51]. For the muon case, the absorber of the calorimeter (5 cm lead, 172 cm steel and 77 cm concrete) leads to a threshold of 2.4 GeV (for vertical trajectories). The trajectories of such muons are traced back through the Central Detector up to the trigger layer and in the case they hit detectors of the trigger layer with measured energy deposits compatible for muons, the corresponding measured arrival times in the trigger layer are associated. The MC simula-

tions show that about 75% of the 2.4 GeV muon tracks in the MWPC have a correlated signal in the trigger layer. These correlated muons have been considered in the present work to investigate the time structure of the EAS muon component. An amount of 24.000.000 (KRETA input) experimental shower events have been used for analysis, from a period of aquisition during $28.05.97 \div 30.06.98$. For the arrival time analysis, at least $n = 3$ detectors of the trigger layer are required to have a signal which can be correlated with muon tracks in the MWPC. Measurements of the muon component at small core distances could be affected by the hadrons in the shower core and by the electromagnetic punch-through. Because the MWPC system is positioned deep below the iron sampling calorimeter, the contribution of the electromagnetic punch-through is found to be negligible [22]. But cascading hadrons distort the relative arrival time distributions. A veto for a large energy deposit in the scintillator detectors $E_{dep} \geq 20$ MeV (c. 3 m.i.p.) has been applied in order to suppress "muon signals" produced by cascading hadrons. This procedure remedies the distortion effect in the shower centre [21].

5.2 Complete simulations for KASCADE

Complete air shower simulations including the detector response have been performed for comparisons with measured data. CORSIKA vers. 5.621 has been used, including the GHEISHA code as generator for low energy hadronic interactions, QGSJET as generator for high-energy hadronic interactions and EGS4 Monte Carlo procedure for the simulation of the electron-photon component. EAS for three primaries have benn simulated: proton (H) for light group, oxygen (O) for CNO group and iron (Fe) for heavy group. Seven energy bins:

$$\begin{aligned}
&5.00 \cdot 10^{14}\ \text{eV} \div 1.40 \cdot 10^{15}\ \text{eV}, \quad 8.36 \cdot 10^{14}\ \text{eV} \div 2.33 \cdot 10^{15}\ \text{eV},\\
&1.40 \cdot 10^{15}\ \text{eV} \div 3.90 \cdot 10^{15}\ \text{eV}, \quad 2.33 \cdot 10^{15}\ \text{eV} \div 6.51 \cdot 10^{15}\ \text{eV},\\
&3.90 \cdot 10^{15}\ \text{eV} \div 1.09 \cdot 10^{16}\ \text{eV}, \quad 6.51 \cdot 10^{15}\ \text{eV} \div 1.82 \cdot 10^{16}\ \text{eV},\\
&1.09 \cdot 10^{16}\ \text{eV} \div 3.06 \cdot 10^{16}\ \text{eV}
\end{aligned}$$

and three zenith angle intervals:

$$0^\circ \div 15^\circ, \quad 15^\circ \div 20^\circ, \quad 20^\circ \div 40^\circ$$

have been considered. Two areas where the shower cores are positioned have been especially simulated:

- $cut1$: $0 \leq D_{core} \leq 95$ m;
- $cut4$: 80 m $\leq D_{core} \wedge \mid X_{core} \mid \leq 105$ m $\wedge \mid Y_{core} \mid \leq 105$ m. [1]

X_{core} and Y_{core} are the coordinates of the shower core in the plane of the KASCADE experiment: $D^2_{core} = X^2_{core} + Y^2_{core}$. The center of the Central Detector is located at $(0, 5.19)$ m. $Cut4$ corresponds mainly to shower core positions in the corners of the KASCADE array.
For each primary type there are $\simeq$ 5000 showers for each $E_0 \times \theta$ bin, except for the bins of the highest energies ($6.51 \cdot 10^{15} \div 1.82 \cdot 10^{16}$ eV with $\simeq$ 2500 simulated showers and $1.09 \cdot 10^{16} \div 3.06 \cdot 10^{16}$ eV with $\simeq$ 1250 simulated showers). In fact there are 25 times less CORSIKA showers but the position of the core of each shower is randomly generated 10 times in $cut1$ and 15 times in $cut4$. For a certain primary (proton, oxygen, iron) a "spectrum" has been built over all simulated θ, E_0 and D_{core} intervals ($0° \leq \theta \leq 40°$, $5.00 \cdot 10^{14} eV \leq E_0 \leq 3.06 \cdot 10^{16} eV$, $\{D_{core} \mid D_{core} \in cut1 \cup cut4\}$). A certain weight has been assumed for each event according to the dependence:

$$dN = const. \cdot E_0^{-\gamma} sin\theta D_{core} dE_0 d\theta dD_{core} \tag{5.2}$$

dN is the number of primaries with energy between $E_0, E_0 + dE_0$, zenith angle between $\theta, \theta + d\theta$, intersecting the plan of the KASCADE array between $D_{core}, D_{core} + dD_{core}$. An identical spectral index $\gamma = 2.7$ over the whole primary energy range is considered for all primaries (H, O, Fe) as a simple assumption on the primary energy spectra used for the muon arrival times comparisons in this section. A parametrisation of the spectral index around the "knee"

$$\gamma = \begin{cases} 2.7 & : \quad \text{for } E \leq E_{knee} \\ 3.1 & : \quad \text{for } E > E_{knee} \end{cases}$$

$$E_{knee}(Z) = Z \cdot 4 \cdot 10^{15} \text{ eV} \tag{5.3}$$

with Z being the atomic number of the primary nucleus has been used to increase the consistency in the analysis from Chap. 7, studying primary mass composition. Dependence 5.2 has been considered at the top of the atmosphere; absorbtion in the atmosphere and event reconstruction (detector eficiency) have been taken into account.
Because of the limited energy range of the simulations, a certain N_μ^{tr} interval

[1] "$\wedge$" represents the logical operator "AND".

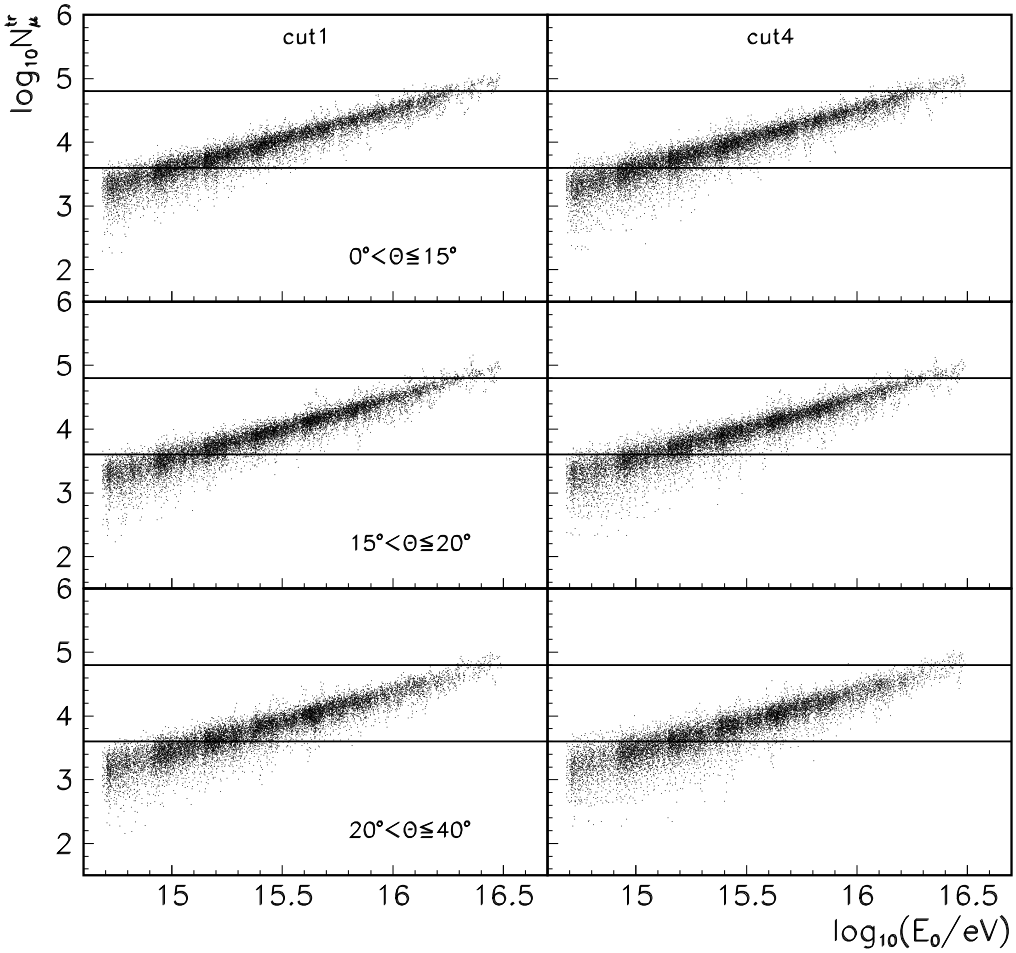

Fig. 5.2: N_μ^{tr} range (between the horizontal lines) used for furtheron analysis. Proton, oxygen, iron induced showers have been plotted together; a weight=1 has been considered for each event.

has been considered (between horizontal lines in Fig. 5.2):

$$3.60 \leq log_{10} N_\mu^{tr} \leq 4.80 \tag{5.4}$$

Using the condition 5.4, showers of energies outside the simulated range which fluctuate into the range have been eliminated. For example, as horizontal

line $log_{10}N_{\mu}^{tr} = 3.6$ shows, practically no primary having the energy below $5.00 \cdot 10^{14}$ eV (which is the lowest limit in the "spectrum" build above) will give a $log_{10}N_{\mu}^{tr}$ above 3.6 (even at extrem EAS fluctuations).

5.3 Time distributions and multiplicity effects

For a certain EAS event let's consider n muons detected in the MWPC with arrival times measured in the trigger layer. The present studies consider only EAS events with muon multiplicities $n \geq 3$. Because of the jitter of some nanoseconds in estimating the arrival time of the electromagnetic front in the shower core, the arrival time of the foremost muon is choosen as reference, i.e. local muon arrival times are considered. These n local muon arrival times form a "single EAS event distribution". There are two possibilities to analyse the single EAS event distribution:

- For the single EAS event distribution different features T can be calculated. E.g.: mean value ($\Delta\tau_{mean}^{loc}$) and quantiles ($\Delta\tau_{0.25}^{loc}$, $\Delta\tau_{0.50}^{loc}$, $\Delta\tau_{0.75}^{loc}$, as defined in Sec. 2.2). Representing together, for many showers, the values of such a variable T considered in a certain bin ($R_{\mu} \times \theta \times ...$), an "EAS events distribution" is obtained for the variable T.

- Second possibility is to add, for a certain bin ($R_{\mu} \times \theta \times ...$), single EAS event distributions for many showers. The distribution of individual muon arrival times over many showers will be called "single muon arrival time distribution".

It's clear that only the first possibility allows event-by-event analysis including muon arrival times (i.e. muon arrival times variables can be correlated with the other observables of the same shower event). But in an event-by-event consideration intriguing statistical effects enter in the estimate of the properties (like the mean and quantiles) of the probability density function (p.d.f.) from small samples of muons. The arrival time $\Delta\tau_1^{glob}$ of the foremost muon (relative to the fictive zero-time, represented by the arrival time of the electromagnetic front of the shower core) and its fluctuations depend on the particular value of the multiplicity n, systematically increasing the mean values of the local time quantities with increasing n [22]. The fluctuation with the muon multiplicity is relatively small in pure CORSIKA simulations. But it seriously distorts the experimental arrival time distributions as well as the simulated distributions, when the smearing due to the finite time resolution

[22] is taken into account. Fig. 5.3 presents the dependence on the multiplicity of the expectation values $\langle \Delta\tau_1^{glob} \rangle$ of the arrival time of the first muon; the p.d.f of the single muon arrival time distribution is approximated in the figure by a simple Γ-function.
EAS events distributions (for muon arrival time variables) have been analysed in some recent works [21, 56, 55] by applying a correction procedure [22] removing the distortions due to the multiplicity effects arising mainly from the apparatus performance (its time resolution). EAS events distributions (without correction procedure, because the correction procedure for removing multiplicities effects implies some initial assumptions on primary mass composition) are also used in Chapter 7 in an event-by-event nonparametric multivariate analysis in view to estimate the primary mass composition.
For a realistic comparison of simulated and measured data concerning time structure of the muon component of EAS a transformation of local times into global times (see next section) has been prefered because global times are connected in a more intuitive way with the longitudinal profile of the shower. Single global muon arrival time distribution have been prefered because of some fluctuations arising from the strict mathematical definition of quantiles for EAS samples with poor number of muons. The method presented in the next section has also the advantage of a better statistic for

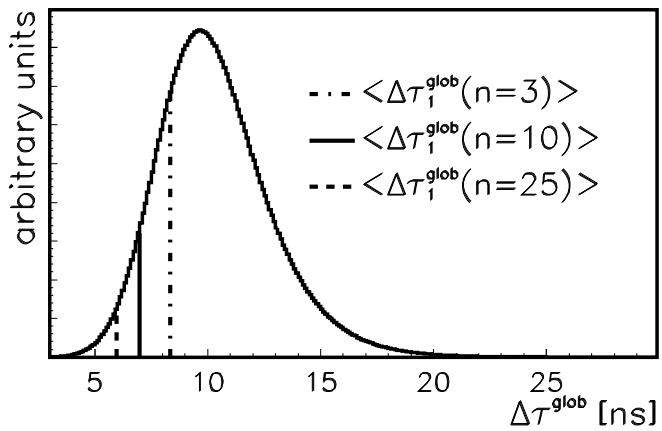

Fig. 5.3: The expectation values $\langle \Delta\tau_1^{glob} \rangle$ of the arrival time of the first muon of a given time distribution for three muon multiplicities [22].

single muon arrival times distribution even in small R_μ bins. In an event-by-event analysis and also for single local muon arrival time distributions R_μ is defined by the centre of the Central Calorimeter while in the next section R_μ will be defined by the positions of the individual muons.

5.4 Transformation of local times into global times

Individual local muon arrival times ($E_{thres} = 2.4$ GeV) detected in the Central Detector are (formally) transformed into individual global arrival times by adopting a certain global time for the foremost muon of this event, coming from a continuum space, over primary energy E_0, primary zenith angle θ, distance of the centre of the Central Detector to the shower core and muon multiplicity n. This continuum space has been build by using CORSIKA simulations (Sec. 5.4.1). The technical procedure and its consistency is presented in Sec. 5.4.2. After the transformation procedure, each of the n muons will be characterised by its global arrival time and its distance to the shower core. Single global muon arrival time distributions are build by representing the individual muon global arrival times for many showers in a certain $R_\mu \times \theta \times ...$ bin. Such distributions and their mean values, standard deviation and quantiles are used in the next chapter to compare measurements with MC predictions.

5.4.1 $\Delta\tau_1^{glob}$-continuum space obtained using CORSIKA simulations

CORSIKA (QGSJET) simulations have been done for proton and iron primaries; 3 fixed energies (10^{15} eV, $3.16{\cdot}10^{15}$ eV, 10^{16} eV) and 4 zenith angles (5°, 15°, 25°, 35°) have been considered (approx. 200 showers for each case). For all cases above, adopting the detector resolution of 1.5 ns for muon arrival times, $\Delta\tau_\mu^{glob}$-distributions have been calculated for 15 radius bins (0÷10 m, 10÷20 m,..., 140÷150 m), considering all muons $E_{thres} = 2.4$ GeV, cumulating all (200) showers.
Corresponding to a multiplicity n (between 3 and 456), a number n of individual arrival times are randomly selected from the $\Delta\tau_\mu^{glob}$-distribution coresponding to a certain radius bin (according to the p.f. represented by the distribution) and $\Delta\tau_1^{glob}$ has been calculated. Repeating the procedure approx. 9000 times (for good statistics), $\Delta\tau_1^{glob}$-distributions have been estimated for

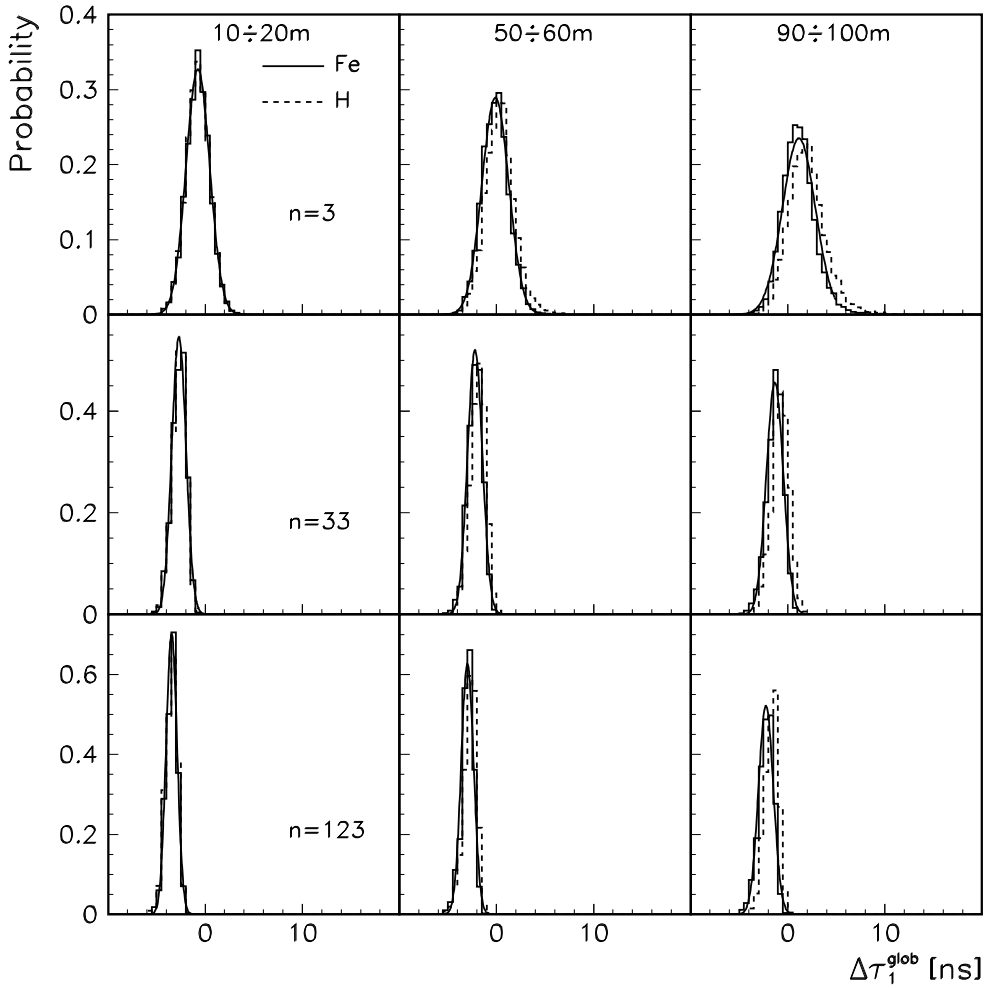

Fig. 5.4: $\Delta\tau_1^{glob}$-distributions for proton and iron primaries ($\theta = 15°$ and $E_0 = 10^{15}$ eV) for 3 radius bins and 3 muon multiplicities.

the cases

$$\{\text{H, Fe}\}\times$$
$$\{10^{15}\text{ eV},\ 3.16\cdot 10^{15}\text{ eV},\ 10^{16}\text{ eV}\}\times$$
$$\{5°,\ 15°,\ 25°,\ 35°\}\times$$
$$\{0\div 10\text{ m},\ 10\div 20\text{ m},\ldots,\ 140\div 150\text{ m}\}\times$$
$$\{3,\ 4,\ldots,\ 456\},$$

see Fig. 5.4. The existence of *negative measured times* is due to muons registered before the electromagnetic front of the shower core. This is another time resolution effect. It is shown that $\Delta\tau_1^{glob}$-distributions can be very well approximated by gaussian distributions; e.g.: gaussians defined by the mean values ($\langle\Delta\tau_1^{glob}\rangle$) and standard deviations (σ_1) of the iron distributions are superimposed on the Fig. 5.4. In Fig. 5.5 the multiplicity dependence of the

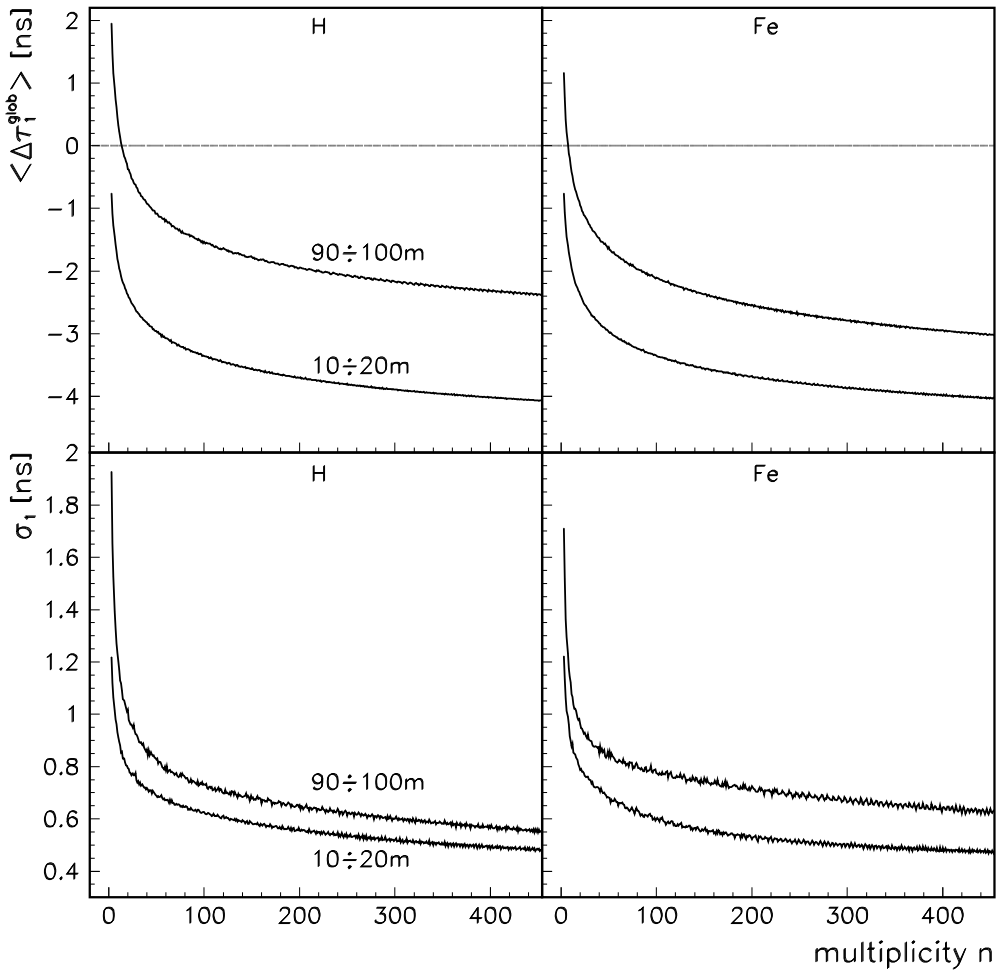

Fig. 5.5: Multiplicity dependence of $\langle\Delta\tau_1^{glob}\rangle$ and σ_1 for proton and iron primaries ($\theta = 15^\circ$ and $E_0 = 10^{15}$ eV), in two radial bins.

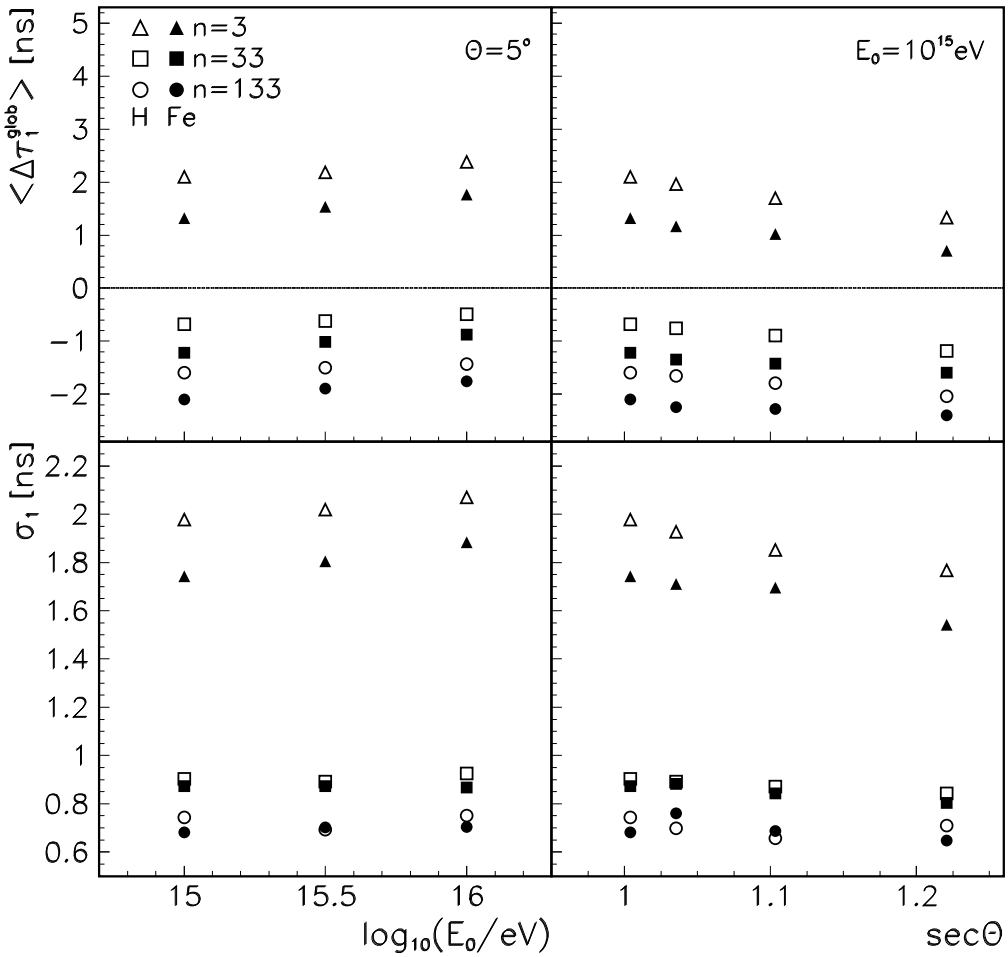

Fig. 5.6: Dependence with $log_{10}E_0$ and $sec\theta$ of $\langle\Delta\tau_1^{glob}\rangle$ and σ_1 for proton and iron primaries, for 3 multiplicities; a 90÷100 m radius range has been considered.

mean values and standard deviations of $\Delta\tau_1^{glob}$ - distributions is represented. Fig. 5.6 presents the dependence of $\langle\Delta\tau_1^{glob}\rangle$ and σ_1 on the primary energy (E_0) and zenith angle (θ) of the shower.

For a certain multiplicity, primary type and radius bin, a continuum space over $sec\theta$ and $log_{10}E_0$ has been built for $\langle\Delta\tau_1^{glob}\rangle$ and σ_1, extrapolating linearly between neighbouring points represented (as example) in Fig. 5.6.

5.4.2 Transformation of measured local times into global times

Zenith angle θ, muon multiplicity n (≥ 3) in the Central Detector and N_μ^{tr} are accesible for a certain shower; also the values for local times:

$$\Delta\tau_{1i}^{loc} = \Delta\tau_i^{glob} - \Delta\tau_1^{glob}, \;\; i \in \{2, n\}$$

The radial bin is given by the position of the centre of the Central Detector with respect to the shower core (in shower coordinates). N_μ^{tr} can be transformed in E_0 according to the relations:

$$log_{10}E_0(GeV) = 2.729 + 0.9549 \cdot log_{10}N_\mu^{tr}, \text{ if proton}$$
$$log_{10}E_0(GeV) = 2.294 + 1.046 \cdot log_{10}N_\mu^{tr}, \text{ if iron}$$

Assuming the shower was produced by a certain primary (H or Fe), corresponding $\langle\Delta\tau_1^{glob}\rangle$ and σ_1 can be estimated from the continuum space defined in Sec. 5.4.1.
For the given shower, local times have been transformed in global times according to relations:

$$\Delta\tau_i^{glob} = \langle\Delta\tau_1^{glob}\rangle + \Delta\tau_{1i}^{loc}, \;\; i \in \{2, n\} \tag{5.5}$$

$\Delta\tau_1^{glob}$ has been formally generated (randomly) from a gaussian distribution with mean value $\langle\Delta\tau_1^{glob}\rangle$ and standard deviation σ_1. In relation 5.5 appears $\langle\Delta\tau_1^{glob}\rangle$ and not the truely "measured" time of the foremost muon; $\Delta\tau_i^{glob}$ will be spread from their truely "measured" values because of this reason. But this effect is compensated in single muon arrival time distributions by "filling" them with several showers with the same multiplicity. A difficulty of the transformation of local times into global times appears because from the begining a shower has to be considered as produced by a certain primary. Fig. 5.7 shows that if a certain mass composition is assumed (H:Fe=a:b), the following relation can be written:

$$(aH + bFe) \uparrow (aH + bFe) \cong aH \uparrow H + bFe \uparrow Fe \tag{5.6}$$

$(a_1H + b_1Fe) \uparrow (a_2H + b_2Fe)$ means that local times for a composition $(a_2H + b_2Fe)$ are transformed in global times considering $(\langle\Delta\tau_1^{glob}\rangle, \sigma_1)$ coming with probabilities a_1 and b_1 from proton and iron continuum spaces, respectively.

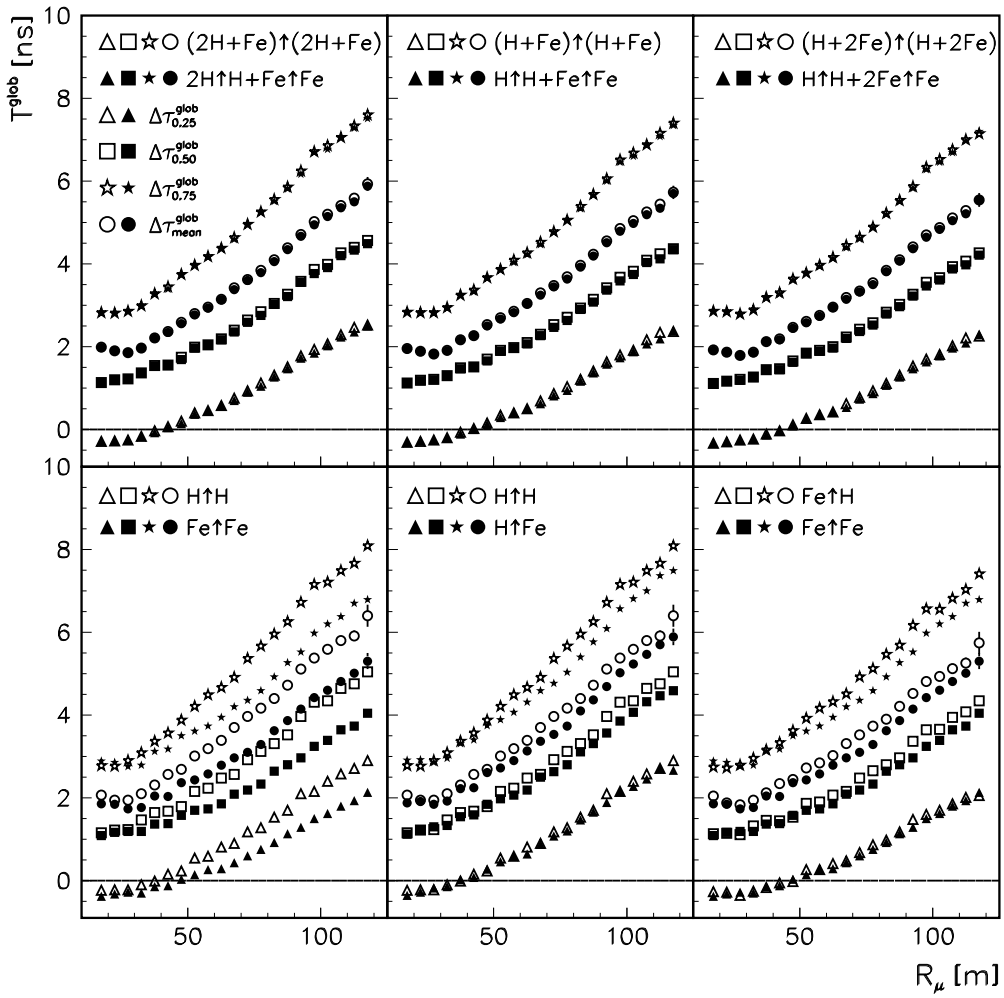

Fig. 5.7: Simulated shower profiles assuming 3 mass compositions; a comparision between $H \uparrow H$, $Fe \uparrow Fe$, $H \uparrow Fe$, $Fe \uparrow H$ is also presented; $3.6 < lgN_\mu^{tr} \leq 4.8$, $5^\circ < \theta \leq 30^\circ$.

The explanation of the relation 5.6 is quite simple. From Fig. 5.7 it is clear that:

$$H \uparrow H \sim H \uparrow Fe \text{ and } Fe \uparrow H \sim Fe \uparrow Fe \tag{5.7}$$

From equation 5.7 it results:
$(aH + bFe) \uparrow (aH + bFe) \equiv a^2 H \uparrow H + abH \uparrow Fe + abFe \uparrow H + b^2 Fe \uparrow Fe$

$\simeq a(a+b)H \uparrow H + b(a+b)Fe \uparrow Fe = aH \uparrow H + bFe \uparrow Fe,$
because $a + b = 1$ (probability normalisation).

6. COMPARISON WITH THEORETICAL PREDICTIONS BASED ON A PARAMETRIC ANALYSIS

Global muon arrival times, obtained from local times by applying procedure described in Section 5.4, have been considered to compare experimental data with theoretical predictions included in the complete simulations presented in Sec 5.2. A mass composition $H : Fe = 2 : 1$ has been adopted for comparison between experimental data and simulations (ref. [54] proposed $H : O : Fe = 4 : 1 : 2$).

6.1 Time distributions

Each individual muon has its own distance to the shower core (in shower coordinates). In the following analysis 24 radius bins (0÷5 m, 5÷10 m,..., 115÷120 m) have been considered for individual muons. The distance between the centre of the Central Detector and the shower core has been considered between 0÷110 m. Global time distributions of individual muons (cumulated over many showers) have been built for all 24 radius bins. For each distribution a mean value $\Delta\tau^{glob}_{mean}$, a standard deviation σ (see Appendix B) and quantiles $\Delta\tau^{glob}_{0.25}$, $\Delta\tau^{glob}_{0.50}$, $\Delta\tau^{glob}_{0.75}$ have been calculated. Figure 6.1 compares the experimental and simulated muon arrival time distributions for 3 radial bins. It's clearly seen that distributions become broader and shifted to larger mean values with increasing distance from the shower centre. At a first look, there is a good agreement between experiment and simulation both on averaged values and on fluctuations. Just empirically motivated (and also by tradition [21, 59]), distributions from Fig. 6.1 are parametrised

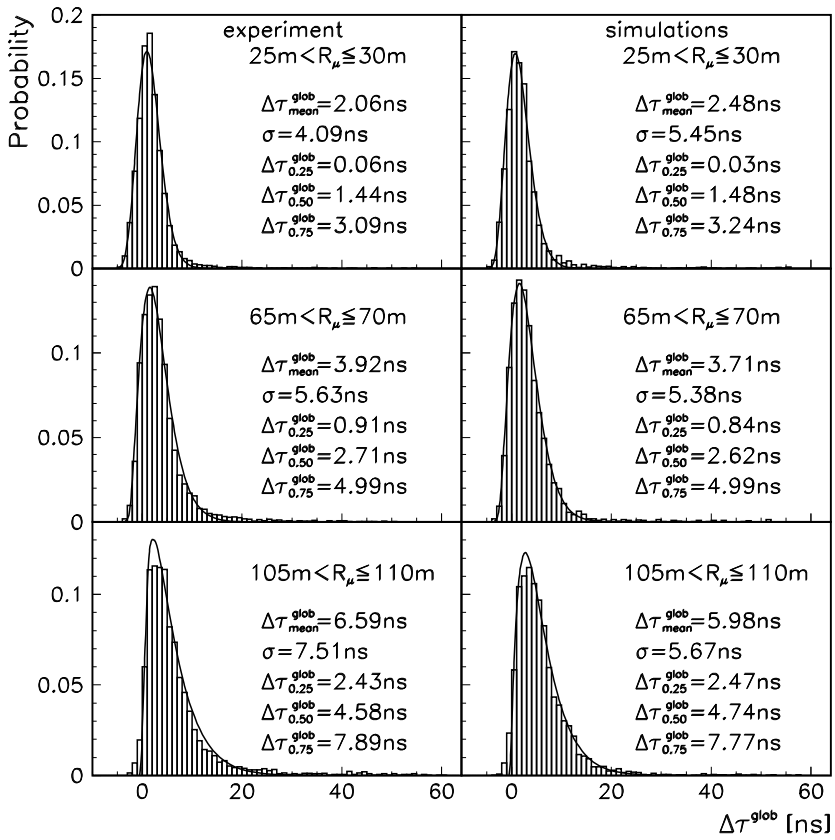

Fig. 6.1: Single muon distributions (fitted with Γ-function) for the particular samples with $4.25 < log_{10}N_\mu^{tr} \leq 4.45$ for the angular range $5° < \theta \leq 30°$ and for three radial bins.

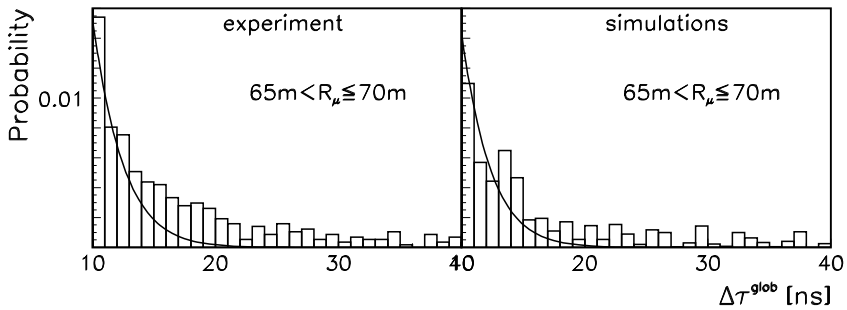

Fig. 6.2: Tails of the experimental and simulated single muon distributions fitted with the Γ-form for the sample with $4.25 < log_{10}N_\mu^{tr} \leq 4.45$, $5° < \theta \leq 30°$, 65 m $< R_\mu \leq$ 70 m.

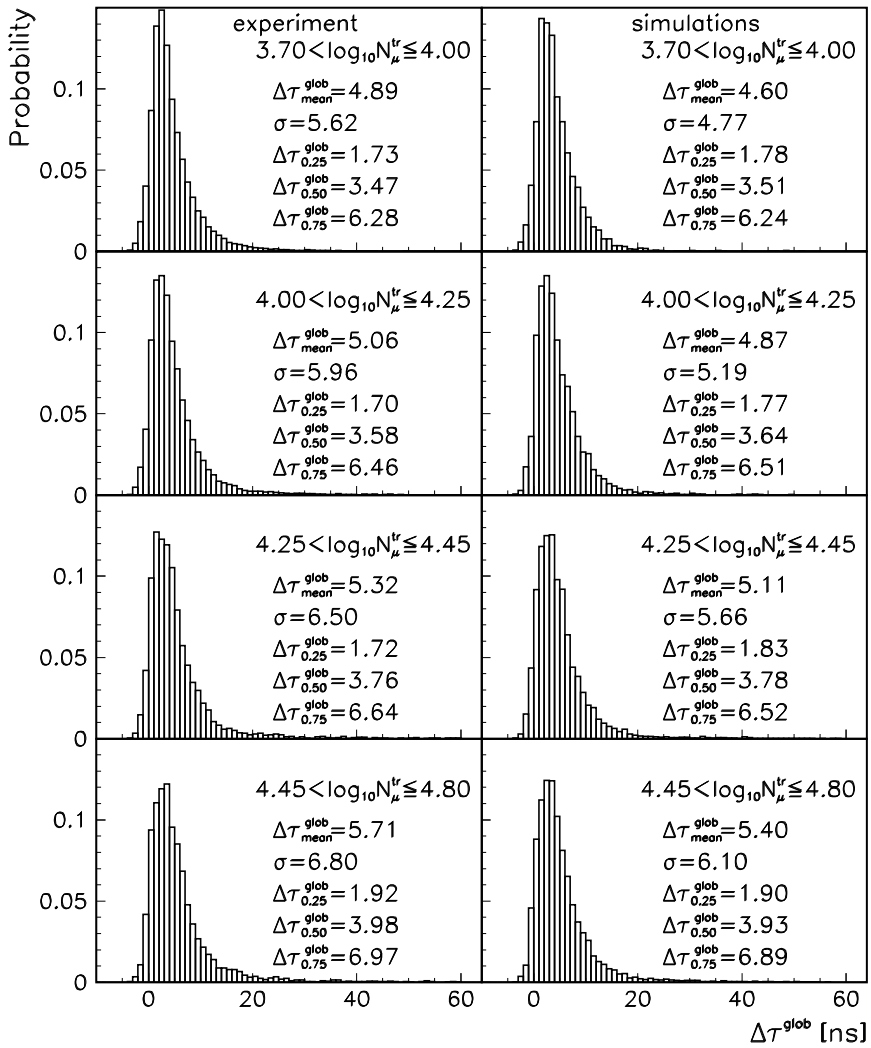

Fig. 6.3: Single muon distributions for different $log_{10}N_\mu^{tr}$ ranges displayed for the angular range $5° < \theta \leq 30°$ and the radial range 90 m $< R_\mu \leq$ 95 m.

by Γ-distributions:

$$\Gamma(T) \;=\; a\,T^b exp(-c\,T) \qquad\qquad (T = \Delta\tau_\alpha)$$

with a mean value $\langle T \rangle = (1+b)/c$ and the standard deviation $\sigma_\Gamma = (1+$

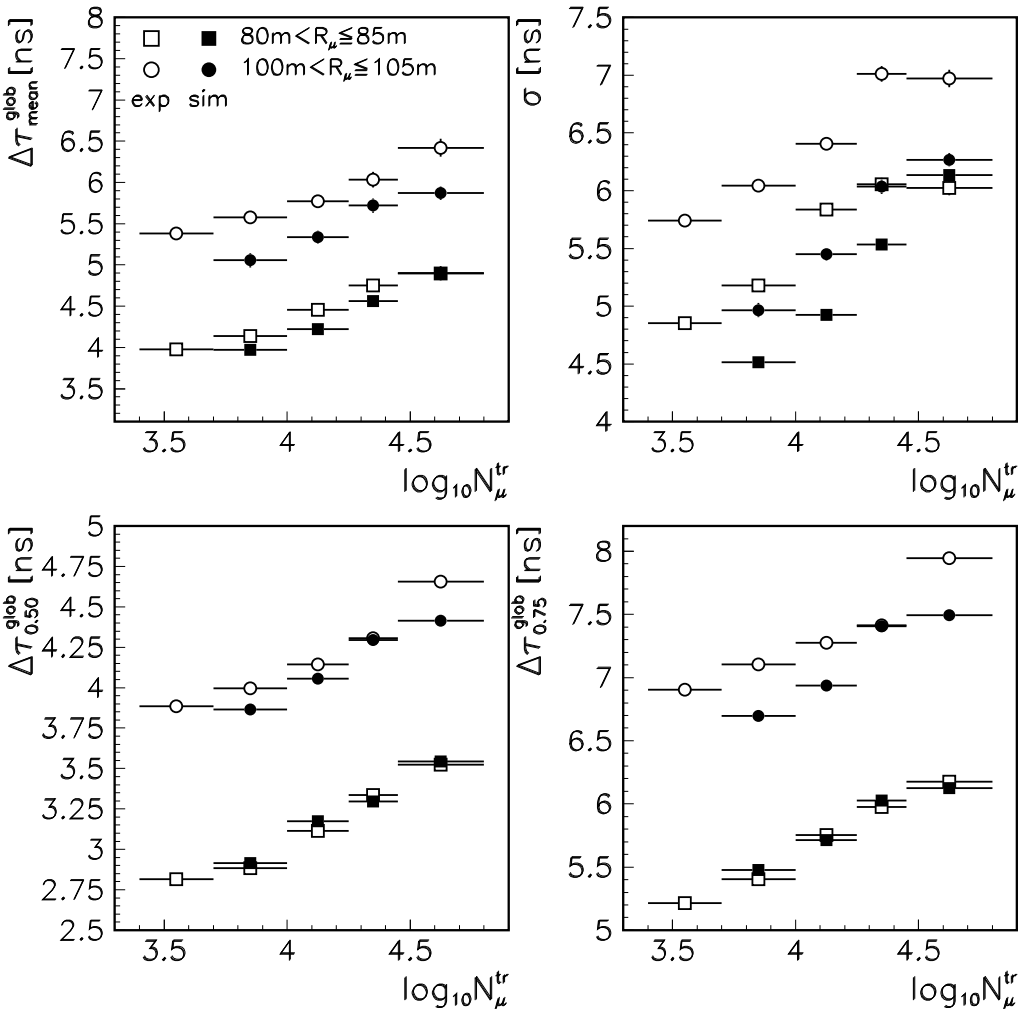

Fig. 6.4: Energy dependence of the mean value, standard deviation, median and third quartile of the single distributions observed at two different ranges of the distance from the shower core ($5° < \theta \leq 30°$).

$b)^{1/2}/c$. The shape of the Γ-form, with a fast increase and a longer decreasing slope, reflects just the gross longitudinal development of the muon component. Only the tails of the distributions are less well described by the Γ-form (Fig. 6.2). A parametrisation by a logarithmic Gauss [57] does sufficiently

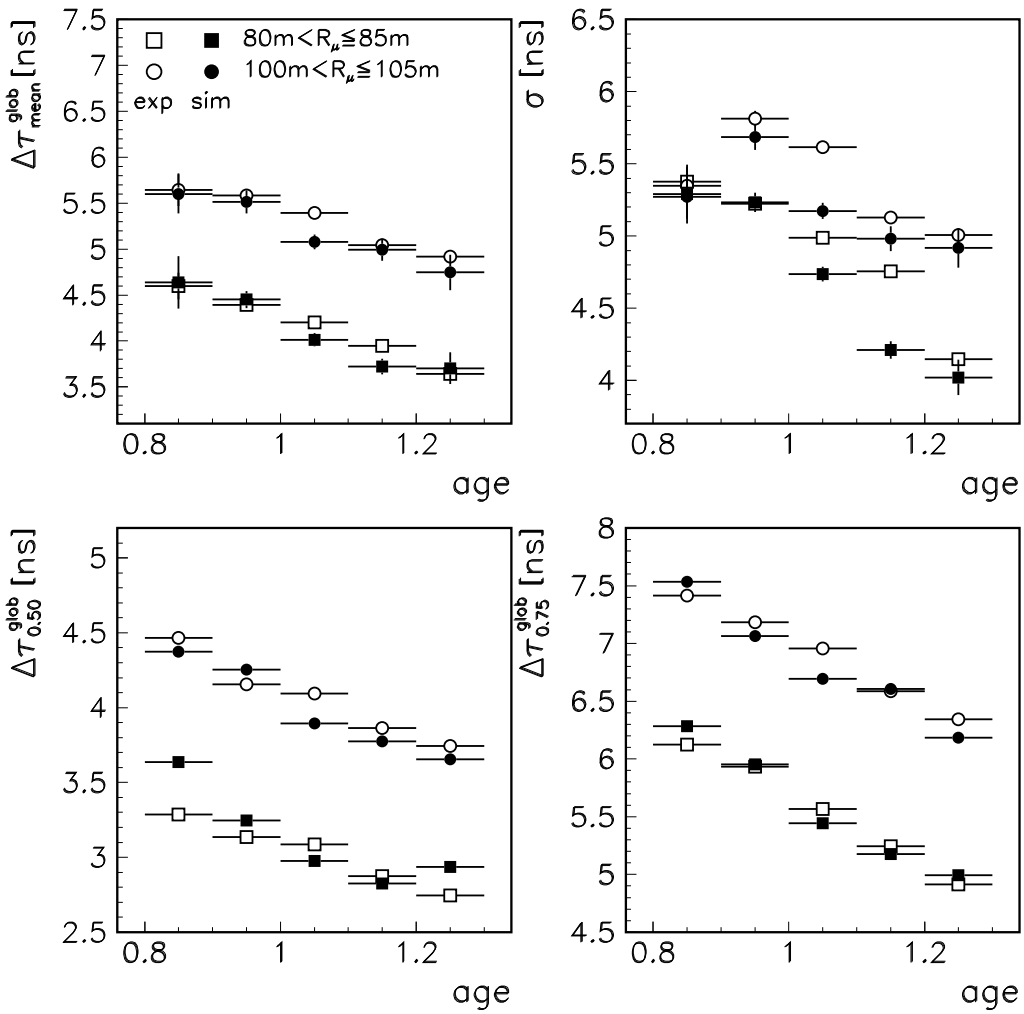

Fig. 6.5: Age dependence of the mean value, standard deviation, median and third quartile of the single distributions observed at two different ranges of the distance from the shower core ($5° < \theta \leq 30°$ and $3.6 < log_{10} N_\mu^{tr} \leq 4.8$).

well reproduce such tails as pointed out by Battistoni et al. [58]. A part of the experimental "delayed" tail from Fig. 6.2 may be accounted to uncorrelated particles triggering the zero-time too early. The contribution arising

from uncorrelated muons is estimated to be less than 20% in the tail [21], completely negligible for the total distribution. Presenting experimental and simulated muon arrival time distributions in four N_μ^{tr} ranges (indicating primary energies), Figure 6.3 exibits increasing averaged values and fluctuations for higher primary energies. Figure 6.4 shows the N_μ^{tr} dependence of averaged values and fluctuations. From both Figures 6.3, 6.4 it appears a systematic tendency that the distributions of the simulated data underestimate the thickness of the muon disk. The age dependencies of the averaged values and fluctuations of the single time distributions are shown in Fig. 6.5 for two radius ranges. The decreasing values may be qualitatively understood as corelation between age and the depth of the EAS maximum. Higher values for age means "older" showers, i.e. showers which start earlier their longitudinal development; muons come from higher altitude and, because of this, they have smaller arrival times. Despite the underestimation of the thickness of the muon disk in simulations, there is a good agreement between measured and simulated dependencies of averaged time values with N_μ^{tr} and age.

6.2 Time profiles

The variation of different time quantities characterising single muon arrival

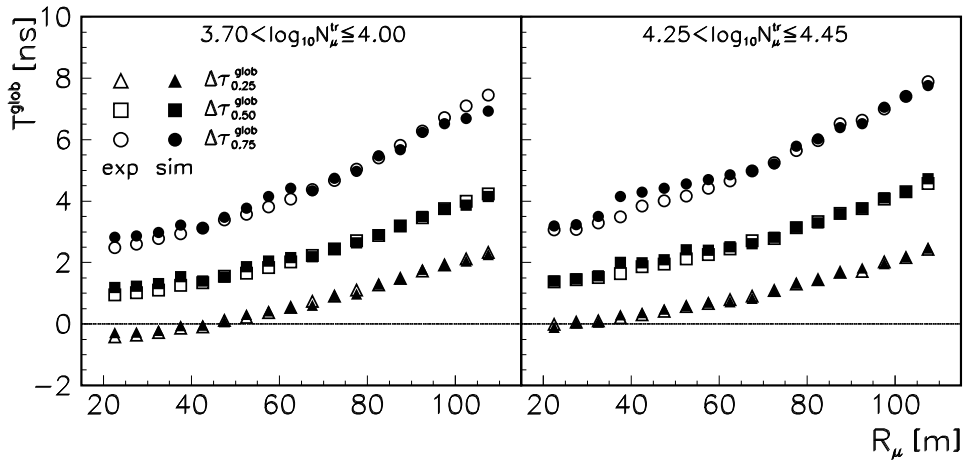

Fig. 6.6: Experimental and simulated time profiles for two different N_μ^{tr} ranges (corresponding to energy ranges of the primary cosmic ray spectrum before and after the "knee") and for $5° < \theta \leq 30°$.

time distributions ($\Delta\tau^{glob}_{mean}$, σ, $\Delta\tau^{glob}_{0.25}$, $\Delta\tau^{glob}_{0.50}$, $\Delta\tau^{glob}_{0.75}$) with the distance R_μ from the EAS core represents the time structure of the EAS muon disk. It is dependent on the primary energy E_0, the nature (mass A) of the primary particle, the angle of the shower incidence and from observation conditions (energy threshold, time resolution). Profiles of the time distributions for different N^{tr}_μ and angular ranges are presented in Figs. 6.6 and 6.7. There is a good agreement between measured and simulated data. Simulated data are not presented in Fig. 6.7 just for the clarity of the figure. As Fig. 6.7 shows, there is a systematic variation of the profile with the EAS angle of incidence. The averaged values and fluctuations decrease with increasing the zenithal angle. The considered zenithal angle ranges in Fig. 6.7 ($0° \div 24°$, $24° \div 33°$,

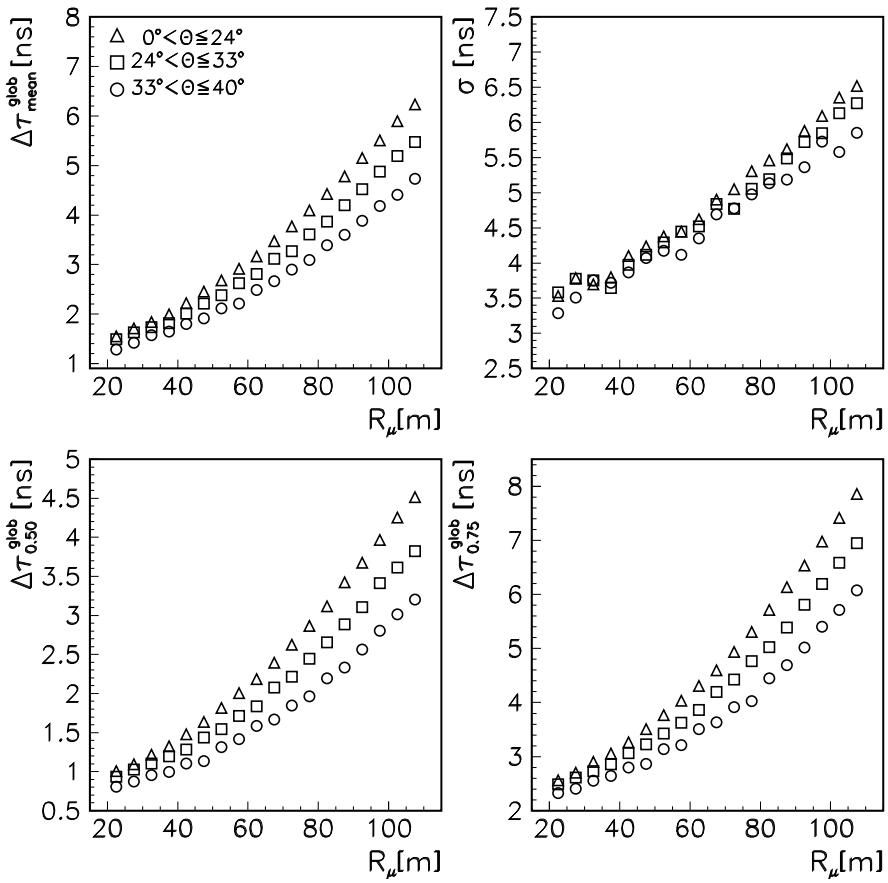

Fig. 6.7: Experimental time profiles for different angular ranges of EAS incidence for $3.6 < log_{10}N^{tr}_\mu \leq 4.8$.

$33° \div 40°$) corresponds to rather equal $sec\theta$-bins (the equivalent atmospheric thickness at the observation level is proportional with $sec\theta$). The statistical uncertainty in the mean values and in the standard deviations are given by $\sigma/\sqrt{N}$ and $\sigma/\sqrt{2(N-1)}$, respectively. In case of experimental data N represents the number of events while in simulation data N represents the number of equivalent events (Appendix B). In the shown figures these errors are smaller than the size of the markers. The systematic errors are mainly coming from multiplicity effects due to the finite time resolution (one effect is the presence of negative times) and from the assumption made on primary mass composition. In the second order the systematic uncertainity is introduced by the procedure to transform local times into global times and the CORSIKA assumption in building the $\Delta\tau_1^{glob}$ continuum space. These systematic errors affect in a consistent way both measurements and simulations.

6.3 Muon production heights

Muon production loci, expressed by the atmospheric thickness above, dis-

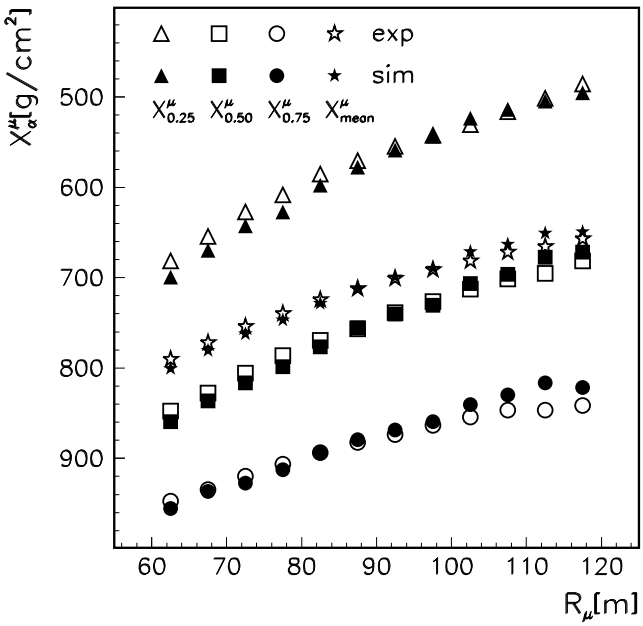

Fig. 6.8: Experimental and simulated radial dependence of different "fractions" of the muon longitudinal development; $5° < \theta \leq 30°$ and $3.6 < log_{10}N_{\mu}^{tr} \leq 4.8$).

play the longitudinal development of the shower. Using simple triangulation, production loci (in g/cm^2, starting from the top of the atmosphere) of single muons have been estimated from their global arrival times (obtained with the procedure described in Sec. 5.4). The barometric profile of the US standard atmosphere with five layers has been used. Negative global times (resolution effect) have been simply ignored. There are considerable uncertainties

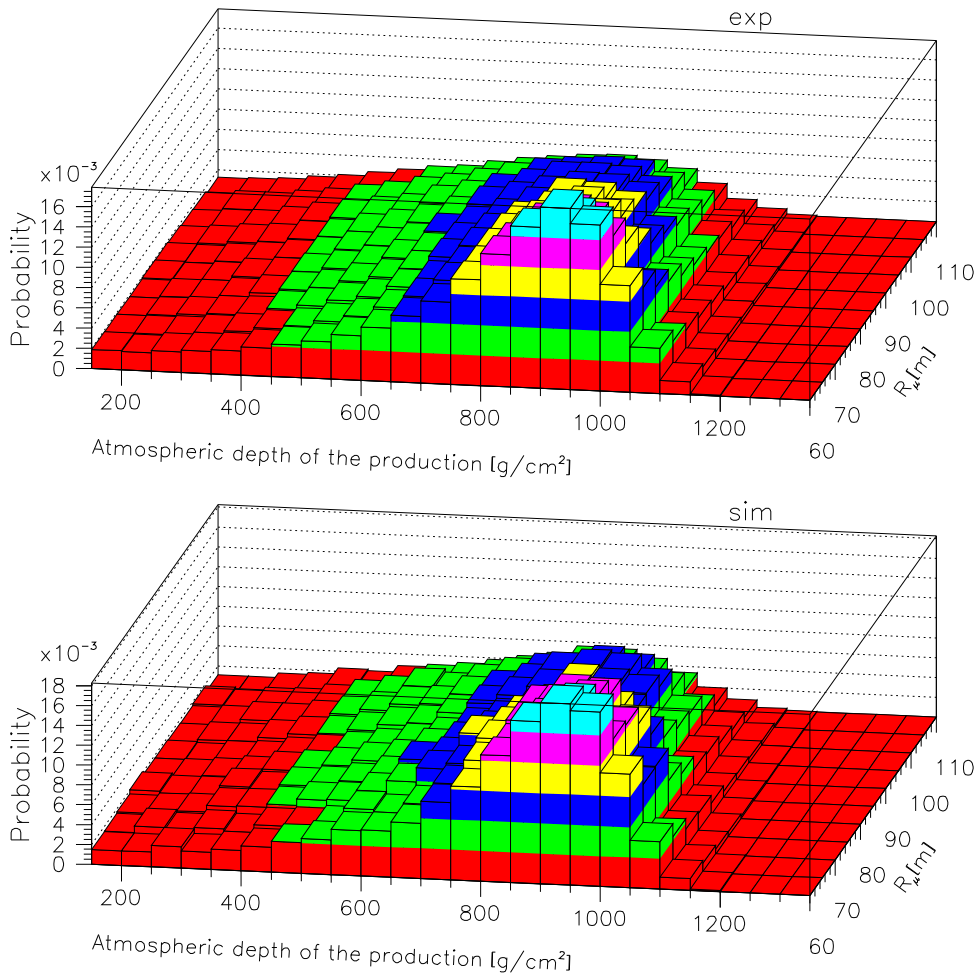

Fig. 6.9: Profiles of the muon production loci for muons detected in a 60÷110 m distance from the EAS axis for $5° < \theta \leq 30°$ and $3.6 < log_{10} N_\mu^{tr} \leq 4.8$.

inherent to the procedure transforming the arrival time distributions to longitudinal profiles, and uncertainties due to the finite time resolution of the detector. These uncertainties affect the data and simulations in the same systematic way. In Fig. 6.8 the variation of the production height distributions of the muons is displayed, as observed at the distance R_μ from the shower core. $X^\mu_{0.25}$, $X^\mu_{0.50}$,... mean the atmospheric depths when 25%, 50% etc. of the muons observed at R_μ are produced; X^μ_{mean} represents the mean atmospheric depth where the muons observed at R_μ are produced. The results, with good agreement of data and simulations, exhibit a lateral variation of the detected muon profile (larger R_μ emphasise the beginning of the EAS development) and they indicate the interrelation of arrival time and lateral density distribution. In other words, the arrival time distributions do not map the total N_μ-profile, only that part arriving at R_μ. The feature is underlined in Fig. 6.9, showing the average profiles of the muon component (2.4 GeV energy threshold) varying in the range $R_\mu = 60 \div 100$ m for a certain N^{tr}_μ range.

7. NONPARAMETRIC MULTIVARIATE ANALYSES OF MUON ARRIVAL TIME DISTRIBUTIONS

The inference of the nature and the properties of the primary cosmic particles from EAS observations requires the comparison with the distributions of EAS observables generated by Monte Carlo simulations, after being folded by the response of the detectors (see Fig. 4.6). The comparison of the experimentally observed EAS parameters with the pattern of such pseudo-experimental data can be principally performed in two different ways:

- By use of adequate parameterisations of the EAS parameter, describing the average behaviour and neglecting the correlations between the parameters.
- Alternatively, taking into account the nonparametric character of the observed parameter distributions and their correlations the comparisons can be made event-per-event, invoking advanced statistical decision methods. In this case the fluctuations are taken into account, and uncertainties of the classifications can be specified.

In this chapter the attempt is made to analyse the measured time structure of the EAS muon component with nonparametric techniques, in particular in view of the role of muon arrival time distribution for the mass discrimination of the primaries (see also [19]). It is obvious that the procedure is unavoidably model-dependent.
It has to be stressed that only local muon arrival times will be used for this multivariate analysis, without the procedure to correct the multiplicity effects. The multiplicity correction procedure and also the transformation of local times into global times need "a-priori" assumptions on the primary mass compositions, being inadequated for an analysis concerning primary mass discrimination.

7.1 Basic principles

Multivariate analysis techniques are used to study the correlations between physical variables by comparing experimental data with theoretical models and for grouping experimental events in different classes [60, 61, 62].
When the Likelihood function cannot be written explicitely like strictly in the case of EAS observations, nonparametric techniques are invoked, avoiding the constraint by a specific analytical parametrisation. Usually, the population distribution is considered to be continuous.
For a short sketch of the basic procedures we introduce first some notations:

- A_i ($i \in \{1, m\}$) represent classes of events. The different classes are defined by the different primary nuclei (H, O, Fe etc.) inducing EAS; $A \stackrel{def}{=} \bigcup_{j=1}^{m} A_j$ notes all primary nuclei classes. The classes are disjunctives and normalised by:

$$P(A) = 1 \tag{7.1}$$

- $x \equiv (x_1, x_2, ..., x_n)^T$ is the random vector of observables of a phenomenon (EAS observables in our case) initiated by an event X (primary nucleus) from one of the classes A_i;

- from Monte Carlo simulations an "a-priori" probability $P(x \mid A_i)$ (to observe x if $X \in A_i$) can be calculated;

- an "a-posteriori" probability $P(A_i \mid x)$ (to have $X \in A_i$ if x is observed) can be calculated from "a-priori" probabilities by using the Bayes theorem.

7.2 Nonparametric estimation of the probability densities

The first step of the analysis procedure is to derive the probability density $P(x \mid A_i)$ distributions from the Monte Carlo calculations. Therefore various procedures have been proposed. The Parzen [63, 64] and K nearest neighbours (KNN) [65, 66] methods are indicated as examples for the construction of the conditional densities. In the Parzen procedure every point of the training sample (TS), u_j, is substituted by a bell-like function (e.g. gaussian), and the density in arbitrary point x of the feature space is obtained as

a superposition of numerous "kernels" centered about each TS point

$$P(x \mid A_i) = \frac{1}{\left(\sigma\sqrt{2\pi}\right)^{n+1}\sqrt{\mid \Sigma_i \mid}} \sum_{j=1}^{M_i} w_j e^{-\frac{r_j^2}{2\sigma^2}}, \;\; i \in \{1, m\} \tag{7.2}$$

where:
- Σ_i is the sampling covariance matrix of the class to which events u_j ($j \in \{1, M_i\}$) belong;
- σ is the kernel width;
- n is the feature space dimensionality;
- M_i is the number of events in the i-th training sample;
- w_j is the weight of event u_j; $\sum_{j=1}^{M_i} w_j = 1$
- r_j is the distance from experimental event x to the j-th event of the TS in the Mahalonobis metric [67]:

$$r_j^2 = (x - u_j)\Sigma_i^{-1}(x - u_j) \tag{7.3}$$

The distances calculated in the Mahalonobis metric are scale invariant; no transformation of initial data is necessarily.
The KNN estimation takes the form:

$$P(x \mid A_i) = \frac{k-1}{M_i V_k(x)} \tag{7.4}$$

where $V_k(x)$ is the volume of a n-dimensional hypersphere containing the k-th nearest neighbour of the experimental event x:

$$V_k(x) = V_n \mid \Sigma_i \mid^{1/2} r_k^n, \;\; V_n = \frac{\pi^{n/2}}{\Gamma(n/2+1)} \tag{7.5}$$

r_k is the distance to the k-th nearest neighbour of x in the Mahalonobis metric. Only the Parzen procedure has been used next.

7.3 The Bayesian approach

Just for simplicity, only 3 classes A_i will be considered furtheron, corresponding to 3 primaries (H, O, Fe) inducing Extensive Air Showers. $x \equiv (x_1, x_2, ..., x_n)^T$ will represent some EAS observables. The nonparametric

Bayesian decision rule associates a particular observed event x to a definite class of events (H, O, Fe) and takes the form:

$$max\{P(H \mid x), P(O \mid x), P(Fe \mid x)\} \xrightarrow{decision} \begin{matrix} H \\ O \\ Fe \end{matrix} \tag{7.6}$$

Bayes theorem C.1 (see Appendix C) is invoked for an estimate of the a-posteriori probabilities from a-priori probabilities (which are known from simulations):

$$\begin{aligned} P(H \mid x) &= P(x \mid H)P(H)/P(x) \\ P(O \mid x) &= P(x \mid O)P(O)/P(x) \\ P(Fe \mid x) &= P(x \mid Fe)P(Fe)/P(x) \end{aligned} \tag{7.7}$$

where $P(x) = P(x \mid H)P(H) + P(x \mid O)P(O) + P(x \mid Fe)P(Fe)$

The Bayesian decision rule, like all statistical methods, include a quality test as a necessary element. The measure of quality is the error probability depending on the degree of overlapping of multivariate distributions (Bayes decision rule provide minimal error as compared to any other decision rule using the same features). The method "one-leave-out-for-a-time" is used for an estimate of the Bayes error [68]. In this method, each element is subsequently removed from the MC sample (probability densities are calculated without it), it is classified and then returned into the training sample. Thus, using the definition

$$\epsilon(x) = \begin{cases} 0, & \text{for correct classification} \\ 1, & \text{otherwise} \end{cases} \tag{7.8}$$

the estimated error R^e is

$$R^e = \frac{1}{M_i} \sum_{j=1}^{M_i} \epsilon(u_j) \tag{7.9}$$

Using the "one-leave-out-for-a-time" method, probabilities $P_{A_i \to A_j}$ (i.e. the probability of classifying events of the i-th class as belonging to the j-th

class) can be estimated. The terminology "misclassification" probability is used for $P_{A_i \to A_j}$ when $i \neq j$ while $P_{A_i \to A_i}$ represents the "true" classification probabilities. Reconstructing (by applying nonparametric Bayesian decision rule) the mass composition of a control sample with $N = n_H + n_O + n_{Fe}$ events, the number of events n_H, n_O, n_{Fe} corresponding to each class (H, O, Fe) gets altered to n'_H, n'_O, n'_{Fe} given by:

$$\begin{aligned} n'_H &= P_{H \to H} n_H + P_{O \to H} n_O + P_{Fe \to H} n_{Fe} \\ n'_O &= P_{H \to O} n_H + P_{O \to O} n_O + P_{Fe \to O} n_{Fe} \\ n'_{Fe} &= P_{H \to Fe} n_H + P_{O \to Fe} n_O + P_{Fe \to Fe} n_{Fe} \end{aligned} \tag{7.10}$$

The above system of linear equations can be inverted in order to determine the true values n_H, n_O, n_{Fe} defining the primary mass composition. The statistical errors affecting the numbers n_H, n_O, n_{Fe} are estimated using the bootstrap method [69] which consists in replication of the initial sample many times by means of random sampling with replacement.
All used procedures are included in the program ANI (**A**nalysis and **N**onparametric **I**nference) [70] especially developed for high energy physics and astrophysics experiments.

7.4 Mass discrimination

The complete simulations prepared in Sec. 5.2 and including the realistic detector response have been used to obtain training samples for the Bayesian analysis. All three primaries have been considered in the analysis: H, O and Fe. The simulated events have been weighted according to eq. 5.2. Eq. 5.3 has been used for the spectral index around the "knee". The following EAS observables are considered in the analysis:

- the truncated number of muons N_μ^{tr} (the energy estimator);
- the shower size (N_e);
- the shower age (s);
- the muon local time quantiles (Q_α);

- the multiplicity n of muons (above 2.4 GeV) detected in the Central Detector;

- the muon local time quantiles divided by muon density: $q_\alpha = Q_\alpha/\rho_\mu$. ρ_μ represents the multiplicity n of muons divided by the area of he Central Detector.

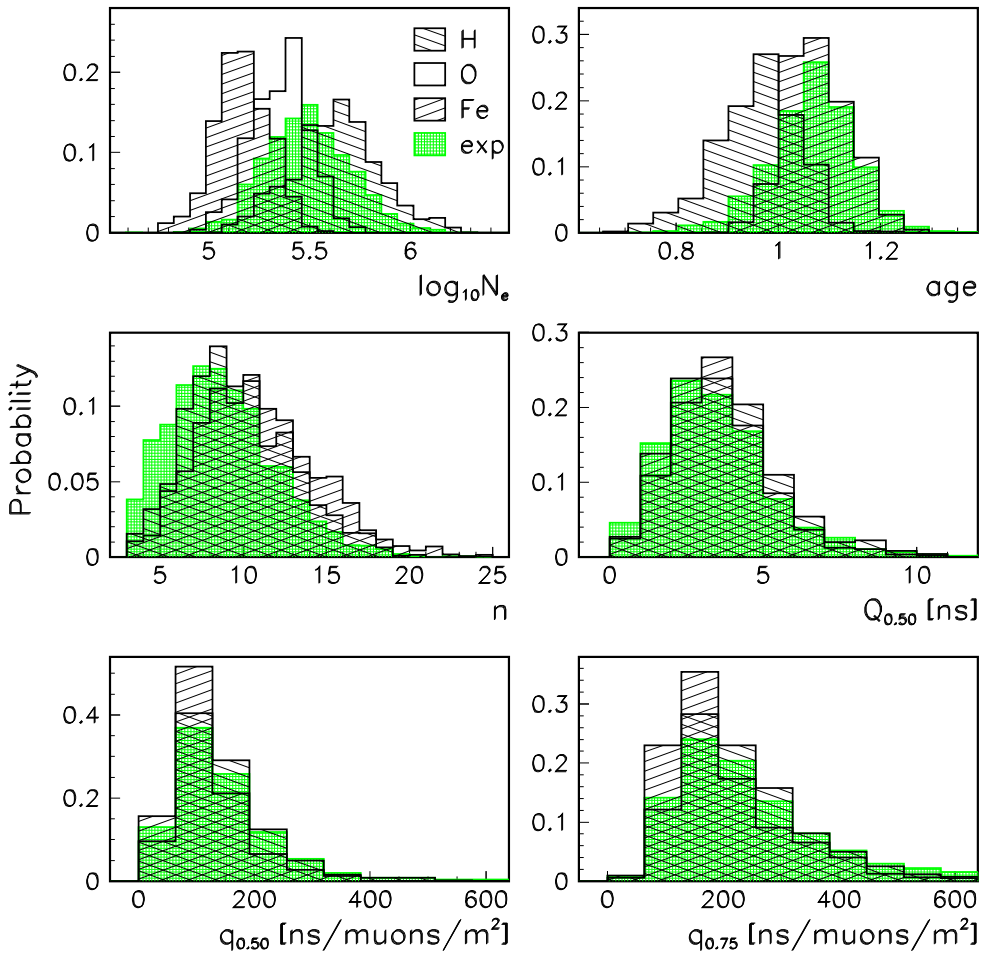

Fig. 7.1: Comparison between simulations and experimental data for six shower observables in a particular N_μ^{tr} ($4.05 < log_{10}N_\mu^{tr} \leq 4.28$), radius (80 m $< R_\mu \leq$ 90 m) and theta ($0° < \theta \leq 24°$) ranges.

A comparison between simulations and measurements for various shower observables, in a certain $N_\mu^{tr} \times R_\mu \times \theta$ bin, is shown in Fig. 7.1. Shower size, shower age, muon multiplicity, median muon arrival time, median and third quartile divided by muon density are displayed. The oxygen distribution is plotted only in case of the shower size for clarity of the figure. Such distributions have been used, in different combinations, as input for the classification

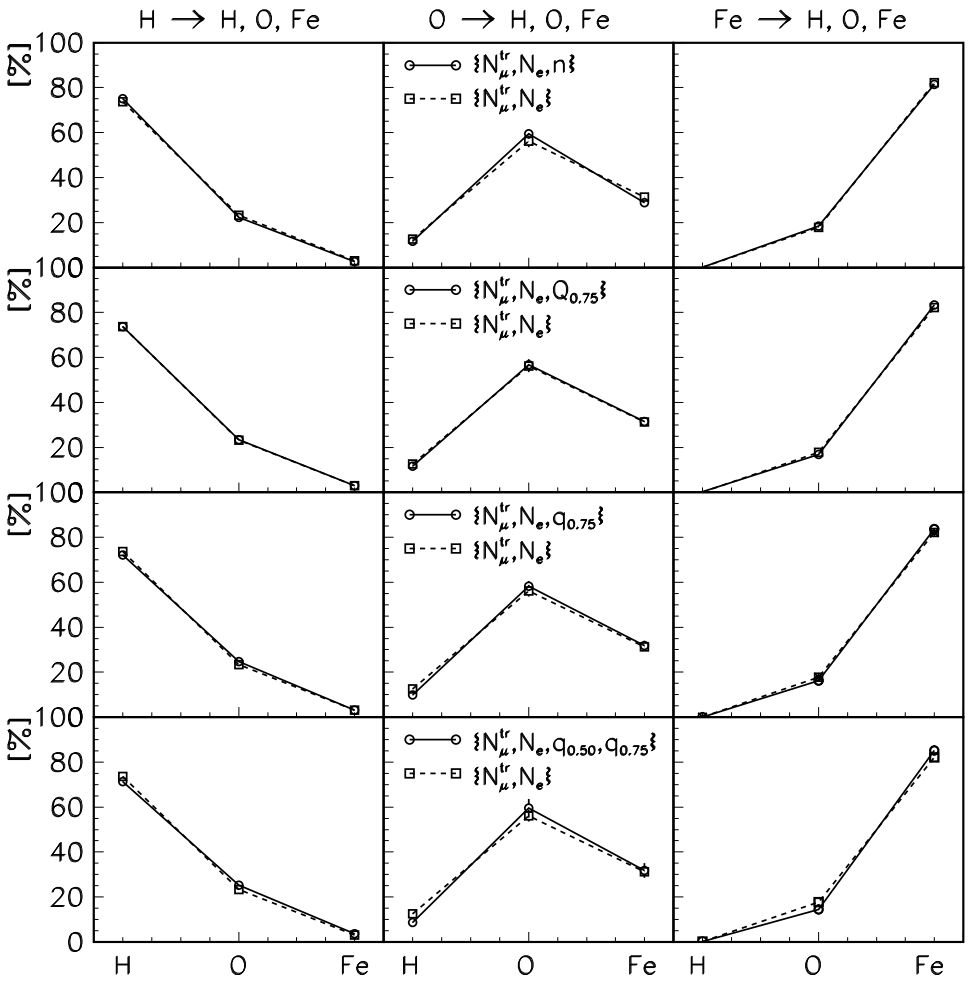

Fig. 7.2: Probabilities of classification and misclassification using Bayes procedure in 3 classes (H, O, Fe) and 5 combinations of observables; $3.83 < log_{10} N_\mu^{tr} \leq 4.05$, 80 m $< R_\mu \leq$ 90 m, $0° < \theta \leq 24°$.

procedure.
Figs. 7.2 and 7.3 display the probabilities of classification and misclassification (using Bayes procedure) in different classes (H, O, Fe) and for two energy ranges (7.2 before the knee, 7.3 around the knee). As example, an Extensive Air Shower initiated by a proton primary can be correctly classified with a

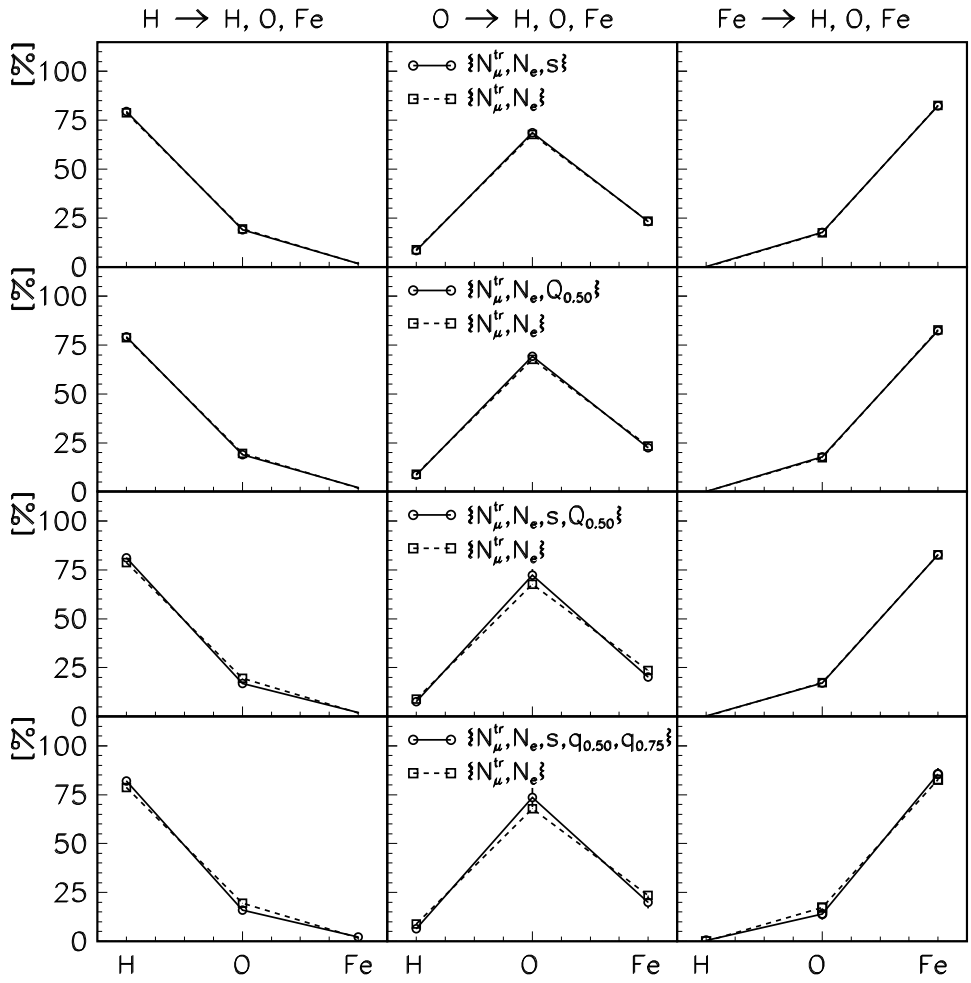

Fig. 7.3: Probabilities of classification and misclassification using Bayes procedure for 3 different classes (H, O, Fe) and 4 combinations of observables (including age); $4.05 < log_{10}N_\mu^{tr} \leq 4.28$, 65 m $< R_\mu \leq$ 80 m, $0° < \theta \leq 24°$.

probability of approx. 80% into proton, but due to the overlaying likelihood distributions, it can be incorrectly classified, in oxygen or iron. The same can be seen in case of oxygen and iron primaries initiating the Extensive Air Showers. Knowing the probabilities of classification and misclassification, the true mass composition can be calculated by solving the system of equations 7.10. The observables $\{N_\mu^{tr}, N_e\}$ plays a key role in mass discrimination. For this reason, probabilities for other combinations of observables (having as "nucleus" the pair $\{N_\mu^{tr}, N_e\}$) are compared with those given only by $\{N_\mu^{tr}, N_e\}$. A slightly improvement of discrimination is seen by the combination $\{N_\mu^{tr}, N_e, q_{0.50}, q_{0.75}\}$ (Fig. 7.2) and even better for $\{N_\mu^{tr}, N_e, s, q_{0.50}, q_{0.75}\}$ (Fig. 7.3).

7.5 N_μ^{tr}-dependence of the mass composition

A test how a given mass composition using the set $\{N_\mu^{tr}, N_e, q_{0.50}, q_{0.75}\}$ can be reconstructed is shown in Fig. 7.4. Five $log_{10}N_\mu^{tr}$ bins have been used:

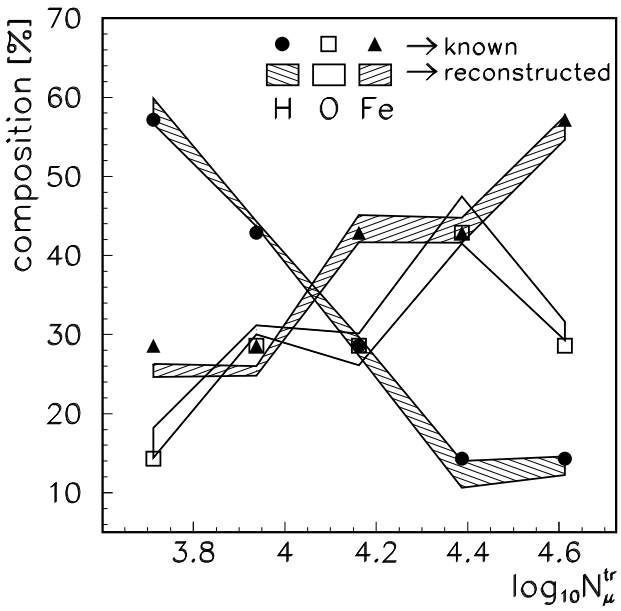

Fig. 7.4: Test of reconstruction of a given mass composition; 80 m $< R_\mu \leq$ 90 m, $0° < \theta \leq 24°$.

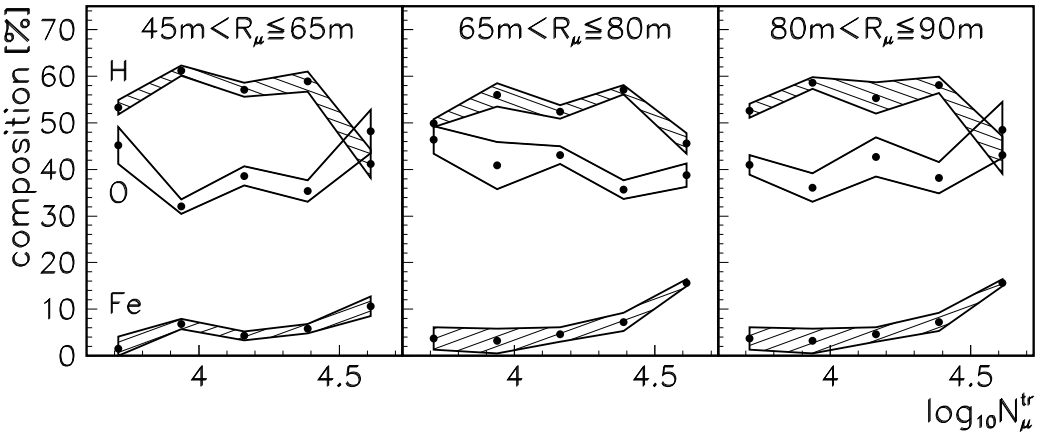

Fig. 7.5: Experimental mass composition estimated from KASCADE measurements in three radius bins in a zenithal angle range $0° < \theta \leq 24°$. $N_\mu^{tr}, N_e, q_{0.50}, q_{0.75}$ have been used as set of observables for mass discrimination.

$3.6 \div 3.825$, $3.825 \div 4.050$, $4.050 \div 4.275$, $4.275 \div 4.5$, $4.5 \div 4.725$. In each of these five bins, some arbitrary known mass compositions have been considered. They are represented by symbols. Applying the Bayes procedure, these compositions should be furtheron reconstructed. Reconstructed compositions are represented with shadowed areas. The thickness of the shadowed areas corresponds to statistical errors estimated from the bootstrap procedure. A very good agreement can be seen. It has to be noted that the procedure has been applied to the sets of simulations made by the same model. Therefore systematic uncertainities due to a wrong modelling of the EAS are not included in the test.

The experimental mass composition estimated from KASCADE measurements using as set of observables $\{N_\mu^{tr}, N_e, q_{0.50}, q_{0.75}\}$ is given in Fig. 7.5 for three different radius bins. It is necessary to precise that at least at smaller primary energies (smaller N_μ^{tr}) this estimation of the mass composition (from Fig. 7.5) has to be normalised to obtain the efficiency corrected mass composition. Particularly in this work, radius bins at relatively larger distances from the shower core have been used, hoping in a better mass discrimination induced by muon arrival times. At smaller primary energies and for showers in the margins of KASCADE array it is more difficult to recon-

struct a valid event. The KASCADE experiment has different efficiencies for different primaries at a given distance. An increasing concentration of the heavier component at higher primary energies is seen in Fig. 7.5, consistent in all radial ranges. The knee is at approx. $log_{10}N_{\mu}^{tr} = 4.2$.

7.6 Primary mass composition

In this paragraph is presented an estimation of the primary mass composition given by normalising the reconstructed mass compositions which are obtained by using multivariate analysis on some experimental samples (corresponding to some selections on measured data by KASCADE experiment). Three selections have been considered, defined by following cuts on R_{μ}, N_{μ}^{tr}, θ, n:

- 3 radius ranges are considered: 45÷65 m, 65÷80 m, 80÷90 m;
- $3.95 < N_{\mu}^{tr} \leq 4.45$ (this N_{μ}^{tr} range is centered around the knee region);
- $0° < \theta \leq 24°$ (rather vertical showers, reconstructed with higher accuracy);
- multiplicity n of muons (above 2.4 GeV) detected in Central Detector larger than 3.

If the integral of the "spectrum" 5.2 (with spectral index around the "knee" given by eq. 5.3) is normalised to 1 for each primary type in a range of:

$$\{E_0 \mid 5.00 \cdot 10^{14} \text{ eV} \leq E_0 \leq 3.06 \cdot 10^{16} \text{ eV}\} \times$$
$$\{\theta \mid 0° \leq \theta \leq 40°\} \times$$
$$\{D_{cor} \mid D_{cor} \in cut1 \cup cut4\} \times$$
$$\{n \mid n \geq 0\}$$

then the values of the contributions C_{A_i} ($A_i \in \{H, O, Fe\}$) of these "spectra" in each of the defined selections are given in the table 7.1. They are calculated from Monte Carlo simulations. Of course, the lower and upper limits of the variables E_0, θ, D_{cor}, defining the "spectrum" given by equation 5.2, are large enough to avoid "interferences" (due to fluctuations or defectuous EAS reconstructions) from outside (these limits) applying in the selections defined above.
Even if (in average) the electromagnetic component of the proton shower is larger than for heavier primaries (see Fig. 3.1, KASCADE level), the con-

R_μ	C_H	C_O	C_{Fe}
45÷65 m	$1.80 \cdot 10^{-3}$	$3.23 \cdot 10^{-3}$	$3.86 \cdot 10^{-3}$
65÷80 m	$1.92 \cdot 10^{-3}$	$3.53 \cdot 10^{-3}$	$3.93 \cdot 10^{-3}$
80÷90 m	$1.13 \cdot 10^{-3}$	$2.46 \cdot 10^{-3}$	$2.67 \cdot 10^{-3}$

Tab. 7.1: Contributions of H, O, Fe "spectra" in the defined selections; $3.95 < N_\mu^{tr} \leq 4.45$, $0° < \theta \leq 24°$, $n \geq 3$.

R_μ	$P_H(\%)$	$P_O(\%)$	$P_{Fe}(\%)$	$P_H^*(\%)$	$P_O^*(\%)$	$P_{Fe}^*(\%)$
45÷65 m	56.8	40.0	3.2	71.5	26.7	1.8
	±0.5	±1.7	±1.5	±0.7	±1.1	±0.8
65÷80 m	56.9	39.6	3.5	70.8	27.1	2.1
	±1.4	±1.6	±0.6	±1.7	±1.1	±0.4
80÷90 m	57.3	40.6	2.1	74.6	24.2	1.2
	±1.3	±1.2	±0.9	±1.6	±0.7	±0.5

Tab. 7.2: The reconstructed mass composition of the observed data sample (P_H, P_O, P_{Fe}) as compared with the results obtained after corrections for the efficiency of KASCADE (P_H^*, P_O^*, P_{Fe}^*); $3.95 < N_\mu^{tr} \leq 4.45$, $0° < \theta \leq 24°$, $n \geq 3$.

tributions for proton (C_H) are systematically smaller for all three selections as compared with the other primaries. The reason is the etablished cut on muon multiplicity ($n \geq 3$) which removes many showers induced by protons because of their small number of muons above 2.4 GeV at larger distances from the shower core (Fig. 3.1).
Because of these different contributions corresponding to different primaries, reconstructed mass compositions P_{A_i} ($A_i \in \{H, O, Fe\}$) has to be normalized to efficiency corrected mass compositions $P_{A_i}^*$ ($A_i \in \{H, O, Fe\}$), according to the relation:

$$P_H^* : P_O^* : P_{Fe}^* = \frac{P_H}{C_H} : \frac{P_O}{C_O} : \frac{P_{Fe}}{C_{Fe}} \tag{7.11}$$

Tab. 7.2 presents the three values of the primary mass composition (efficiency corrected) obtained for the three selections defined above. Estimating the mass composition as a mean value over all three selections, the result $\overline{P_H^*} : \overline{P_O^*} : \overline{P_{Fe}^*} = 72.3 : 26.0 : 1.7$ has been obtained in the primary energy range

$5 \cdot 10^{14}$ eV $\leq E_0 \leq 3 \cdot 10^{16}$ eV; values of the mass composition in different energy ranges (near the "knee" region) can be formally derived from the above estimation according to the dependence of the spectral index given by relation 5.3.

8. CONCLUSIONS AND OUTLOOK

The present work investigates the temporal structure of the muon component of high energy extensive air showers, with the aspect how it maps the longitudinal EAS profile and contributes to the discrimination of the mass of the cosmic particles inducing the EAS. The study is based on measurements of the muon arrival time distributions using the timing facilities of the Central Detector of the KASCADE experiment. The time structure of the muon component has been characterised by the distributions of the mean arrival time and of various quantiles, the first quartile $\Delta\tau_{0.25}$, the median $\Delta\tau_{0.50}$ and the third quartile $\Delta\tau_{0.75}$, of the muon arrival time distributions, observed for the single EAS event-by-event. The lateral time profile of the EAS muon component, defined as the average variation of the quartile-distributions with the distance from the shower axis, has been studied in correlation with the variation of the zenith angle-of-EAS incidence, the shower age and of the truncated muon number N_μ^{tr} (used as primary energy identifier). In addition to simple phenomenological parametrisations, proposed in literature, the observed distributions have been compared with predictions of realistic simulations of the EAS development. The simulation calculations have been performed with the EAS Monte Carlo simulation code CORSIKA, invoking the QGSJET model as generator. A good overall agreement is found and indicates that the average longitudinal EAS profile, as predicted by the CORSIKA description, agrees with the experimental findings. In contrast to previous studies [21, 22], which are restricted to the local time profile (measured at several radial distances from the shower core with reference to the first registered muon arriving there), in this work global times are considered, referring to the arrival of the shower center. Since the arrival time of the shower core could not be experimentally determined, a procedure, based on simulations has been developed to transform the locally observed distributions to the arrival time of the shower core as reference time. In this way some unfortunate features of experimental local distributions, arising from the considerable fluctuations of the arrival of the first muon and thus being

distinctly dependent from the multiplicity of the observed muons, could be relieved. In order to illustrate the relation between the features of the longitudinal EAS development and the time structure of the shower disk, an approach (proposed by J. Linsley) for the determination of the EAS elongation rate has been scrutinised [24]. This approach induced the hope to infer the elongation rate and fluctuations of the atmospheric height of the shower maximum from the observed energy and zenith angle dependence of the observable with invoking Monte Carlo simulations. This thesis shows that this is not possible, since a scaling factor enters in the procedure, whose complex dependence from various EAS details is a-priori unknown. Hence the analysis of the data is thrown back to corresponding (model dependent) Monte Carlo simulations. Thus for the analysis of the experimental data nonparametric multivariate analyses have been performed in order to explore the role of muon arrival time distribution parameters for the EAS characterisation, in particular for the mass determination of the primary. The analysis includes the correlations of the main discriminator by N_e/N_μ with the age, the quartiles of the local arrival time distributions, the multiplicity of the muons and also the ratio of the time parameters to the observed muon local density (thus including the effect of the lateral density distributions). The analysing technique implies a specification of the true- and the mis- classification probabilities of the EAS events. In context of the topics of this work, the main aspect has not been to determine the cosmic ray mass composition (which has been attempted in a more wider analysis of the KASCADE collaboration (see [61, 73]), but rather the role of the time structure observations. It turns out that in the radial distances from the shower axis, limited by the KASCADE array, the discriminate power is not significant, if the actual detection efficiency and limited time resolution is taken into account, though pure CORSIKA simulations for an ideal detector appear promising. The KASCADE collaboration has committed an extension of the array: KASCADE GRANDE [74] potentially allowing the observation of muon arrival time distribution at larger distances from the shower core and at larger primary energies, favourising discriminative features of the temporal EAS structure. As an outlook this perspective is illustrated in Fig. 8.1. It displays simulated results for the quantity $q_{0.75}(R_\mu) = Q_{0.75}/\rho_\mu$ ($Q_{0.75}$ being the local third quartil and ρ_μ the muon density) observed for proton and iron induced showers at $R_\mu = 220 \div 230$ m. It compares the cases of two different primary energies, for an ideal detector and a detector with the realistic response of the timing facility of the KASCADE Central Detector. It turns

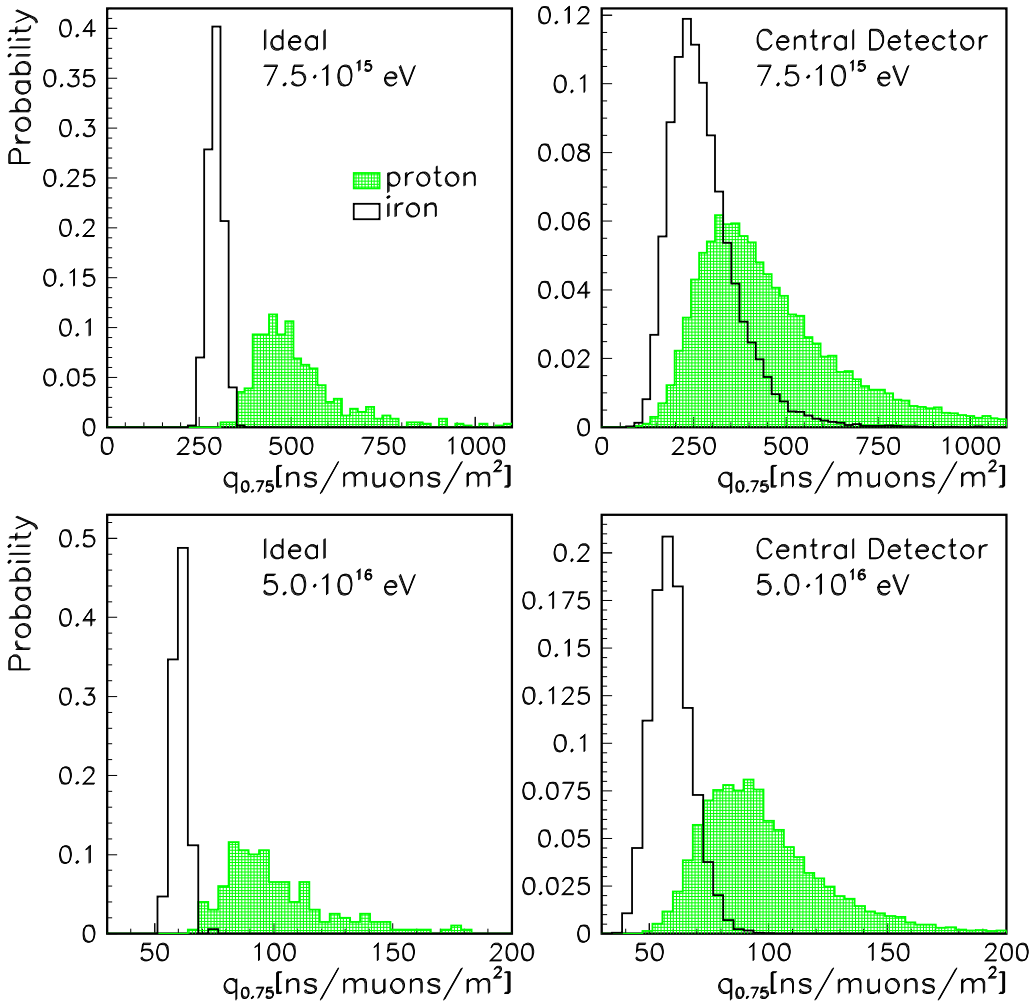

Fig. 8.1: Simulated distributions $q_{0.75}$ of proton and iron induced EAS, observed for two different primary energies ($E_0 = 7.5 \cdot 10^{15}$ eV and $E_0 = 5 \cdot 10^{16}$ eV), at the zenith angle of primary incidence $\theta = 0°$, for a muon energy threshold of 2.4 GeV and a distance from the shower axis $R_\mu = 220 \div 230$ m. Two cases are presented: for an ideal detector (with the area of a ring at the distance R_μ) and the realistic case which includes the response of the KASCADE Central Detector.

out that the time resolution gets decreasing importance at larger distances R_μ, also for the determination of the arrival time of the shower core (Fig. 8.2

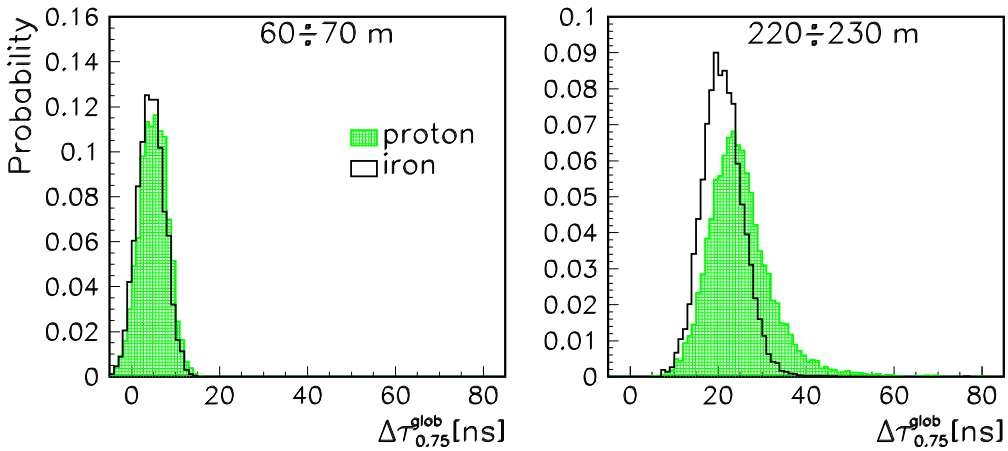

Fig. 8.2: Simulated distributions $\Delta\tau^{glob}_{0.75}$ of proton and iron induced EAS, observed for the primary energy $E_0 = 7.5 \cdot 10^{15}$ eV, at the zenith angle of primary incidence $\theta = 0°$, for a muon energy threshold of 2.4 GeV and two distances from the shower axis ($R_\mu = 60 \div 70$ m and $R_\mu = 220 \div 230$ m). The realistic case which includes the response of the KASCADE Central Detector is presented. A time resolution of 3 ns is considered for estimating the arrival time of the electromagnetic front of the shower core.

shows the improved discrimination between proton and iron induced EAS at larger distances). These features indicate promising application of the muon arrival time measurements for an extended KASCADE configuration.
This work is a supplementary argument for the extension of the KASCADE experiment.

Acknowledgements

My thanks are first directed to Prof. Dr. M. Petrovici and Prof. Dr. H. Rebel, the scientific coordinators of my work, for encouraging supervision and scientific guidance.
This work has been performed in the frame of the scientific-technical cooperation (WTZ) project between Germany and Romania (No. RUM-014-97).
I would like to thank Dr. Iliana M. Brancus, leader of the cosmic ray group at NIPNE-HH, and to my colleagues Dr. B. Vulpescu, Eng. H. Bozdog and Eng. M. Petcu for introducing me in cosmic rays studies.
I am particularly grateful to Prof. Dr. H. Rebel and Prof. Dr. G. Schatz for the kind hospitality during various research visits in Institut für Kernphysik of Forschungszentrum Karlsruhe.
I thank Dr. A. Haungs, Dr. H.-J. Mathes, Dr. J. Wentz, Dr. R. Haeusler, Dr. M. Roth, DM. J. Oehlschläger for helpful scientific and technical advices.
I thank all members of the KASCADE Collaboration for the opportunity to collaborate in such an interesting experiment.
Finally I would like to thank my wife Madalina for her encouragement and understanding tolerance during the period of preparing this thesis.

BIBLIOGRAPHY

[1] P. Sokolsky, Introduction to Ultrahigh Energy Cosmic Ray Physics, Addison-Wesley Publishing Co. (1989) p. 7.

[2] D.J. Bird et al. - Fly's Eye Collaboration, Phys. Rev. Lett. 71 (1993) 71.

[3] H. Rebel et al. - KASCADE Collaboration, Acta Phys.Polon. B31 (2000) 323.

[4] M.S. Longair, High Energy Astrophysics, Cambridge, Cambridge University Press (1981) p. 117.

[5] J. Knapp, FZKA-Report 5970, Forschungszentrum Karlsruhe (1997).

[6] The KASCADE Collaboration:
T. Antoni, W.D. Apel, A.F. Badea, K. Bekk, K. Bernlöhr, H. Blümer, E. Bollmann, H. Bozdog, I.M. Brancus, A. Chilingarian, K. Daumiller, P. Doll, J. Engler, F. Feßler, H.J. Gils, R. Glasstetter, R. Haeusler, W. Hafemann, A. Haungs, D. Heck, T. Holst, J.R. Hörandel, K.H. Kampert, J. Kempa, H.O. Klages, J. Knapp, D. Martello, H.J. Mathes, H.J. Mayer, J. Milke, D. Mühlenberg, J. Oehlschläger, M. Petcu, H. Rebel, M. Risse, M. Roth, G. Schatz, F.K. Schmidt, T. Thouw, H. Ulrich, A. Vardanyan, B. Vulpescu, J.H. Weber, J. Wentz, T. Wiegert, J. Wochele, J. Zabierowski, S. Zagromski,
Nucl. Phys. B, Proc. Suppl. 75A (1999) 234.

[7] A. Haungs et al. - KASCADE Collaboration, Nucl.Phys.B (Proc.Suppl.) Vol.87 (2000) 414.

[8] K. Bernlöhr et al. - KASCADE Collaboration, Nucl.Phys.B (Proc.Suppl.) Vol.87 (2000) 528.

[9] The CASA-MIA Collaboration, Nucl. Phys. B, Proc. Suppl. 75A (1999) 241.

[10] The HEGRA Collaboration, Nucl. Phys. B, Proc. Suppl. 75A (1999) 244.

[11] M. Aglietta et al. (EAS-TOP), Nucl. Phys. B, Proc. Suppl. 75A (1999) 251.

[12] H. Rebel, Proceedings NATO Advanced Study Institute "Nuclei Far from Stability and Astrophysics", Predeal - Romania, August 28 - September 8, 2000, in press.

[13] J.R. Hörandel et al. - KASCADE Collaboration, Nucl. Phys. B (Proc. Suppl.) 75A (1999) 228.

[14] T. Antoni et al. - KASCADE Collaboration, J. Phys. G: Nucl. Part. Phys. 25 (1999) 2161.

[15] J. Linsley, 15^{th} ICRC (Plovdiv, Bulgaria) Vol. 12 (1997) 89.

[16] B. Vulpescu et al., NIM A 414 (1998) 205.

[17] H. Rebel, G. Völker, M. Föller and A.A. Chilingarian, Journ. Phys. G: Nucl. Part. Phys. 21 (1995) 451;
H. Rebel, in: The Cosmic Ray Mass Composition, Proc. XV Cracow Summer School of Cosmology, 15-19 July, 1996, Lodz, Poland, Uniwersytetu Lodzkiego, ed. W. Tkaczyk (1997) 91.

[18] T.V. Danilova, D. Dumora, A.D. Erlykin and J. Procureur, Journ. Phys. G: Nucl. Part. Phys. 20 (1994) 961.

[19] I.M. Brancus et al., Astropart. Phys.7 (1997) 343.

[20] M. Föller, U. Raidt et al. - KASCADE Collaboration, 25th ICRC (Durban, South Africa), Vol. 6 (1997) 149.

[21] T. Antoni et al. - KASCADE Collaboration, "Time structure of the EAS Muon Component measured by the KASCADE Experiment", Astropart. Phys. (2000), in press.

[22] R. Haeusler, FZKA-Report 6520, Forschungszentrum Karlsruhe (2000).

[23] Graf, Henning, Stange, Wirlich, Formeln und Tabellen der angewandten mathematischen Statistik, Springer Berlin-Heidelberg (1987) p. 27.

[24] A.F. Badea et al., "A simulation based study of Linsley's approach to infer the elongatin rate and fluctuations of the EAS maximum depth from muon arrival time distributions", Astropart. Phys. (2000), in press.

[25] D. Heck et al., FZKA-Report 6019, Forschungszentrum Karlsruhe (1998).

[26] Handbook of Chemistry and Physics, 67^{th} Edition, R.C. Weast ed. (The Chemical Rubber Co., Cleveland, 1986) F141.

[27] K. Werner, Phys. Rep. 232 (1993) 87.

[28] N.N. Kalmykov and S.S. Ostapchenko, Yad. Fiz. 56 (1993) 105; Phys. At. Nucl. 56(3) (1993) 346; N.N. Kalmykov, S.S. Ostapchenko and A.I. Pavlov, Bull. Russ. Acad. Sci. (Physics) 58 (1994) 1966.

[29] J. Ranft, Phys. Rev. D51 (1995) 64.

[30] R.S. Fletcher, T.K. Gaisser, P. Lipari and T. Stanev, Phys. Rev. D50 (1994) 5710.

[31] H. Fesefeldt, Report PITHA-85/02 (1985), RWTH Aachen.

[32] P.K.F. Grieder, Report INS-J125 (1970), Inst. for Nuclear Studies, Univ. of Tokyo; P.K.F. Grieder, Proc. 16^{th} Int. Cosmic Ray Conf., Kyoto, 9 (1979) 161.

[33] R. Brun et al., GEANT3, Report CERN DD/EE/84-1 (1987), CERN, Geneva.

[34] W.R. Nelson, H. Hiroyama and D.W.O. Rogers, SLAC Report 265 (1985).

[35] M.F. Bourdeau et al., J. Phys. G: Nucl. Phys. 6 (1980) 901.

[36] I.M. Brancus, Proceedings NATO Advanced Study Institute "Nuclei Far from Stability and Astrophysics", Predeal - Romania, August 28 - September 8, 2000, Kluwer Academic Publishers, Boston/Dordrecht/London, eds. D. Poenaru, H. Rebel, J. Wentz, in press.

[37] O. Saavedra, Proceedings of the Chacaltaya Meeting on Cosmic Ray Physics, to be published in Nuovo Cimento C.

[38] A.A. Chilingarian et al.-ANI Collaboration, 26th ICRC, Salt Lake City, Utah, August 17-25, Vol. 1, (1999) 240.

[39] C.L. Bhat et al., NIM A 340 (1994) 413.

[40] A. Lindner, Astropart. Physics 8 (1998) 235 and private communication; A. Lindner et al.-HEGRA Collaboration Proc. 10^{th} ISVHECRI 1998, Gran Sasso, Italy, July 12-18, 1998, Nucl. Phys. B (Proc. Suppl.)75A (1999) 244.

[41] G.L. Cassidy et al., Astrophys. Journ. 356 (1990) 669.

[42] J. Linsley and A.A. Watson, Phys. Rev. Lett. 46 (1981) 459.

[43] T.K. Gaisser et al., Rev. Mod. Phys. 50 (1978) 859.

[44] M. Dolores Rodriguez-Frias, Luis del Peral and Jose Medina, Astropart. Phys. 8 (1977) 77.

[45] R. Walker and A.A. Watson, Journ. Phys. G: Nucl. Phys. 7 (1981) 1297.

[46] P.R. Blake, W.S. Collis, M. Luksys, W.F. Nash and A.J. Sephton, Journ. Phys. G: Nucl. Phys. 16 (1990) 775.

[47] I. Atanasov et al., FZKA-Report 6474, Forschungszentrum Karlsruhe (2000).

[48] J. Zabierowski et al., NIM A 354 (1995) 496.

[49] J. Engler et al., NIM A 427 (1999) 528.

[50] T. Antoni et al. - KASCADE Collaboration, "Electron, Muon and Hadron Lateral Distributions Measured in Air-Showers by the KASCADE Experiment", submitted to Astropart. Phys. (2000).

[51] H. Bozdog et al., "The detector system for measurement of multiple cosmic muons in the central detector of KASCADE", submitted to NIM A (2000).

[52] J.H. Weber et al. - KASCADE Collaboration, 25th ICRC (Durban, South Africa), Vol. 6 (1997) 153.

[53] R. Glasstetter et al. - KASCADE Collaboration, 25th ICRC (Durban, South Africa), Vol. 6 (1997) 157.

[54] B. Wiebel-Sooth, P.L. Biermann and H. Meyer, Astron. Astrophys. 330 (1998) 389.

[55] I.M. Brancus et al. - KASCADE Collaboration, Nucl. Phys. B (Proc. Suppl.) 75A (1999) 343.

[56] A.F. Badea, Internal Report KASCADE-11/1999-03 (unpublished).

[57] W.T. Eadie, D. Drijard, F.E. James, M. Roos and B. Sadoulet, "Statistical Methods in Experimental Physics", North Holland Publishing Co., Amsterdam, The Netherlands (1971) 80.

[58] G. Battistoni, A. Ferrari, M. Carboni and V. Patera, Astropart. Phys. 9 (1998) 277.

[59] M. Ambrosio, C. Aramo, L. Colesanti, T.V. Danilova and A.D. Erlykin, Astropart. Phys. 7 (1997) 329.

[60] A.A. Chilingarian, Comp. Phys. Comm. 54 (1989) 381; A.A. Chilingarian, G.Z. Zazian, Nuovo Cim. 14 (1991) 355.

[61] M. Roth, FZKA-Report 6262, Forschungszentrum Karlsruhe (1999).

[62] A.A. Chilingarian et al. - KASCADE Collaboration, Nucl. Phys. B (Proc. Suppl.) 75A (1999) 302.

[63] M. Rosenblatt, Ann. Math. Stat. 27 (1956) 832.

[64] E. Parzen, Ann. Math. Stat. 33 (1962) 1065.

[65] E. Fix and J.L. Hodges. Project 21-49-004, Report 4, USAF School of Aviation Medicine, Randolf Field, Texas (1951).

[66] D.O. Lofsgaarden and C.D. Quesenberry, Ann. Math. Stat. 36 (1965) 1049.

[67] P.C. Mahalonobis, Proc. of the Nat. Inst. of India 2 (1936) 49.

[68] S.M. Snappin and J.D. Knoke, Technometrics 26 (1984) 371.

[69] B. Efron, Bootstrap methods, another look at the jacknife, Ann. Statist., Vol. 7, (1979) 1.

[70] A.A. Chilingarian, ANI-program, 1999, unpublished.

[71] I.M. Brancus, Internal Report KASCADE-09/2000-02 (2000) (unpublished).

[72] HBOOK 4.21, Reference Manual, CERN (1993) p.93.

[73] T. Antoni et al. - KASCADE Collaboration, "A Non-Parametric Approach to Infer the Energy Spectrum and the Mass Composition of Cosmic Rays", submitted to Astropart. Phys. (2001).

[74] M. Aglietta et al., Proposal to Study Cosmic Ray Primaries and their Interactions at $E_0 \simeq 10^{16} - 5 \cdot 10^{17}$ (1999).

APPENDIX

A. SCALING FACTOR F AND BAROMETRIC PROFILE OF THE ATMOSPHERE

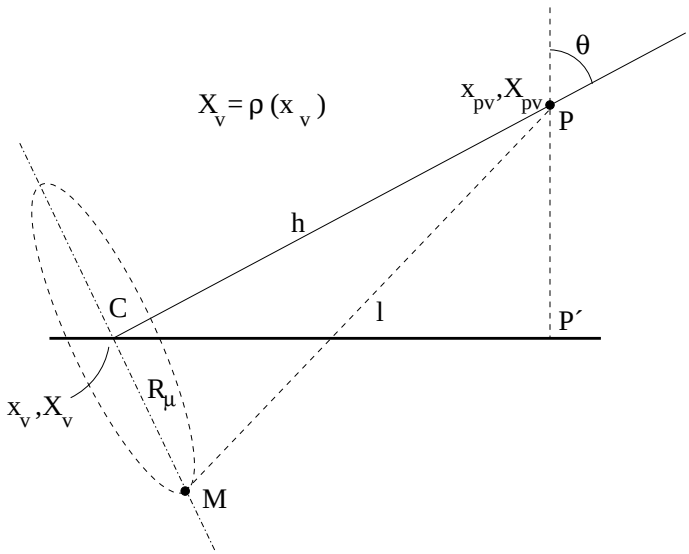

Fig. A.1: Simple triangulation arrival time - production point of the muon. U.S. standard atmosphere with five layers: $X_v = \rho(x_v) = a_i + b_i exp(-x_v/c_i)$.

The basic relation to estimate $F^{(e,\mu)}$ is eq. 3.10. It will be shown that f$(X, X_m)(\equiv f^\mu(X, X_m^\mu)$ from eq. 3.10, muons above 2 GeV) practically has no analytical form due to the influence of the barometric profile of the atmosphere. For simplicity let's consider T as arrival time of a single muon (M in figure A.1); P is the production point of this muon. Using notations of

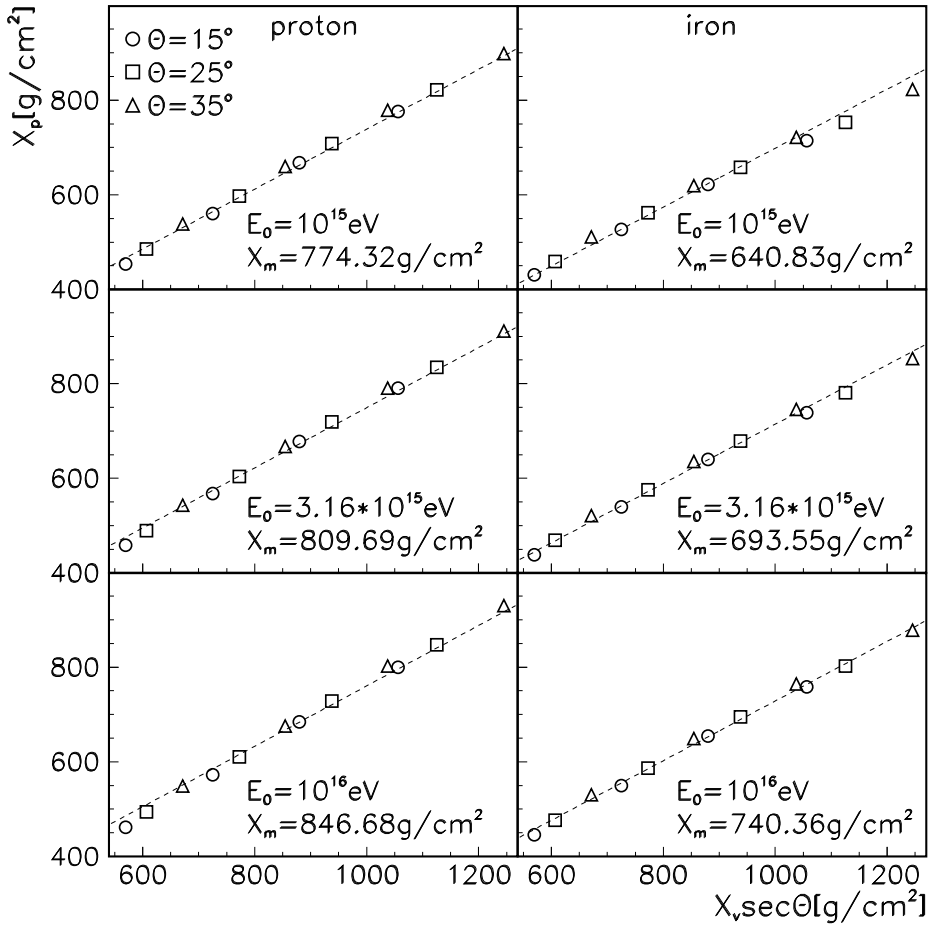

Fig. A.2: The mean muon production points X_p for proton and iron induced EAS at 3 primary energies and 3 zenithal angles as estimated from simple triangulation in case of $T \equiv \Delta\tau^{glob}_{mean}$.

Fig. A.1 there are following relations:

$$T = \frac{l-h}{c} = \frac{\sqrt{R^2+h^2}-h}{c} \tag{A.1}$$

$$x_{pv} = x_v + h \cdot cos\theta \tag{A.2}$$

where x is altitude and X is density. Applying U.S. standard atmosphere

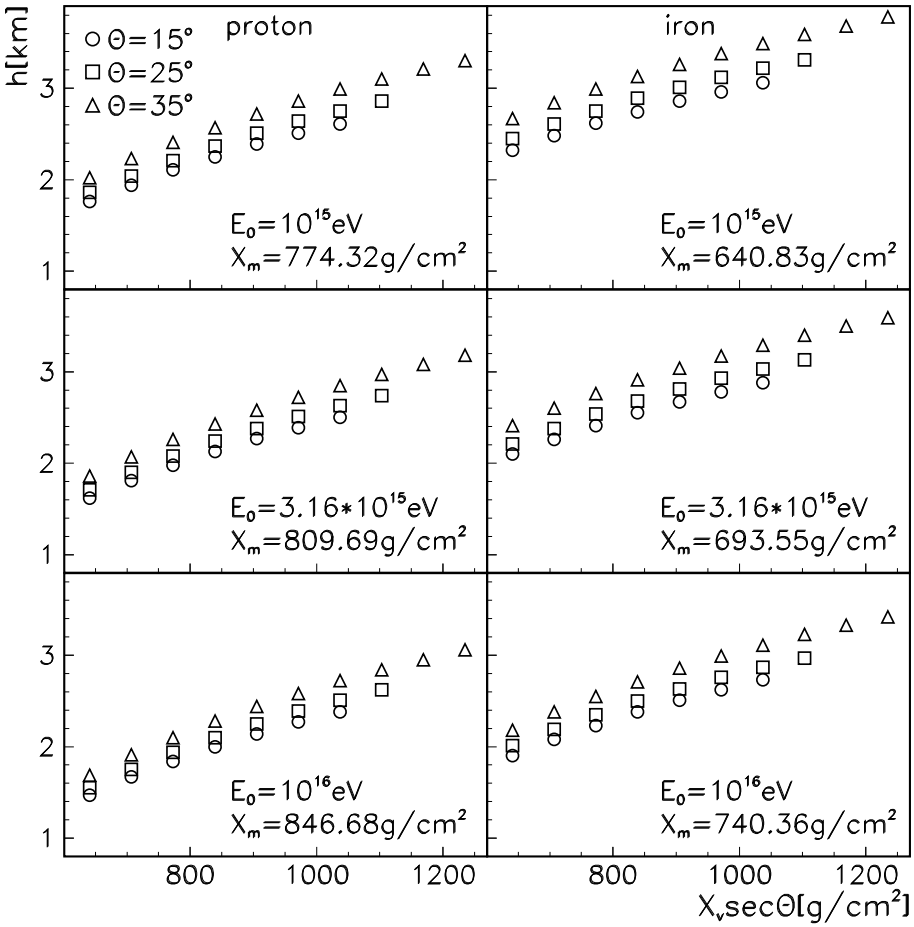

Fig. A.3: Numerical estimation of h from eqs. A.3 and A.4.

function ρ to eq. A.2 the following relation:

$$X_p \cdot cos\theta = \rho(h \cdot cos\theta + \rho^{-1}(X \cdot cos\theta)) \tag{A.3}$$

has been obtained. The mean muon production point X_p (see Fig. A.2), estimated from triangulation using the simulated values of $T \equiv \Delta\tau^{glob}_{mean}$, is a simple function of X_m and $X = X_v sec\theta$, valable simultaneously for proton and iron induced EAS at different primary energies and zenithal angles:

$$\begin{aligned} &X_p = (a + b \cdot X_m) \cdot X + c \cdot X_m + d \\ &a = 0.575; b = 0.739 \cdot 10^{-4}\ \mathrm{cm^2/g}; c = 0.226; d = -69.480\ \mathrm{g/cm^2} \end{aligned} \tag{A.4}$$

The dotted lines from Fig. A.2 represent the fit with the function above of X_p values. Even if it exists the simple form A.4 between X_p, X and X_m, because of the complex relation A.2 (ρ contains five exponential terms) it results (from eqs. A.3 and A.4) a rather complicate form for h as function of X_v, X and X_m (see fig. A.3). Replacing h in eq. A.2 it results a complicate form for $\mathrm{f}(X, X_m)$ and then for F from eq. 3.10. Practically there is no analytical form for $F^{(e,\mu)}$. The only solution is to estimate F directly from simulations.

B. STATISTICAL CALCULATIONS FOR WEIGHTED EVENTS

The following definitions have been used for statistical calculations (w_i is the weight of event x_i):

- Expectation value:

$$E(x) = \frac{\sum_{i=1}^{n} w_i x_i}{\sum_{i=1}^{n} w_i}$$

- Mean value: $E(x)$
- Central moment of ordin n:

$$M(n) = E((x - E(x))^n)$$

- Standard deviation:

$$\sigma = \sqrt{M(2)}$$

- Number of equivalent events [72]:

$$N = \frac{\left(\sum_{i=1}^{n} w_i\right)^2}{\sum_{i=1}^{n} w_i^2}$$

- Uncertainity for the mean value:

$$\frac{\sigma}{\sqrt{N}}$$

- Uncertainity for σ:

$$\frac{\sigma}{\sqrt{2(N-1)}}$$

C. BAYES THEOREM

Bayes theorem gives the propability of A_i-class (hypothesis) to be truth if the x-value was observed, and before experiment the $P(x \mid A_j)$ prior probabilities were assumed.
Bayes theorem:

$$P(A_i \mid x) = \frac{P(x \mid A_i)P(A_i)}{\sum_{j=1}^{m} P(x \mid A_j)P(A_j)}, \quad i \in \{1, m\} \tag{C.1}$$

Proof:

$$P(x \cap A_i) = P(x \mid A_i)P(A_i) = P(A_i \mid x)P(x)$$

It results:

$$P(A_i \mid x) = \frac{P(x \mid A_i)P(A_i)}{P(x)}, \quad i \in \{1, m\} \tag{C.2}$$

But:

$$P(x) \overset{7.1}{=} P(x \cap A) = P\left(x \cap \left(\bigcup_{j=1}^{m} A_j\right)\right) == P\left(\bigcup_{j=1}^{m}(x \cap A_j)\right) \tag{C.3}$$

Because classes A_j are disjunctive we can write:

$$P\left(\bigcup_{j=1}^{m}(x \cap A_j)\right) = \sum_{j=1}^{m} P(x \cap A_j) = \sum_{j=1}^{m} P(x \mid A_j)P(A_j) \tag{C.4}$$

From relations C.2, C.3 and C.4 it results C.1 (q.e.d.)